공학박사 학위논문

Micro-CT Characterization and Reconstruction Modeling for Multiscale Analysis of Sheet Molding Compound (SMC) Composites

SMC 복합재료 멀티스케일 해석을 위한
Micro-CT 특성화 및 재구성 모델링

2023 년 2 월

서울대학교 대학원
기계항공공학부
임 형 준

SMC 복합재료 멀티스케일 해석을 위한 Micro-CT 특성화 및 재구성 모델링

Micro-CT Characterization and Reconstruction Modeling for Multiscale Analysis of Sheet Molding Compound (SMC) Composites

지도교수 윤 군 진

이 논문을 공학박사 학위논문으로 제출함

2022 년 12 월

서울대학교 대학원

기계항공공학부

임 형 준

임형준의 공학박사 학위논문을 인준함

2022 년 12 월

위 원 장 : 신 상 준 (인)

부위원장 : 윤 군 진 (인)

위 원 : 김 도 년 (인)

위 원 : 박 상 욱 (인)

위 원 : 유 승 화 (인)

Micro-CT Characterization and Reconstruction Modeling for Multiscale Analysis of Sheet Molding Compound (SMC) Composites

Advisor: Prof. Gun Jin Yun

Submitting a Ph.D. Dissertation of Engineering

December 2022

Graduate School of Engineering
Seoul National University
Mechanical and Aerospace Engineering

Hyoung Jun Lim

Confirming the Ph.D. Dissertation written by
Hyoung Jun Lim
December 2022

Chair	Prof. SangJoon Sin
Vice Chair	Prof. Gun Jin Yun
Examiner	Prof. Do-Nyun Kim
Examiner	Prof. Sangwook Park
Examiner	Prof. Seunghwa Ryu

Abstract

With the advancement of technology in the aerospace field, high-performance materials are in increasing demand and application. Hence, beyond the original performance of a single material, a composite material composed of two or more materials is utilized in many fields. Especially, due to the mass production advantage in the compression molding process, sheet molding compound (SMC) composites have gained increasing attention in the automotive industry. However, due to the high spatial inhomogeneity of SMC composites, local properties differ within the SMC plate, which leads that the SMC composite is difficult to predict mechanical behavior. The dissertation proposes novel multi-scale modeling to construct a mesostructure of SMC composite using micro-CT characterization and a stochastic reconstruction algorithm. It predicts the elastic properties and strength of SMC composites through computational simulation.

Before dealing with SMC composites, multi-scale analysis is introduced using a homogenization technique. Homogenization refers to the process of deriving the effective properties of a microstructure composed of two or more materials. This method is generally applied to larger-scale structures in order to evaluate their material and structural behaviors. For example, it can be classified into a direct numerical simulation (DNS) employing the finite element method and mean-field homogenization (MFH) based on the Eshelby tensor to express the shape of the reinforcement of composite materials. It is presented two types of homogenization techniques for the multi-scale analysis of composite materials, along with their characteristics.

Next, a reconstruction algorithm based on statistical distributions is presented to construct the mesostructure of SMC composite materials. Design variables are determined by the intrinsic characteristics of SMC composite materials. The direction and dispersion, as well as the shape of the fiber bundles constituting the SMC plate, are reflected in a mesostructure reconstruction model. A finite element analysis of the static linear behavior is conducted and verified with the experimental results. Finally, the proposed model examines the change in the behaviors based on the deformation measurement method. For damage and failure analysis, the failure mechanisms of SMC composites are investigated and adapted to material constitutive models. Simulating progressive damage allows us to observe failure mechanisms that are not detectable in linear analysis. Numerous attempts have been made to simulate composite damage because of their complex fracture patterns. This study introduces different methods for determining the failure criteria of composite materials. With the material constitutive models, the tensile modulus and strength are determined through FE simulation, and failure patterns are examined based on the direction and dispersion of fibers. The proposed simulation model can explicitly observe the local deformation of composite materials and is compared with experimental results to demonstrate its validity.

Finally, the analytical homogenization technique for the efficient way is utilized for SMC composites. Miro-meso-macroscale homogenization is performed step-by-step. It considers the overlap of fiber bundles caused by the high volume fraction of fibers in the mesostructure. Moreover, it proposes the modeling technique for fiber waviness which takes place in the manufacturing process. With a simple calculation, the proposed model has proven its validity based on experimental verification and has reduced the computational cost for nonlinear analysis.

Keyword : Multiscale analysis, Composite materials, SMC (Sheet molding compound), Homogenization, Microstructure, Characterization, Micro Computed Tomography (Micro-CT)

Student Number : 2017-29220

List of Contents

List of Figures

List of Tables

Chapter 1. Introduction

1.1 Background

Materials have been emerging as a core of future industry competitiveness according to the global standardization of assembly and production capacity of complete products. To enhance the quality, cost, and delivery (QCD) competitiveness of the materials and parts, it is required to establish a research and development (R&D) platform that integrates material properties, manufacturing processes, and characterization technology. Since the announcement of the Materials Genome Initiative (MGI) by the US administration in 2011, novel materials have been developed by applying a cutting-edge research methodology that systematically combines computational materials science, creative experiments (process design), and material information (digital data). Attempts to achieve shorter development time and cost reduction are being actively pursued around the world. Thanks to the rapid development of computer technology, the evolution of modeling techniques, and the expansion of material databases, computational materials science and process technology have become indispensable R&D tools in material development beyond theory and experimentation. Especially, computational materials science, which is led exclusively by a few advanced technological countries, requires long-term investment due to its technical merits. Open innovation that pursues knowledge broadly through interdisciplinary cooperation is required, and it is expected that this will result in a significant shift in the conventional material R&D culture.

Furthermore, it is imperative to develop methods for analyzing the interrelationships between properties and microstructures on a multiscale basis in order to break away from the traditional work that relies on empirical evaluation and trial and error. An advanced R&D network that links process-modeling-analysis/characteristic evaluation should be established by changing the R&D paradigm. Based on this idea, starting with the Accelerated Insertion of Materials (AIM) research strategy of the U.S. Defense Advanced Research Projects Agency (DARPA) in 1999, the integrated computational materials engineering (ICME) strategy from the National Materials Advisory Board (NMBD) in 2008 is being applied as a core technology to achieve a weight reduction of structural materials.

In this atmosphere, composite materials are attracting attention in many advanced industrial fields. The development of technology in recent years has led to the discovery of new materials such as graphene and carbon nanotubes (CNT). It shows inhomogeneous and consists of dissimilar constituents (or phases) that are distinguishable at some (small) length scale. Each constituent shows different material properties and/or material orientations and may itself be inhomogeneous. The use of materials in the engineering field results in demands on consideration of the heterogeneous microscopic (small-scale) characteristics. Since determining the macroscopic (large-scale) behavior of composite material is challenging for heterogeneous microstructure, it is necessary to develop a multi-scale analysis to connect their length scales. From a large-scale perspective, the behavior of the material is considered homogeneous. Composite materials exhibit heterogeneous

structures at a small-scale. The different types of microstructures using a scanning electron microscope (SEM) are summarized in Figure 1.1.

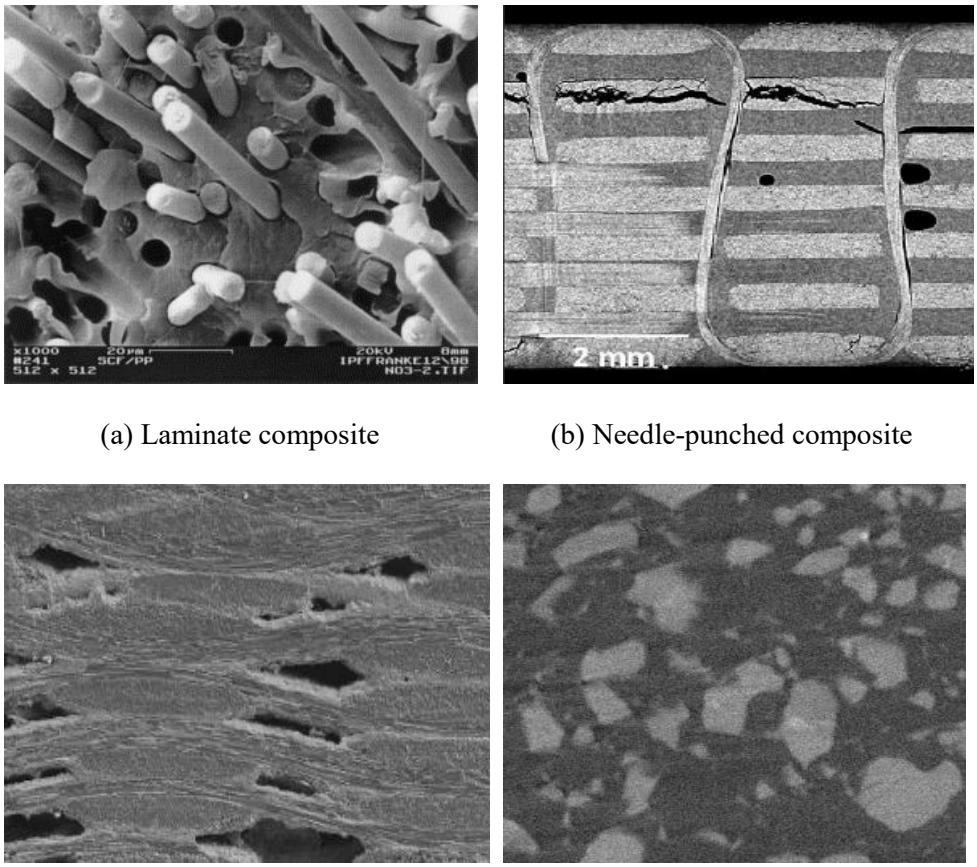

(a) Laminate composite (b) Needle-punched composite

(c) Woven composite (d) Particulate composite

Figure 1.1. Scanning electron microscope (SEM) images of composite materials [1-5]

Composite materials exhibit very complex material behavior given the spatial arrangement of size, shape, orientation, distribution, and constituents' properties [6-8]. It is noted that these factors represent a variety of physical phenomena at different

time and length scales that influence macroscopic material behavior. Depending on the purpose, composite materials can be investigated at a variety of scales, ranging from the atomic scale to continuum mechanical principles. Throughout this study, the causes of how the component derives its overall behavior are identified, including the material stiffness, thermal conductivity, and electric characteristics. The most important key role is that physical and mechanical features are connected from small to large-scale to reflect microscopic information into macroscopic behavior, which is known by the name of a multiscale method [9]. The concept image of multiscale analysis is depicted in Figure 1.2.

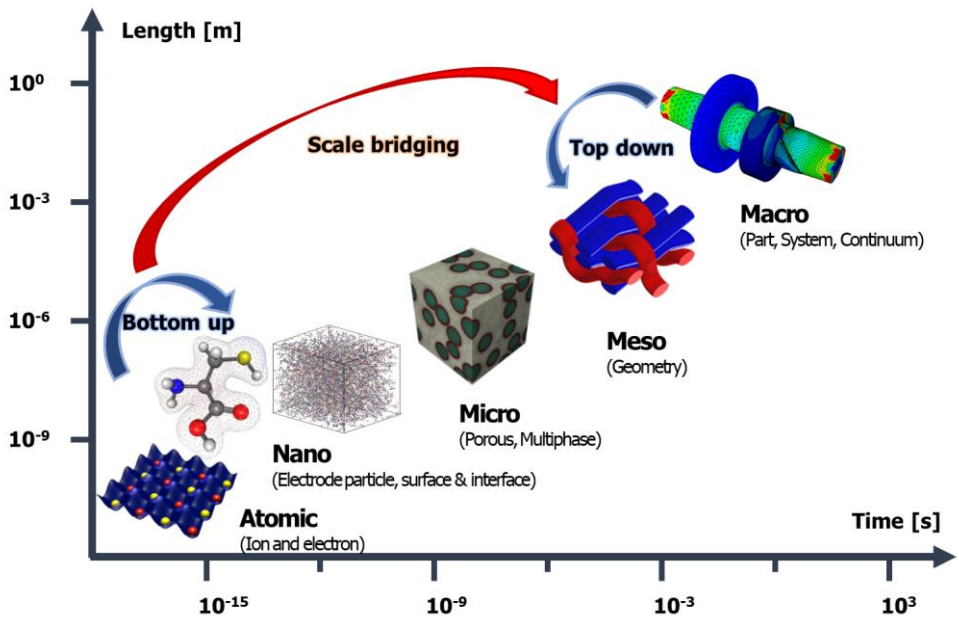

Figure 1.2. The scheme of multiscale analysis for composite materials

1.2 Sheet Molding Compound (SMC) Composites

Among many types of composite materials, sheet molding compound (SMC) is one of the most widely used composite materials in the automotive and aerospace industry. SMC shows similarity with bulk molding compound (BMC), and there are several components to this material, including thermosetting polyester resins (or vinyl esters), thermoplastic additives, and fillers. The reinforcement fibers are typically woven strands or swirl mats of 25 to 50 mm in length, and continuous fibers and woven fabrics may also be used for structural integrity. There is a typical reinforcement percentage of 40% by weight, but it can vary between 25% and 65%. Among different types of SMC, chopped bundles with short fiber-reinforced composites are gaining increasing attention owing to their enormous potential [10-12]. SMC composites with high mechanical performance are produced by increasing bundles made of short fibers. The compression molding process is suitable for SMC composites balancing mechanical performance, formability, and manufacturing costs. For these reasons, SMC has an advantage in the mass-production industry. An initial charge comprised of fiber bundles with short fibers and resin matrix is prepared as a preform and compressed into a mold. The compression molding process is illustrated in Figure 1.3.

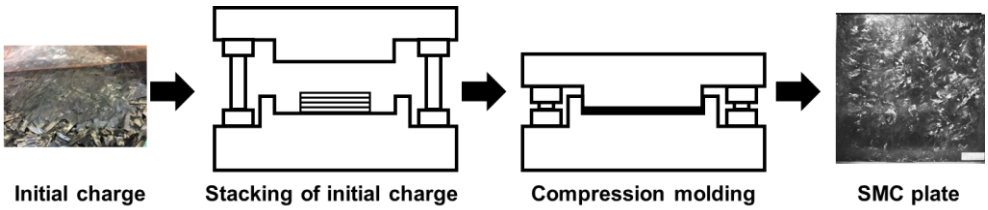

Figure 1.3. The manufacturing process for SMC composite

1.3 Literature Review

Despite the great performance and lightweight structure of SMC composite, due to the complex flow pattern during the compression molding process, the final molded parts feature a spatially varying distribution of fiber bundles. Therefore, considerable inhomogeneity and anisotropy are commonly observed and pose a tremendous challenge to predicting SMC composites' behavior in simulations. As a result, repeated experiments were conducted to determine the behavior of the initial SMC composites. However, with the advancement of modeling techniques, numerous studies have been conducted on developing multiscale modeling approaches for SMC composites to account for these inherent features. The critical importance herein is developing a homogenization method to estimate the effective properties of micro and mesoscopic models. There are many ways for modeling SMC composite in the literature review. The first is the analytical homogenization method which is also described as the micromechanics method. It has been exploited based on Eshelby's theory which is the basis of the self-consistent and Mori-Tanaka (MT) methods [7, 13-15]. Inclusions are modeled as the distinct phase in the matrix-surrounded region, and the strain fields are characterized and expressed as strain

concentration tensors. By employing an orientation averaging process, this method can also be applied to predicting the properties of random fiber composites.

SMC modeling is first implemented based on the randomly oriented discontinuous fiber composites using the micromechanics-based scheme [16, 17]. They endeavored to represent a theoretically complex interaction between the short fibers and the surrounding matrix, both globally and locally. The proposed micromechanics model predicted the point-wise stresses in the fiber and the matrix including the stress state at fiber ends. A comparison of the predicted stiffness properties with experimental data demonstrated its validity. Next, Fitoussi developed a statistical micro-macro relationship with the help of the model of MT [18-20]. In the case of an SMC composite with a 32% fiber volume fraction, debonding at the fiber/matrix interfaces is predominant in a micro-damage mechanism. They introduced a statistical local damage criterion and the concept of the equivalent damaged inclusion in the micro-macro relationship of Mori and Tanaka. Based on this approach, there are various attempts to predict the mechanical properties of SMC composites. Anagnostou et al. adopted the Mori-Tanaka scheme through a two-step homogenization [21]. They first homogenized effective properties from the microstructure of the fiber bundle. After that, the macroscopic behavior of SMC composites was calculated through the second homogenization from the mesostructure. This approach evaluated the effective viscoelastic behavior of fiber bundles and SMC plates by accounting for the time dependence. Furthermore, Görthofer et al. investigated the influence of the microstructural parameters through a sensitivity analysis [22]. They evaluated the effective elastic properties of SMC

composites through the Mori-Tanaka method by changing microstructural input parameters such as the elastic moduli, the volume fraction of the constituents, and the orientation of fiber. They presented influential parameters in predicting the overall mechanical behavior. Recently, Tamboura et al. presented the multiscale approach to predict the stiffness reduction of SMC composites subjected to low cycle fatigue loading [23]. By considering the local cyclic normal and shear stress at the interface, the fiber-matrix interface damage criterion was introduced in the Mori-Tanaka method to predict the loss of stiffness.

Like the micromechanics approach, the classical laminated plate theory (CLPT) was also applied to the SMC composite by representing inclusion as a parallel layer of in-plane randomly oriented fibers [24, 25]. When using the CLPT method to analyze laminate composite structures, they have the advantage of minimizing computational resources. However, although proven successful in predicting macroscale behavior through numerous studies, the micromechanics-based method and CLPT still have a limitation in capturing local phenomena. Thus, it cannot account for spatial variation and uncertainty in the micro/mesostructure in SMC composites, which is inferred neither of the methods can accurately predict the nonlinear material properties.

To resolve this problem, the finite element (FE)-based computational method defining the representative volume element (RVE) have been developed. With the advancement of computing power, it is possible to implement complex microstructures using FE modeling. It can accurately predict composites' local behavior as well as overall elastic behavior. Especially, a micro-computed

tomography (CT) images-based high-fidelity RVE generation in FE modeling is the most advanced way of reflecting microstructural morphologies accurately [26-28]. However, unlike simple micro or mesostructure such as cross-ply laminate or particulate composites, SMC composites have a complex mesostructure from the compression molding process. Despite the fact that incorporating microstructure and mesostructure into the model improves its predictive capabilities, significant computational costs are inevitable [27]. Moreover, the deviation caused by random fiber bundle locations should be considered in the RVE modeling. Therefore, a cost-efficient multiscale modeling method is needed for predicting the mechanical behaviors of chopped carbon fiber SMC. Micro/mesostructure reconstruction is a key component of the multiscale modeling of SMC composite materials. The goal is to generate in-silico digital structural models. As a result, many efforts have been attempted to create a stochastic RVE that is statistically equivalent to the real-life microstructural information of the composite.

Initial SMC studies based on a Voronoi diagram were conducted [29]. Each Voronoi cell models have a fiber bundle region with a distinct orientation [30]. It was able to represent a mesostructure of SMC composite by assigning representative orientation to partitioned Voronoi cells. Because it has factitious morphology with the Voronoi diagram, it was not amenable to observe the local behavior of constituents. Therefore, only macroscopic elastic behavior was evaluated in their study. However, it was a valuable approach for SMC composites in that the statistical information of fiber orientation is utilized in the stochastic reconstruction of SMC composites. Further study is conducted on a CT-image-based SMC model [31]. The

most widely used method is based on an algorithm of random sequential adsorption (RSA). It sequentially put the inclusions on the target domain while they do not overlap with previously adsorbed inclusions. It is proceeding until the prepared number of inclusions is totally consumed. RSA has been widely employed to construct RVE for particulate and short-fiber composites [32]. Although RSA is an efficient way to construct the microstructure of composite materials, a limitation to reaching a high volume fraction happens. Likewise, other kinds of reconstruction algorithms, such as the Monte Carlo method and series expansion have the same problem in terms of high volume fraction. Chen et al. developed a reconstruction algorithm to construct SMC plates based on the modified RSA [33]. They sequentially packed the SMC fiber bundles and accounted for overlap through a rise and sink methodology. This study broke down the limitation of volume fraction in RSA and presented an effective modeling technique by successfully generating an SMC mesostructure that is statistically equivalent to the orientation tensor. In this study, they extracted specimens from the reconstructed SMC plate. Depending on the locations on the plate, elastic modulus showed different results because of fiber bundles' distribution which is characterized during the compression molding process.

Based on the SMC modeling techniques, damage modelings have been conducted based on the major failure modes of SMC composites. Four major failure modes are observed in SMC composites: matrix cracking, bundle splitting/breakage, and bundle-matrix interface failures. Following the constituents' failure patterns, nonlinear models are employed to represent the damage manifestation of the SMC composite under external loadings. Chen et al. [34] first developed material

constituents in the SMC mesostructure to capture their mechanical behavior. With the proposed study, SMC damage analysis was performed using explicit analysis. The failure process observed in experiments was well captured using computational simulation. Moreover, Tang et al. proposed failure criteria for bulk SMC composites using computational simulations [35]. Depending on the fiber orientation, modified failure criteria were created. However, the characterized envelope can not guarantee in the case of the other type of composite (different types of constituents and mesostructure geometry of SMC composites). Above all, the presented studies can not capture the deviation of output (modulus and strength). These SMC studies mainly focused on the averaged mechanical properties rather than their scattering because the orientation-based SMC RVE modeling yields relatively consistent results of modulus and strength. In particular, the strength of SMC composites shows a more significant scattering than the modulus because of the random dispersion (i.e., the local volume fraction of fiber bundles) effect [36]. Therefore, the next study should cover the statistical investigation of the SMC composite to reflect real-life SMC composites' features and guarantee its performance.

Based on the review of SMC composite using computational work, it is important to develop accurate and efficient SMC modeling and analysis for predicting performance and extending its capability to the design area. In this dissertation, statistical modeling and analysis using computational simulation will be presented by representing not only the average value but also the deviation of output [37, 38]. In the literature, the SMC mesostructured was generated considering only the orientation tensor of the fiber bundles by an orientation averaging scheme of Advani

and Tucker [39]. Based on the orientation from commercial compression moldings analysis software, such as Moldflow, Moldex3D, and PAM-COMPOSITES, the SMC RVE was generated with a statistically matching orientation tensor [30, 33, 40]. In this study, the dispersion of the fiber bundle in the SMC plate will be taken into account in the reconstructional modeling. This idea was highly inspired by Kim and Yun's work, which demonstrated the variation in mechanical properties according to the dispersion of inclusion in particle-reinforced composites through principal component analysis (PCA) [1].

1.4 Aims and Scope

In the dissertation, multiscale modeling and analysis for SMC composite are presented using finite element (FE) and micromechanics-based modeling. First, SMC modeling is realized with a stochastic reconstruction algorithm. As a manufacturing-based parameter that can be a result of the compression molding process, orientation and dispersion of the fiber bundles in the SMC plate are used as statistical indicators in the reconstruction modeling. To represent complex distribution in terms of statistical indicators, averaging tensors are replaced for the direct probabilistic distribution functions (PDF). Moreover, during the packing process in the reconstruction algorithm, overlapping between the fiber bundles is implemented to construct high-volume fraction composites and represent undulation of the fiber bundle which can determine through the thickness geometry of the SMC

plate. Based on the reconstructed modeling linear analysis and nonlinear analysis are conducted to predict the modulus and strength of SMC composites.

Second, micromechanics-based modeling is employed to predict the properties of SMC composites more efficiently. Three homogenization steps are sequentially conducted. Wavy fibers are investigated in the modeling. The chopped carbon fiber reinforced composites show wavy fibers, which is a type of manufacturing defect commonly found in composite material parts. It is important to understand how the presence of waviness affects the performance of SMC composites [41, 42].

The novel contribution of the dissertation can be summarized as follows.

i. Three-dimensional (3D) reconstruction modeling is proposed to construct SMC mesostructured.
ii. Strength prediction in linear finite element (FE) analysis is evaluated using the averaging scheme in the matrix domain.
iii. Damage patterns on SMC composites are characterized and applied in the FE model as constituents models to demonstrate the damage manifestation in the simulation.
iv. The influence of orientation and dispersion of the fiber bundles in the SMC plate is investigated in terms of overall mechanical performance.
v. The effect of fiber bundles' waviness is considered through the micromechanics model.
vi. Both direct-FE simulation and micromechanics model show good agreement with the experimental result.

1.5 Outline of Dissertation

To provide an outline of this dissertation, the contents of the chapters are presented as follows.

In Chapter 2, the basic theory of multiscale analysis is introduced: FE-based direct numerical simulation (DNS) and micromechanics-based Mori-Tanaka method. This chapter discusses each feature of homogenization methods and results.

In Chapter 3, a microstructure modeling of sheet molding compound (SMC) composites is presented using manufacturing parameters. A stochastic reconstruction algorithm is developed for microstructure. Based on the orientation and dispersion of fiber bundles, the mesostructure is constructed for FE analysis. The linear behavior of composites is evaluated and compared with the experimental outcome.

In Chapter 4, damage assessment is quantified using material constitutive modeling in mesoscale. Damage mechanisms are considered in constituents as materials constitutive models. Progressive damage analysis is performed through nonlinear FE analysis. The damage patterns of SMC composites are characterized depending on the fiber bundles' orientation and dispersion. Finally, its validity is further demonstrated by experimental comparison.

In Chapter 5, to reduce computational cost and time, micromechanics modeling for SMC composites is presented. There are three steps for homogenization in terms of a fiber bundle, SMC layer, and SMC composite. The wavy fiber is implemented using a polynomial mathematical expression. The overlapping between the fiber bundles is also considered through multi-site (MS) Mori-Tanaka (MT) modeling. Finally, Validation is conducted with results from the literature.

Chapter 2. Multiscale Analysis for Composite Materials

2.1 Study Background

The multi-scale method originated in the field of micromechanics, where an analytical homogenization method was first proposed [43]. It has the disadvantage of only being applicable to linear materials, small deformations, simple morphological structures, and simple material models. It is therefore limited in explaining complex microstructures and/or nonlinear hysteresis-dependent configurational behavior. In recent decades, in order to compensate for the shortcomings of analytical methods, computational methods have been developed [44]. It allowed for the analysis of very complex microstructures and provided access to more microscopic phenomena. Due to the increase in computing power, they have been the subject of strong scientific interest. It is especially useful in many fields because it allows digital design and optimization of microstructures of composite materials [45]. This avoids numerous design and prototype manufacturing through trial and error testing. By using multiple combinations of model parameters, it is easier and faster to perform digital complex tests by taking into account shape, mechanical properties, size, and topology.

The computational multi-scale method is characterized by the consideration of multiple successive points on the large-scale domain and the definition of a representative volume element (RVE) of microstructure [46, 47]. RVE composed of two or more components can be discretely separated and be considered to have

continuous deformation [48]. Large-scale variables are produced in low-scale calculations by defining and successively solving stress- or strain-based boundary value problems (BVP) for representative volume elements [49-52]. Homogenization is a technique used to calculate equivalent material behavior based on RVE on a small scale. This term is derived from the concept that the behavior of an inhomogeneous material can be predicted by replacing it with an equivalent homogeneous continuum, as shown in Figure 2.1.

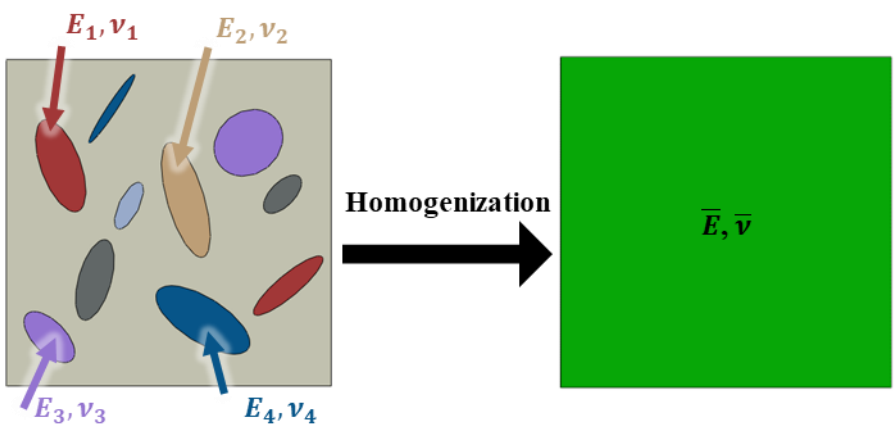

Figure 2.1. A concept of homogenization

Defining the RVE is the most significant step in evaluating the equivalent behavior through homogenization. By specifying the RVE more precisely or making it larger, it is possible to obtain a simulation result similar to the actual value, but it needs tremendous calculation cost. Therefore, it is necessary to define the RVE that is capable of representing the distinct features of the microstructure.

Homogenization methods are based on the volume averaging schemes of field variables calculated by solving a boundary value problem (BVP) of heterogeneous microstructures [53]. It can be seamlessly integrated within the multilevel finite element (FE^2) multiscale analysis framework. This approach can solve microstructure problems at every integration point in the macroscale model concurrently [54]. Its advantage is that it intuitively illustrates the microstructure's deformation. However, the FE^2 multiscale approach is computationally expensive especially when the model has material or geometric nonlinearities. On the other hand, there are analytical homogenization models for two-phase composites. The methods can comprise Voigt and Reuss approximations (rule of mixers) [55], Hashin-Shtrikman type bounds [56, 57], Mori-Tanaka type models [58], and classical self-consistent schemes [59]. Voigt (arithmetic mean) and Reuss (harmonic mean) are the most basic boundaries for the elastic modulus of composite materials. Hasin and Shtrikman extended boundaries to derive upper and lower bounds for the effective elastic modulus of quasi-isotropic and quasi-uniform polyphase materials of arbitrary topology. This method gives a reliable estimate of the boundaries for elastic modulus if the ratio of phase modulus to each other is not too large. The majority of predictions of the macroscopic properties of two-phase composites have focused on showing boundaries for various moduli of elasticity [60]. Such boundaries depend only on the relative volumes of each constituent and do not reflect any geometry, except when fibers are constantly aligned. Mean-field homogenization (MFH) method which is based on Eshelby's theory [13] provides a relatively accurate solution to the elastic problem [61]. In particular, the defining

interaction of the inclusion enables the consideration of the shape design of the microstructure. It includes Mori-Tanaka (MT) and self-consistent schemes. The MFH methods are semi-analytical, computationally efficient, and suitable for multiscale simulations. Among them, the MT micromechanics model has been constantly increasing attraction from the composites community since it was originally developed. Each Numerical and mean-field homogenization is summarized in Figure 2.2.

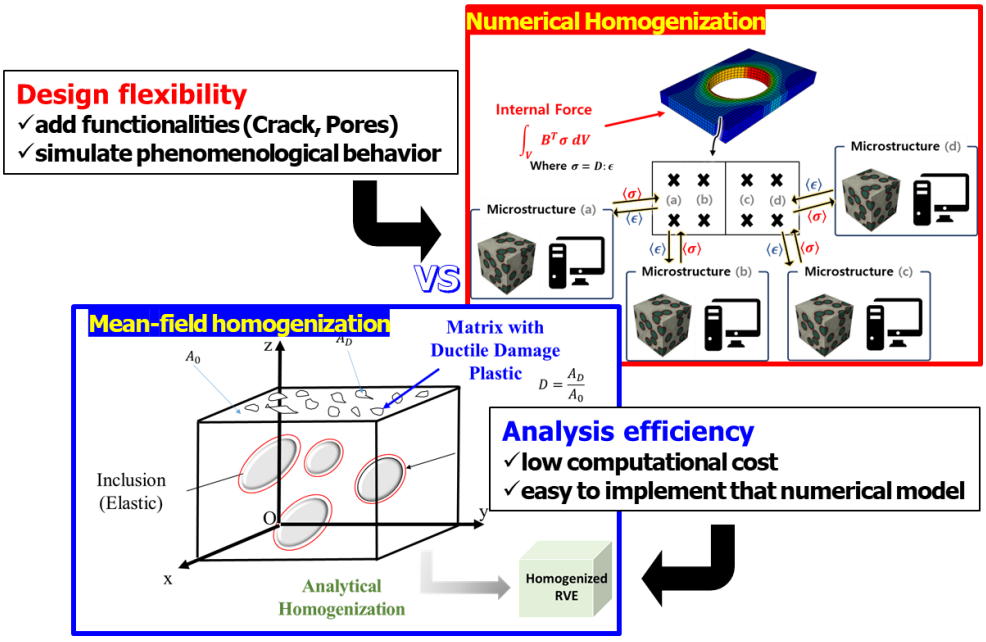

Figure 2.2. Comparison between computational and analytical homogenization

This chapter will cover the computational homogenization method using finite elements and the Mori-Tanaka method using MFH. It is the goal of both methods to achieve equivalent properties and equivalent behavior of SMC composites. In

Chapters 3-5, the equivalent properties of SMC composites are calculated using these methods.

2.2 FE-based Homogenization Method

Here, this section describes the procedure of evaluating effective properties and equivalent behaviors by defining the microscale problem using the finite element method (FEM). Since the microstructure of composite materials is directly solved, this method is known as direct numerical simulation (DNS). In Chapters 3 and 4, FE-based numerical simulation is conducted to evaluate the effective properties and equivalent behaviors of the fiber bundle in SMC composite. The detailed theory and equations are detailed below.

2.2.1 Problem at the microscale

At the micro-scale problem, we assume that the micro-scale problem is considered in domain Θ. In the notation, ($\tilde{}$) represents microscopic quantities. In this scale, The equilibrium equation can be described in the same way as the macro-scale problem.

$$\mathrm{div}\tilde{\boldsymbol{\sigma}}(x) + \boldsymbol{f}_B = 0 \tag{2.1}$$

where $\tilde{\sigma}(x)$ is the Cauchy stress tensor at any point $\bar{x}$ in the macro-scale structure and $\boldsymbol{f_B}$ is the body force that is neglected in micro-scale problems. Regarding the boundary value problem, the heterogeneous composite material on a micro-scale can be presumed to be made of the infinite number of periodic arrangements of identical

cells such that its behavior can be predicted by analyzing one of the cells. When the material is not periodic then it is often possible to define RVE which typifies the representative features. To analyze the behavior at the micro-scale, the RVE should be conducted with appropriate loading and boundary conditions. The RVE should have features such that the neighboring RVE must fit into each other in both deformed and un-deformed states. Hence the boundary condition for the RVE should be periodic in order to preserve the continuity of displacements, strains, and stresses across each RVE. For implementation in FEM, the boundary conditions can be expressed as linear constraints and they are implemented as multipoint constraints. Various types of boundary conditions will be discussed in the following sections. Regarding the constitutive relation, we can prescribe various constitutive matrixes for linear or non-linear. The homogenization procedure which provides the macroscopic stress as a function of microscopic stresses involves a volume-averaging relationship and is provided as follows:

$$\bar{\boldsymbol{\sigma}} = \langle \tilde{\boldsymbol{\sigma}}(\bar{x}) \rangle = \frac{1}{|\Theta|} \int_{\Theta} \tilde{\boldsymbol{\sigma}}(\bar{x}) d\Theta = \bar{\boldsymbol{C}} : \bar{\boldsymbol{\varepsilon}} \tag{2.2}$$

where $\bar{\boldsymbol{\sigma}}$, $\bar{\boldsymbol{\varepsilon}}$, and $\bar{\boldsymbol{C}}$ are the macroscopic stress, strain, and homogenized linear constitutive matrix, respectively. In case of a nonlinear relationship can be described as follows:

$$\Delta\bar{\boldsymbol{\sigma}} = \langle \tilde{\boldsymbol{\sigma}}(x) \rangle = \bar{\boldsymbol{C}}^{\mathrm{t}} : \Delta\bar{\boldsymbol{\varepsilon}} \tag{2.3}$$

where $\bar{\boldsymbol{C}}^{\mathrm{t}}$ is the homogenized tangent constitutive matrix which depends on the linear elastic properties of micro-scale constituents.

The linear analysis performs a single analysis at the macroscale, not an iterative analysis for convergence in a typical nonlinear analysis. For this reason, the constitutive matrix on the microscale can be repeatedly calculated for each integration point of the macroscale level, or the constitutive matrix which is calculated by performing only one micro-scale problem can be assigned to the entire integration point. In the linear problem, both methods produce the same results and the latter case can deal with the problem much more efficiently.

2.2.2 Boundary value problem of RVE

There are various boundary conditions such as kinematic uniform boundary condition (KUBC), static uniform boundary condition (SUBC), and periodic boundary condition (PBC), as shown in Table 2.1. Homogeneous fields are produced by applying external loads on the surface of a homogeneous body [62]. However, fluctuations of the stress and strain fields are obtained in heterogeneous materials and have an on influence the macroscopic behavior. SUBC consists in applying on the boundary the stress vector field that would occur if the stress were uniform inside the RVE. In the same manner, KUBC consists of the displacement field. PBC is theoretically related to structures with periodic cells and media that can be defined by periodic changes. PBC assumes that strains and stresses are periodic at the cell (defined as RVE) level. The periodicity of stress and strain can lead to the specific periodic boundary condition for the localization problem of RVE.

Table 2.1. Boundary conditions for RVE

	SUBC	PBC	KUBC
Equation	$t_i(\Gamma) = \sigma_{ij}^0 n_j$	$u_i = \varepsilon_{ij}^0 x_j + u_i^*$	$u_i(\Gamma) = \varepsilon_{ij}^0 x_j$
Average	$\bar{\boldsymbol{S}} = \frac{1}{\lvert\Theta\rvert}\int_\Theta \tilde{\boldsymbol{\varepsilon}} d\Theta$	$\bar{\boldsymbol{C}} = \frac{1}{\lvert\Theta\rvert}\int_\Theta \tilde{\boldsymbol{\sigma}} d\Theta$	$\bar{\boldsymbol{C}} = \frac{1}{\lvert\Theta\rvert}\int_\Theta \tilde{\boldsymbol{\sigma}} d\Theta$
Concept	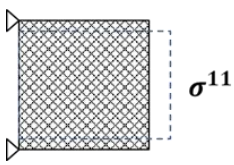	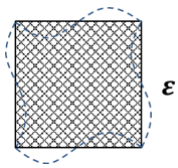	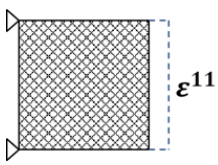

These boundary conditions lead to distinct estimates of the stiffness of a given RVE. The behavior is no longer dependent on boundary conditions if the RVE is large enough [63]. However, it is computational wasting for constructing large RVE. Typically, the effective property is overestimated under KUBC whereas underestimated under SUBC as provided by Vogit-Reuss and Hashin-shtrikman theoretical bounds [56]. Here, the choice of boundary conditions is restricted by the geometry of RVE. In the case of microstructures having pores, there is a limitation in implementation because stress vectors must be applied to the pores in SUBC. Among them, PBC can describe the phenomenological behavior of the composite microstructures and show the best convergence as the RVE size increases [46]. Figure 2.3 shows the relationship of the effective property depending on the boundary condition for homogeneous and heterogeneous media.

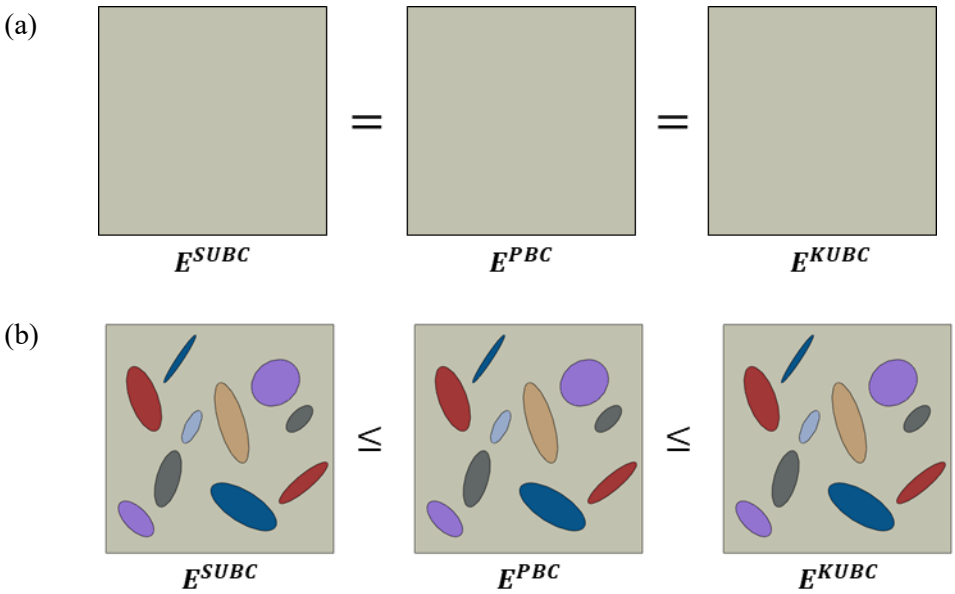

Figure 2.3. Relationship between boundary conditions: (a) homogeneous media, (b) heterogeneous media

In order to implement PBC using ABAQUS, this can be carried out via linear constraints and described as explicit form.

$$u_i^- - u_i^+ - \Delta L_x \epsilon_{i1} - \Delta L_y \epsilon_{i2} - \Delta L_z \epsilon_{i3} = 0 \tag{2.4}$$

where where u_i^- is the displacement of the node on slave region $(-)$ and u_i^+ is the displacement of the node on the master region $(+)$. i is x, y, and z in the Cartesian coordinate system. ΔL_i is the relative distance between two nodes. Using the following equation, the nodes on the 3D RVE can be grouped by their every location, that is, surface nodes, edge nodes, and vertex nodes because their relative distances are different depending on the group and this grouping prevents nodes from being over-constrained

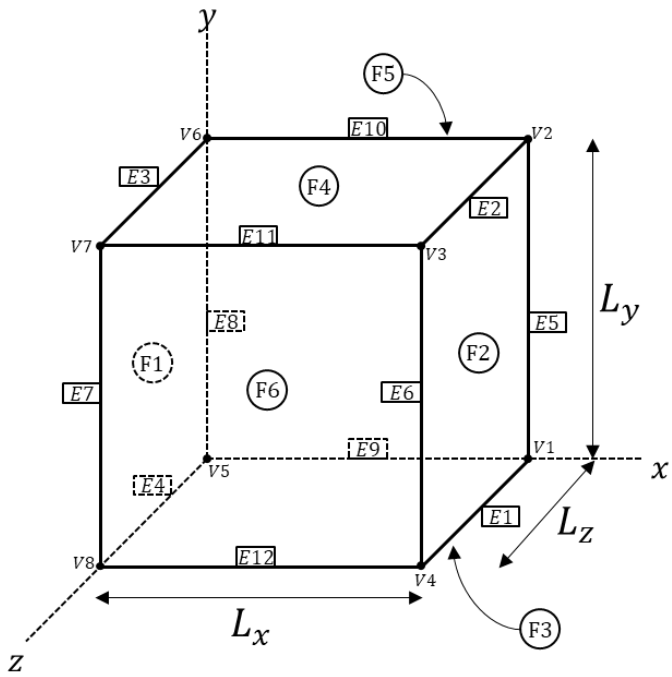

Figure 2.4. Notations for kinematic PBC equation

As shown in Figure Figure 2.4, Eq. (2.5) can be decomposed into regions where nodes are located: surfaces, edges, and vertices.

$$\text{Nodes of the faces: } \begin{cases} \mathrm{u}_\mathrm{i}^{F2} - \mathrm{u}_\mathrm{i}^{F1} = L_x \varepsilon_{i1} \\ \mathrm{u}_\mathrm{i}^{F2} - \mathrm{u}_\mathrm{i}^{F1} = L_x \varepsilon_{i1} \\ \mathrm{u}_\mathrm{i}^{F2} - \mathrm{u}_\mathrm{i}^{F1} = L_x \varepsilon_{i1} \end{cases}$$

$$\text{Nodes of the edges: } \begin{cases} \mathrm{u}_\mathrm{i}^{E2} - \mathrm{u}_\mathrm{i}^{E4} = L_x \varepsilon_{i1} + L_y \varepsilon_{i2} \\ \mathrm{u}_\mathrm{i}^{E1} - \mathrm{u}_\mathrm{i}^{E3} = L_x \varepsilon_{i1} - L_y \varepsilon_{i2} \\ \mathrm{u}_\mathrm{i}^{E6} - \mathrm{u}_\mathrm{i}^{E8} = L_x \varepsilon_{i1} + L_z \varepsilon_{i3} \\ \mathrm{u}_\mathrm{i}^{E5} - \mathrm{u}_\mathrm{i}^{E7} = L_x \varepsilon_{i1} - L_z \varepsilon_{i3} \\ \mathrm{u}_\mathrm{i}^{E11} - \mathrm{u}_\mathrm{i}^{E9} = L_y \varepsilon_{i2} + L_z \varepsilon_{i3} \\ \mathrm{u}_\mathrm{i}^{E10} - \mathrm{u}_\mathrm{i}^{E12} = L_y \varepsilon_{i2} - L_z \varepsilon_{i3} \end{cases} \tag{2.5}$$

Nodes of the edges: $\begin{cases} \mathrm{u}_\mathrm{i}^{V3} - \mathrm{u}_\mathrm{i}^{V5} = L_x\varepsilon_{i1} + L_y\varepsilon_{i2} + L_z\varepsilon_{i3} \\ \mathrm{u}_\mathrm{i}^{V2} - \mathrm{u}_\mathrm{i}^{V8} = L_x\varepsilon_{i1} + L_y\varepsilon_{i2} - L_z\varepsilon_{i3} \\ \mathrm{u}_\mathrm{i}^{V7} - \mathrm{u}_\mathrm{i}^{V1} = -L_x\varepsilon_{i1} + L_y\varepsilon_{i2} + L_z\varepsilon_{i3} \\ \mathrm{u}_\mathrm{i}^{V4} - \mathrm{u}_\mathrm{i}^{V6} = L_x\varepsilon_{i1} - L_y\varepsilon_{i2} + L_z\varepsilon_{i3} \end{cases}$

In the case of well-made mesh, the mesh of each opposite side matches well. However, for RVE with non-matching FE meshes on the facing surfaces, edges, and vertices, it is obscure to apply the kinematic PBC to FE nodes. To resolve the PBC issue in RVE for non-matching meshes, an efficient numerical method is proposed herein. Projecting nodes in the slave region onto the master region, all slave nodes fall into one of the elements on the master region. Depending on the slave node position, displacements of the slave nodes are constrained to weight nodal displacements of the element on the master region as

$$\mathrm{u}_\mathrm{i}^{\mathrm{j}-} - \sum_{k=1}^{n} [W_k u_{ik}^{j+}] - \Delta\mathrm{L}_\mathrm{x}\epsilon_{\mathrm{i}1} - \Delta\mathrm{L}_\mathrm{y}\epsilon_{\mathrm{i}2} - \Delta\mathrm{L}_\mathrm{z}\epsilon_{\mathrm{i}3} = 0 \tag{2.6}$$

where weighting factors W_k are calculated by the shape functions of the element, and n is the number of nodes of the element. These weighting factors are specified in multipoint constraints with the associated nodes. To determine the weighting factors, the following nonlinear simultaneous equations are solved by the Newton-Raphson method.

2.2.3 Results of FE-based direct numerical homogenization

Using the FE-based direct numerical homogenization (DNS), the effective properties of Boron/Aluminum composites are calculated. Cylinder-shaped boron

fiber is placed along the x-direction. The boron fiber has a volume fraction of 0.47 and is bounded perfectly with the aluminum matrix. FE model of boron/aluminum composite consists of 1880 hexahedral meshes, and the properties of constituents are listed in Table 2.2.

Table 2.2. Material properties of constituents

	Boron	Aluminum
Element number	1040	840
Volume fraction	0.47	0.53
Young's Modulus	379.3	68.3
Poisson's Ratio	0.1	0.3

Figure 2.5 shows the stress contours by applying unit strain in each direction to the RVE under PBC. The effective properties of RVE are obtained by the volume average of the stresses at gauss points.

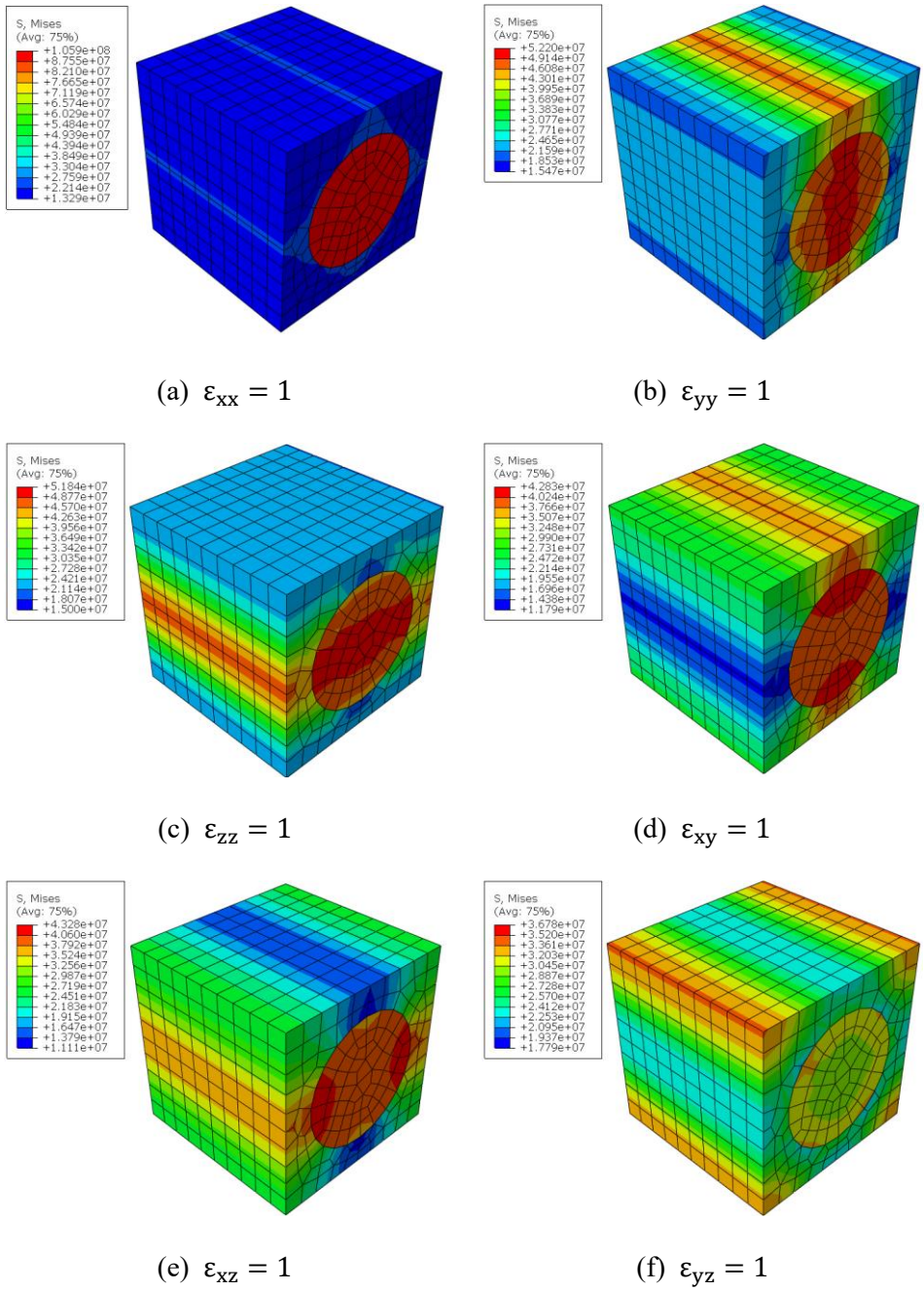

(a) $\varepsilon_{xx} = 1$ (b) $\varepsilon_{yy} = 1$

(c) $\varepsilon_{zz} = 1$ (d) $\varepsilon_{xy} = 1$

(e) $\varepsilon_{xz} = 1$ (f) $\varepsilon_{yz} = 1$

Figure 2.5. Stress contours of RVE under PBC

Table 2.3 shows a comparison of effective properties between homogenization models and an experiment. It is easy to calculate effective properties using ROM based on the volume fraction of each constituent. Although a longitudinal property is well predicted where the fibers are aligned, the transverse and shear moduli are significantly different from the experimental output. Hasin-Rosen and Halpin-Tsai were proposed to supplement the shortcomings of the existing analysis technique. Nevertheless, it is hard to predict the effective properties of the composite simultaneously in all directions. On the other hand, FE-based DNS under PBC provides a good agreement with experimental values for longitudinal, transverse, and shear modulus, and enables the implementation of complex microstructures that can go beyond the simple microstructure shown in this example.

Table 2.3. The experimental properties and outputs from different homogenization models [64]

	ROM	Hashin-Rosen	Halpin-Tsai	PBC	Experiment
E_1	214.3	214.4	214.3	214.8	216
E_2	111.1	111.1	134.5	143.2	140
ν_{12}	0.21	0.20	0.21	0.19	0.29
ν_{23}	0.27	0.27	0.27	0.25	-
G_{12}	43.70	54.01	61.10	54.27	52
G_{23}	43.70	43.70	43.70	45.77	-

2.3 Micromechanics-based Homogenization Method

Here, the basic theory for the Mori-Tanaka method is described. An iterative procedure to update the global strain concentration tensor is presented for nonlinear analysis. The results of MT for ductile damage behavior are verified with the FE-based DNS. An MFT-based MT model is employed to calculate the effective properties and equivalent behaviors of SMC composites [65]. The detailed theory and equations are detailed below.

2.3.1 Kinetmatic integral equation

In this section, the basics of the micromechanics model based on the Mori-Tanaka scheme are presented to obtain the effective properties of composites. A representative volume element Ω of composite material is assumed to obey Hooke's law. Let $\boldsymbol{\Sigma}$ and $\boldsymbol{E}$ be the global strain and stress tensors such that:

$$\boldsymbol{\Sigma} = \boldsymbol{C}^{eff} : \boldsymbol{E} \tag{2.7}$$

Here, $\boldsymbol{C}^{eff}$ is the global fourth-order elastic tensor. The operator "**:**" stands for the tensorial contraction over two indices. Hooke's law is supposed to be valid on the local levels and this relationship can be applied for each point, r of the representative volume element (RVE) as

$$\boldsymbol{\sigma}(r) = \boldsymbol{c}(r) : \boldsymbol{\varepsilon}(r), \tag{2.8}$$

where $\boldsymbol{\sigma}$, $\boldsymbol{\varepsilon}$**,** and $\boldsymbol{c}$ are the local stress, strain, and elasticity tensors, respectively. r is the position vector in the domain Ω. The volume-averaging of the local stress and strain gives macroscopic stress and strain, as follows:

$$\boldsymbol{\Sigma} = \frac{1}{\Omega}\int_{\Omega} \boldsymbol{\sigma}(r) d\,\Omega$$

$$\boldsymbol{E} = \frac{1}{\Omega}\int_{\Omega} \boldsymbol{\varepsilon}(r) d\,\Omega, \tag{2.9}$$

The macroscopic stress and strain are obtained under homogeneous boundary conditions of the Dirichlet and Neumann type in the absence of body force and inertia terms. The strain is first localized from the macroscopic strain tensor. This is defined in Eq. (2.10),

$$\boldsymbol{\varepsilon}(r) = \boldsymbol{A}(r) : \boldsymbol{E}. \tag{2.10}$$

Here, $\boldsymbol{A}$ is the fourth-order global strain concentration tensor and an unknown tensor which contains all information about the microstructure. From Eq. (2.7) ~ (2.10), the effective properties of the RVE are determined as follows:

$$\boldsymbol{C}^{eff} = \frac{1}{\Omega}\int_{\Omega} \boldsymbol{c}(r) : \boldsymbol{A}(r) d\Omega \tag{2.11}$$

For the inhomogeneous domain, the unknown global strain concentration tensor $\boldsymbol{A}$ is determined from a kinematic integral solution with a Green tensor for the infinite body with the homogeneous reference properties. Accordingly, the local stiffness tensor is decomposed into a homogeneous reference part $\boldsymbol{c}^R$ and a fluctuation part $\delta\boldsymbol{c}$. These are defined in Eq. (2.12),

$$\boldsymbol{c}(r) = \boldsymbol{c}^R(r) + \delta\boldsymbol{c}(r). \tag{2.12}$$

In terms of the stiffness decomposition and strain fields, the kinematic integral equation is expressed as

$$\boldsymbol{\varepsilon}(r) = \boldsymbol{E}^R(r) - \int_{\Omega} \boldsymbol{\Gamma}(r - r') : \delta \boldsymbol{c}(r') \boldsymbol{\varepsilon}(r') d\Omega', \tag{2.13}$$

where $\boldsymbol{E}^R(r)$ is the strain field inside the reference infinite medium, $\boldsymbol{\Gamma}(r - r')$ is the modified Green tensor, and $\delta \boldsymbol{c}(r')$ is the deviation part of local properties from the properties of the reference medium. Vieville et al. presented an iterative procedure to update the global strain concentration tensor [66].

2.3.2 Iterative update of global strain concentration: Mori-Tanaka Model

With the assumption that the RVE is composed of N types of reinforcements and a surrounding matrix which is labeled as a constituent number 0. We admit that the geometry of reinforcements can be approached by particulate inclusions. As a consequence, the composite is made up of *(N+1)* constituents. The volume fraction of a given *I*, or family of the same type of inclusions, is denoted by $f^I = \Omega^I / \Omega$. It is inferred that the properties of each constituent are homogeneous inside the constituent. This tensor is obtained based on an iterative procedure. The global strain concentration tensor $\boldsymbol{A}^I(r)$ for the $I - th$ phase of the RVE is given as

$$\begin{aligned} &\boldsymbol{A}^I(r) = \boldsymbol{a}^I(r) : \left(\overline{\boldsymbol{a}}^I(r)\right)^{-1} \text{ where } \overline{\boldsymbol{a}} = \frac{1}{\Omega} \int_{\Omega} \boldsymbol{a}^I(x) d\Omega \\ &\overline{\boldsymbol{A}}(r) = \boldsymbol{I}, \end{aligned} \tag{2.14}$$

where $\boldsymbol{I}$ represents the fourth-order symmetric identity tensor and all notations in the form of $(\bar{\cdot})$ are the mean-field volume average of $(\cdot)$. $\boldsymbol{a}^I$ is the quantity of the local strain concentration tensor which relates the macroscopic strain of the reference medium with the local strain as follows:

$$\boldsymbol{\varepsilon}^I(r) = \boldsymbol{a}^I(r) : \boldsymbol{E}^R \tag{2.15}$$

Taking into account the interaction among different types of phases, the iterative equation for the local strain concentration tensor $\boldsymbol{a}^I$ is expressed as

$$\boldsymbol{a}_0^I(r) = \boldsymbol{I}$$

$$\boldsymbol{a}_{i+1}^I(r) = \left[\boldsymbol{I} + \boldsymbol{T}^{II} : \left(\boldsymbol{c}^I(r) - \boldsymbol{c}^R(r)\right)\right]^{-1} : \left[\boldsymbol{I} - \sum_{J=0, J\neq I}^{N} \boldsymbol{T}^{IJ} : \left(\boldsymbol{c}^I(r) - \boldsymbol{c}^R(r)\right) : \boldsymbol{a}_i^J(r)\right] \tag{2.16}$$

$$I = 0,1,\ldots,N,$$

where N is the number of phases. In Eq. (2.16), $\boldsymbol{a}_i^I$ represents an approximation of the Ith concentration tensor at the i-th iteration. $\boldsymbol{T}^{II}$ and $\boldsymbol{T}^{IJ}$ are the interaction tensors in on-site (OS) and multi-site (MS) versions, respectively. The OS approximation considers only interaction between the surrounding matrix and the inclusions while the MS approximation considers all interactions between different types of inclusion. Their general expression is such that:

$$\boldsymbol{T}^{IJ} = \frac{1}{\Omega_I} \int_{\Omega_I} \int_{\Omega_J} \boldsymbol{\Gamma}(r - r') d\Omega d\Omega' \tag{2.17}$$

This interaction tensor depends on the assumption of the properties of homogeneous reference medium such as $\mathbf{c}^R$ and $\mathbf{E}$. In the case of the Mori-Tanaka theory, $\boldsymbol{c}^{\mathrm{R}} = \boldsymbol{c}^0$ and $\boldsymbol{E}^0 = \boldsymbol{\varepsilon}^0$ are assumed. In this case, the iterative equation for the local strain concentration tensor is reduced to Eq. (2.18).

$$\boldsymbol{a}_0^I(r) = \boldsymbol{I}$$

$$\boldsymbol{a}_{i+1}^I = [\boldsymbol{I} + \boldsymbol{T}^{II}(\boldsymbol{c}^R):(\boldsymbol{c}^I - \boldsymbol{c}^R)]^{-1}:\left[I - \sum_{J=1,J\neq I}^{N} \boldsymbol{T}^{IJ}:(\boldsymbol{c}^I - \boldsymbol{c}^R):\boldsymbol{a}_i^J\right] \tag{2.18}$$

, where $I = 0,1,\ldots,N$

Here, the term corresponding to $J = 0$ is removed owing to $\Delta\boldsymbol{c}^0 = \boldsymbol{c}^0 - \boldsymbol{c}^R = 0$ in Eq. (2.13). In the case of the OS version, Eq. (2.18) is not iterative anymore due to all the tensors $\boldsymbol{T}^{IJ} = 0$ ($I \neq J$), neglecting the interaction between inclusion I and J. The interaction tensor $\boldsymbol{T}^{II}$ can be deduced from the Eshelby's tensor $\boldsymbol{S}$ such as $\boldsymbol{T}^{II} = \boldsymbol{S}:(\boldsymbol{c}^R)^{-1}$. The Eshelby tensor for the spherical shape can be followed the literature [67]

Therefore, the local strain concentration tensor $\boldsymbol{a}^I$ takes a simplified expression as follows:

$$\boldsymbol{a}^I = [\boldsymbol{I} + \boldsymbol{S}:(\boldsymbol{c}^0)^{-1}:(\boldsymbol{c}^I - \boldsymbol{c}^0)]^{-1}, with\ I = 0,1,2,\ldots,N \tag{2.19}$$

As noted in Eq. (2.14), the inverse of the averaged local strain concentration tensor ($\overline{\boldsymbol{a}}^I(r)$) is required, which is obtained through the rule of mixture scheme as follows:

$$(\overline{\boldsymbol{a}}^I)^{-1} = \left(f^0\boldsymbol{I} + \sum_{I=1}^{N} f^I\boldsymbol{a}^I\right)^{-1} \tag{2.20}$$

Substituting Eq. (2.19) and Eq. (2.20) into (2.14), the global strain concentration tensor $\boldsymbol{A}^I$ is calculated as

$$\boldsymbol{A}^I = [\boldsymbol{I} + \boldsymbol{S}:(\boldsymbol{c}^0)^{-1}:(\boldsymbol{c}^I - \boldsymbol{c}^0)]^{-1} : \left(f^0\boldsymbol{I} + \sum_{I=1}^{N} f^I\boldsymbol{a}^I\right)^{-1}. \tag{2.21}$$

For nonlinear constituents, the global strain concentration can be iteratively updated depending on the updated constituents' stiffnesses $\boldsymbol{c}^{\mathrm{I}}$ and/or $\boldsymbol{c}^{0}$.

For a composite material consisting of N types of inclusions, the effective macroscopic stiffness tensor $\boldsymbol{C}^{eff}$ is given in terms of the local stiffness and the global strain concentration tensor as

$$\boldsymbol{C}^{eff} = \frac{1}{V}\int_{V} \boldsymbol{c}(r):\boldsymbol{A}(r)dV = \sum_{I=0}^{N} f_I \boldsymbol{c}^I:\boldsymbol{A}^I. \tag{2.22}$$

From Eq. (2.14), $\boldsymbol{A}^0$ and $\boldsymbol{A}^{\mathrm{I}}$ are expressed as

$$\begin{aligned} &\boldsymbol{A}^0 = \boldsymbol{a}^0:(\boldsymbol{a}^0)^{-1} = \boldsymbol{I}:(\boldsymbol{a}^0)^{-1} = (\boldsymbol{a}^0)^{-1} \\ &\boldsymbol{A}^{\mathrm{I}} = \boldsymbol{a}^I:\boldsymbol{A}^0. \end{aligned} \tag{2.23}$$

Substituting Eq. (2.23)into Eq. (2.22), the effective stiffness by Mori-Tanaka theory can be expressed with known Eshelby tensor and strain concentration tensor, as follows:

$$\begin{aligned} \boldsymbol{C}^{MT} = \sum_{I=0}^{N} f_I:\boldsymbol{c}^I:\boldsymbol{A}^I &= \left(f_0\boldsymbol{c}^0 + \sum_{I=1}^{N} f_I\boldsymbol{c}^I:\boldsymbol{a}^I\right):\boldsymbol{A}^0 \\ &= \left(f_0\boldsymbol{c}^0 + \sum_{I=1}^{N} f_I\boldsymbol{c}^I:\boldsymbol{a}^I\right):\left(f_0\boldsymbol{a}^0 + \sum_{I=1}^{N} f_I\boldsymbol{a}^I\right)^{-1} \end{aligned} \tag{2.24}$$

The ductile damage plasticity constitutive model introduced in Appendix A is integrated into the classical Mori-Tanaka model. Figure 2.6 shows the overall algorithmic procedures of the Mori-Tanaka homogenization method with ductile damage plasticity model for one-site (OS) and multi-site (MS) models.

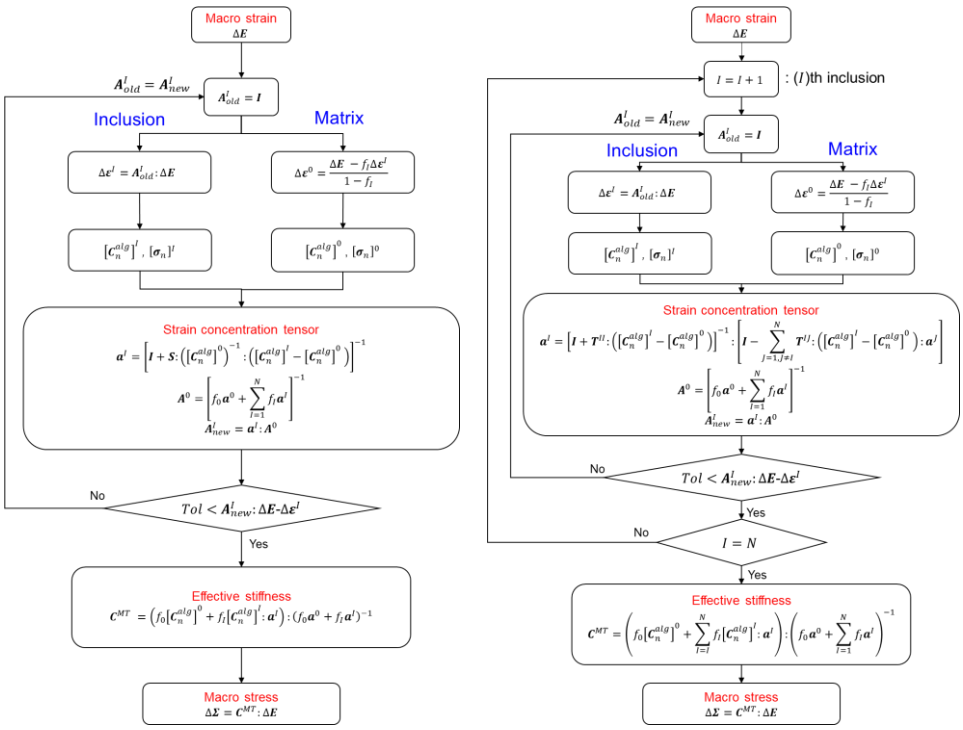

(a) One-site model ($I = 1$) (b) Multi-site model ($I = 2 \sim N$)

Figure 2.6. Flowchart of ductile damage plasticity model with Mori-Tanaka micromechanics

Depending on the global strain concentration tensor $\boldsymbol{A}^I$, the local strain increment ($\Delta \boldsymbol{\varepsilon}$) applied differently to the matrix, and inclusion phases are determined as follows:

$$\Delta \boldsymbol{\varepsilon}^I = \boldsymbol{A}^I : \Delta \boldsymbol{E}$$

$$\Delta \boldsymbol{\varepsilon}^0 = \frac{\Delta \boldsymbol{E} - f_I \Delta \boldsymbol{\varepsilon}^{\mathrm{I}}}{1 - f_I} \tag{2.25}$$

The constituents' algorithmic tangent operator ($\boldsymbol{C}_n^{\mathrm{alg}}$) and stresses ($\boldsymbol{\sigma}_n$) at n-th increment state are computed with the local strains. The flow rule judges whether constituents are under a plastic regime or not. The Newton iteration converges the

internal variables and calculates each constituent's algorithmic tangent operator and stresses for nonlinear behavior. The only tangent operators of constituents are transferred to the calculation of the local strain concentration tensor ($\boldsymbol{a}^I$). And then, it updates the global strain concentration tensor ($\boldsymbol{A}^I_{\text{new}}$). When the difference between the averaged inclusion strains ($Tol < \boldsymbol{A}^I : \Delta\boldsymbol{E} - \Delta\boldsymbol{\varepsilon}^I$) does not satisfy the criterion, the algorithm goes back to the initial step after updating the global strain concentration tensor ($\boldsymbol{A}^I_{\text{old}} = \boldsymbol{A}^I_{\text{new}}$). The micromechanics model can be divided into OS and MS models depending on the number of inclusions. While the OS model can calculate the homogenized effective stiffness at once, the MS model requires an iterative calculation for tangent operators and the strain concentration tensors for the given number of inclusion types. As a result, the incremental macro stresses of composites are calculated through homogenized effective stiffness.

2.3.3 Results and comparisons with FE homogenization

In this section, the FE-based direct numerical simulations (DNS) are performed to verify the MT model. The present MT model was verified with the DNS in two cases: without and with ductile damage of the matrix. For the reference DNS model, microscale RVE FE models with single- and multiple-inclusions were developed with ABAQUS commercial software. For verifications, two types of RVE FE models with $1 \times 1 \times 1\text{mm}$ size were developed, which have single inclusion and multiple inclusions, respectively. The inclusions are spherical. Voxel elements C3D8 (8-node linear element) with 0.02 mm size were used to minimize undesirable element

distortion and ensure the accuracy of the results. We assumed perfect bonding between the matrix and inclusions. The RVE FE models are subjected to strain loading expressed by $\Delta E = \Delta E\psi$ with $\psi = e_1 \otimes e_1 - 0.5(e_2 \otimes e_2 + e_3 \otimes e_3)$.

Periodic boundary conditions (PBC) were applied to the RVE for reasonable effective responses. The assumed properties of the inclusion and matrix are summarized in Table 2.4. The models varied the volume fraction (i.e., 0.01, 0.05, 0.1, and 0.2) to investigate its effects although only two volume fractions are presented due to limited spaces. In all simulation results, $\boldsymbol{\sigma}_e$ and $\boldsymbol{\varepsilon}_e$ from the DNS and MT models are the effective stress and strain from the volume-averaged stress and strain components. In particular, to overcome the inaccuracy of the MT model in the case of high volume fraction, the Incremental Micromechanics Scheme (IMS) and isotropization are adopted [68].

Table 2.4. Material properties of inclusion and matrix

Classification	Parameter	Value
Inclusion	Elastic Modulus, E_1 (GPa)	400
	Poisson ratio, ν_1	0.2
Matrix	Elastic Modulus, E_0 (GPa)	75
	Poisson ratio, ν_0	0.3
	Initial yield stress, σ_{y0} (MPa)	75
	Hardening parameter, k (MPa)	416
	Hardening parameter, m	0.3895

Nonlinear deformation takes place in the matrix. A material constitutive model is implemented by considering both plastic deformation and ductile damage. The ductile damage in the matrix phase is modeled by the Lemaitre-Chaboche method. Inclusion has significant stiffness properties, the only elastic stat is considered. More details about the nonlinear constitutive model and tangent stiffness of MT are referred to the Appendix A.

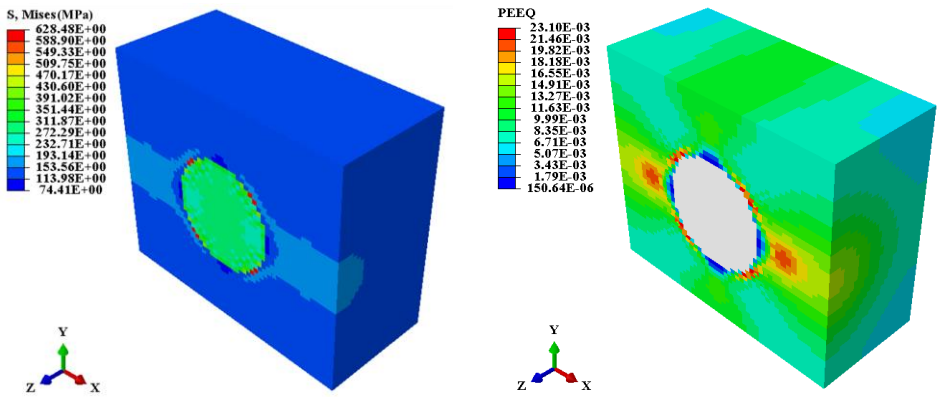

(a) Single-inclusion results

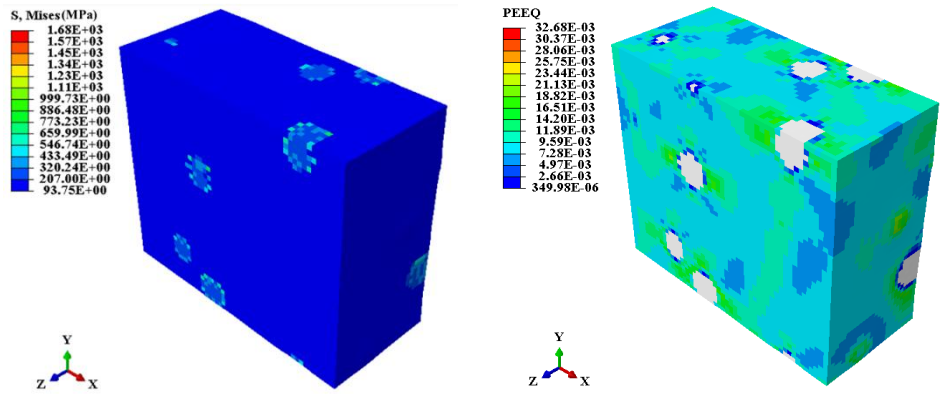

(b) Multiple-inclusion results

Figure 2.7. von Mises stress and effective plastic strain contours from (a) single-

inclusion and (b) multiple-inclusion DNS

(a)

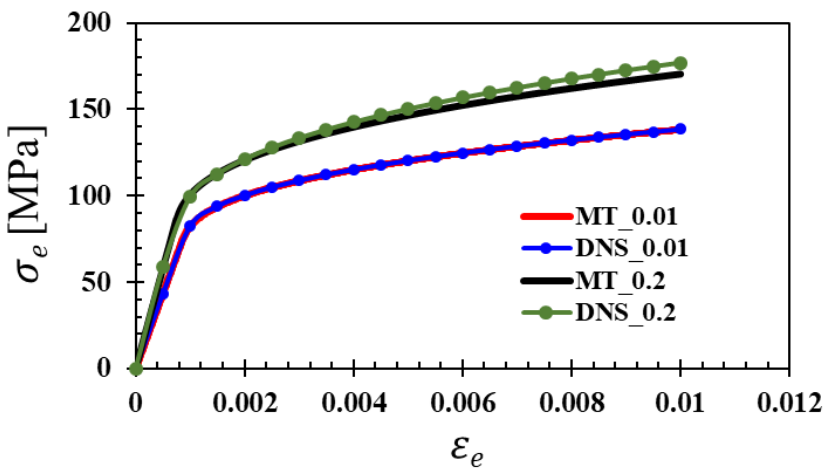

(b)

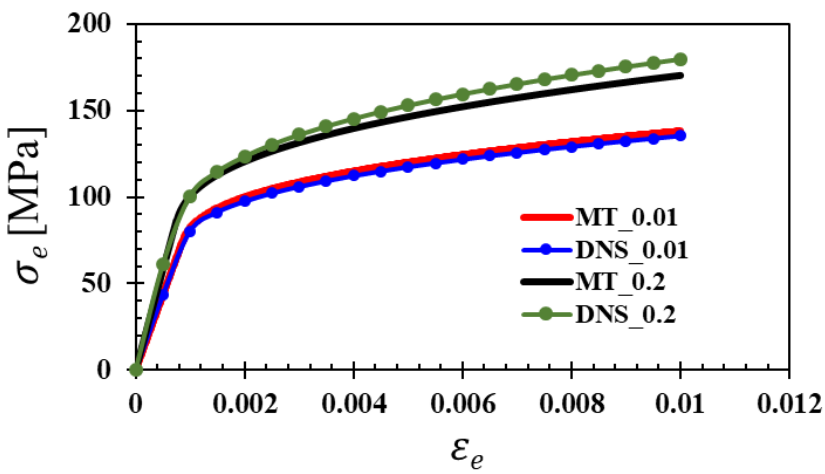

Figure 2.8. Comparisons of effective response for MT and FE-based DNS models with single inclusion and multiple inclusions of different volume fractions (0.01 and 0.2): (a) single-inclusion results, (b) multi-inclusion results

Figure 2.7 shows the von Mises stress and equivalent plastic strain on the half-sectioned plane from the single and multiple-inclusion DNS model, respectively. Stresses are concentrated along with the interface due to the mismatch of properties between inclusion and matrix. Although the MT model cannot predict such local distributions, it can well predict the effective plastic response of the composites as shown in Figure 2.8. Higher volume fraction gives rise to a higher reinforcing effect on the effective response for composites. Results from the DNS and MT models are well matched even at high volume fractions. However, in the case of $f^I = 0.2$, the FE model slightly overestimate the stress after yielding compared to the MT model. It could be postulated that the underestimation by the MT model for the high volume fraction could be attributed to the inherent nature of the non-local mean-field approaches and uniform plastic strain fields per phase.

The MT model with the ductile damage matrix was also verified with DNS results. The same single-inclusion DNS models with varying volume fractions and properties in Table 2.4 are used. Perfect interface bonding was assumed. The damage evolution model in the MT model is different from the ABAQUS built-in damage model, which is defined as follows:

$$D = \frac{1 - \exp(-\alpha\left(\frac{\bar{u}^{pl}}{\bar{u}_f^{pl}}\right))}{1 - \exp(-\alpha)} \tag{2.26}$$

where $\bar{u}^{pl}$ denotes the effective plastic displacement; $\bar{u}_f^{pl}$ is the relative plastic displacement at failure, and α is the exponent parameter. Therefore, the ABAQUS damage parameters (i.e., $\bar{u}_f^{pl}$ and α) were calibrated with the damage parameters

(i.e., S_0 and s) of the MT model through the inverse method in Section 5 referring to the p-D curve from the MT model. The material properties and calibrated damage parameters are summarized in Table 2.5. The details regarding calibration for damage parameters can be referred to the Appendix B.

Table 2.5. Pseudocode for bundle packing reconstruction algorithm

MT damage properties in matrix (reference model)		ABAQUS damage properties in matrix (ID model)	
S_0 (MPa)	s	$\bar{u}_f^{pl}$ (mm)	α
1.00×10^{-4}	0.5	3.91×10^{-4}	1.33

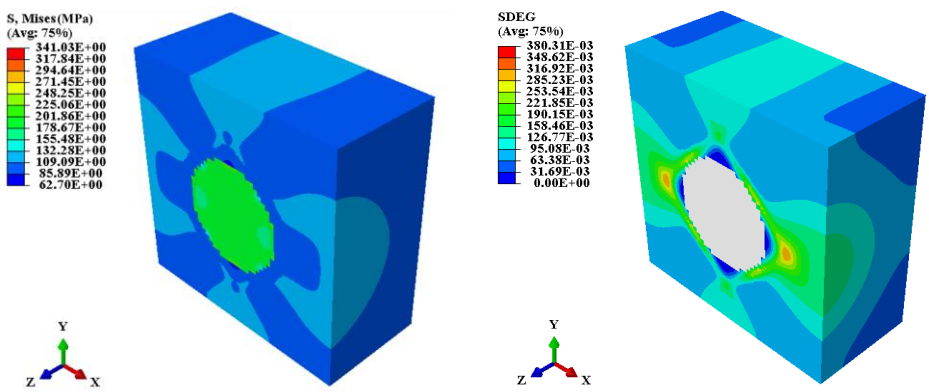

(a) von Mises stress (b) damage variable

Figure 2.9. von Mises stress and damage variable in the DNS model with $f^I = 0.05$

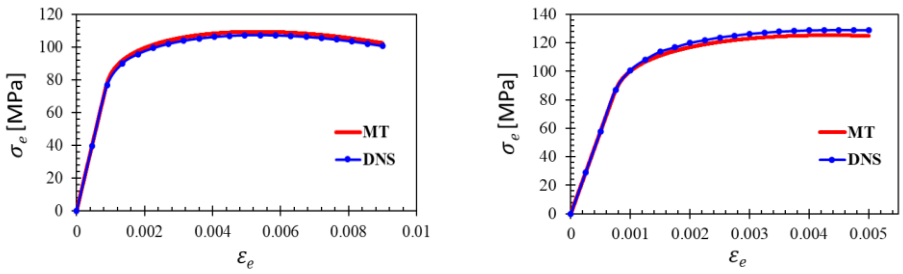

(a) $f^I = 0.01$ (b) $f^I = 0.2$

Figure 2.10. Comparison of MT effective response with DNS model

Figure 2.9 shows local distributions of von Mises and damage variables in the RVE domain. The present MT model is in good agreement with the DNS model as shown in Figure 2.10. While softening was observed in the case of volume fraction 0.01, it was not observed in the case of volume fraction 0.2. In the case of volume fraction 0.2, the DNS model slightly overestimates the yield stresses along the hardening curve.

Using both FE-based numerical homogenization and Mean-field homogenization are successfully implemented and compared to each other. These methods are based on the following SMC multiscale analysis. FE-based numerical homogenization in Chapters 3-4 and mean-field homogenization in Chapter 4 are utilized, respectively.

Chapter 3. SMC Reconstruction Modeling using Statistical Indicators

This chapter presents micro-CT image processing and a novel bundle-packing reconstruction algorithm to construct the geometry of SMC composites. This study deals with SMC composites made of T700 carbon and vinyl ester resin. The orientation and dispersion of the fibers are characterized through micro-CT image processing. A novel bundle packing reconstruction algorithm for a high-fidelity SMC model is introduced based on the manufacturing setup and image processing input parameters. Multiscale modeling is also presented to bridge mechanical properties from microscopic to meso/macroscopic behavior. Finally, the proposed multiscale modeling is validated through comparison with the experimental test and discussed based on the results thoroughly.

3.1 Manufacturing-based SMC Reconstruction Algorithm

During the compression molding process, fiber bundles in the initial charge are distributed differently depending on the mold's pressure, temperature, and speed [69, 70]. As a result, compression-molded SMC composites have a complex mesostructure in which fiber bundles are superimposed on a resin matrix at each layer. The arrangement of fiber bundles is an essential statistical characteristic of the mesostructure, which strongly influences both elastic and failure behavior. Therefore, the characterization of fiber bundles in SMC composites is required to understand the behavior of SMC composites accurately.

3.1.1 Micro-CT image processing for statistical indicators

Using micro-CT scanning and image processing, the placement of the fiber bundles is identified, and two statistical indicators in terms of orientation and dispersion are then defined with a distribution function. The samples with ∅40mm diameter and 3mm thickness are obtained at the center of the SMC plate. Micro-CT imaging is performed using Xradia 620 Versa (Carl Zeiss, USA) equipment. A series of mesostructure images are taken along through the thickness direction. The micro-CT imaging procedure is shown in Figure 3.1. MATLAB Image Processing Toolbox is employed to characterize the statistical indicators within the samples. Histogram equalization and binarization are utilized in the CT images to distinguish between the fibers and the matrix. After that, the gradient method and the local volume fraction calculation at random preset points are conducted to obtain the distributions concerning orientation and dispersion. Since the mechanical properties of SMC composites directly correlate with the arrangement of fiber bundles, the dispersion, and orientation of fiber bundles are expressed as a distribution function. These are utilized as manufacturing-dependent parameters in the SMC reconstruction algorithm [71]. The micro-CT image processing is summarized in Figure 3.2.

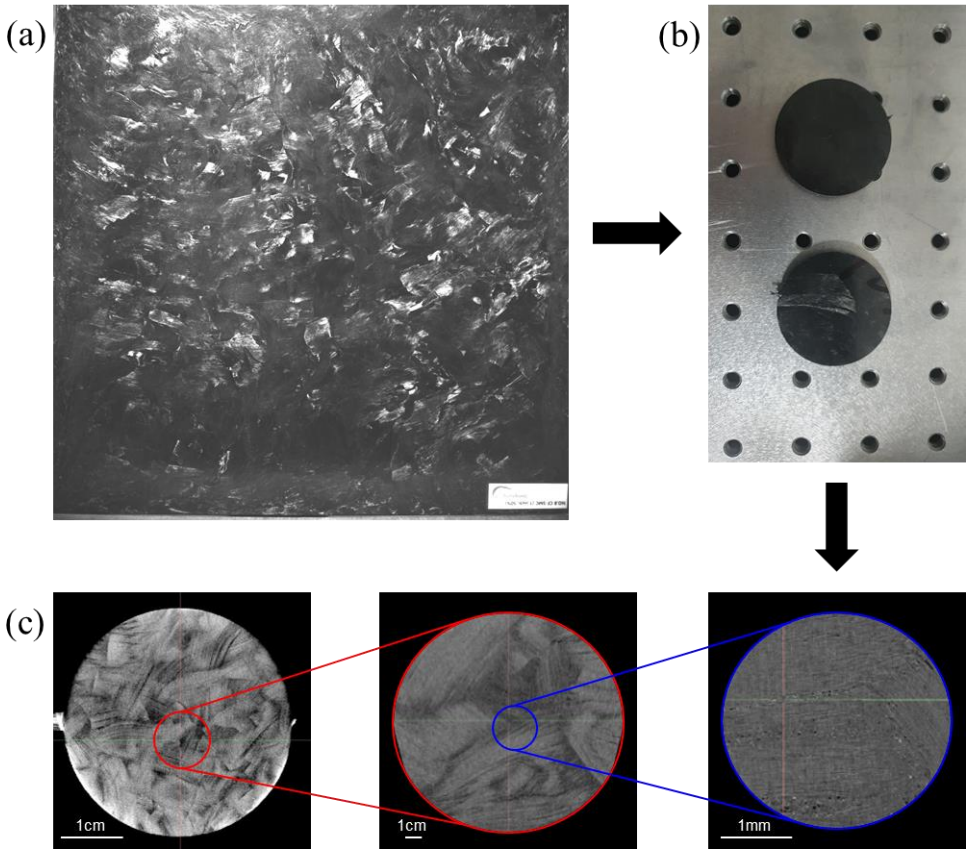

Figure 3.1. Micro-CT scanning procedure: (a) SME plate (b) Extraction of SMC samples for micro-CT scanning (c) The results of micro-CT scanning with different magnifications

In this section, the gradient method is utilized to obtain the orientation of fibers by calculating the grayscale change in the images [72]. Image processing procedures are performed using MATLAB Image Processing Toolbox and consist of three steps. First, the histogram equalization is conducted to distinguish the fiber from the matrix in the micro-CT image. Through this pre-processing step, the accuracy of the gradient method is improved. After that, the gradient method is applied to the pre-

processed micro-CT image. In this step, a MATLAB built-in function 'imgradient' is used. Grayscale values of 3 by 3 pixels around the particular pixel are called from the micro-CT image to calculate the magnitude and normal vector at a specific pixel. Then, the image gradient (∇I) and the gradient orientation are computed based on the change of grayscale values (∂I) of x and y-axis for each pixel (∂x, ∂y). M and G represent the magnitude and orientation of the image gradient calculated by Eq. (3.1). Through this operation, the magnitude and normal vector value of each pixel are computed. Detail procedure of the gradient method is depicted in Figure 3.2.

$$\nabla I = [\partial I/\partial x \quad \partial I/\partial y]^{\mathrm{T}}$$

$$M = \sqrt{(\partial I/\partial x)^2 + (\partial I/\partial y)^2}, \quad G = tan^{-1}(\frac{\partial I/\partial y}{\partial I/\partial x}) \tag{3.1}$$

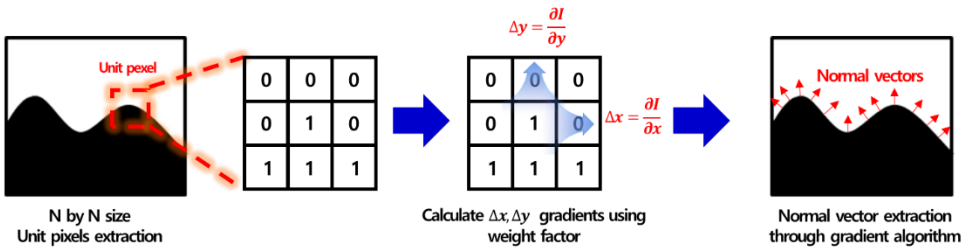

Figure 3.2. Procedure for calculating the normal vector using the gradient method

Finally, the orientation vector is calculated through the normal vector value by the gradient method. Overall image processing procedures to obtain fiber orientation are shown in Figure 3.3.

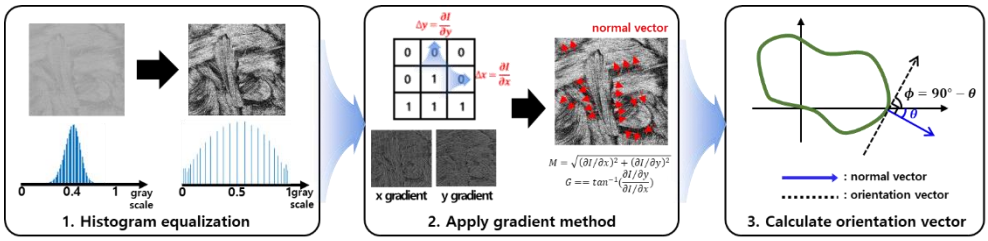

Figure 3.3. Overall image processing procedures: Calculation of the fiber orientation

The fiber local volume fraction is defined to evaluate the non-uniform distribution of the fibers in the SMC plate. First, the histogram equalization is performed as in the gradient method. Next, an image binarization is performed to differentiate between fiber and matrix. The grayscale value of the fiber and matrix was set to one and zero, respectively. To obtain statistical distribution data of the fiber local volume fraction, one thousand local sampling points and areas are randomly generated for each 2D micro-CT image. After that, the local fiber volume fraction in each sampling area is calculated to generate the distribution. In this case, the sampling area was set as a square with a side length of 200 pixels. The image processing procedure for calculating the local fiber volume fraction is summarized in Figure 3.4.

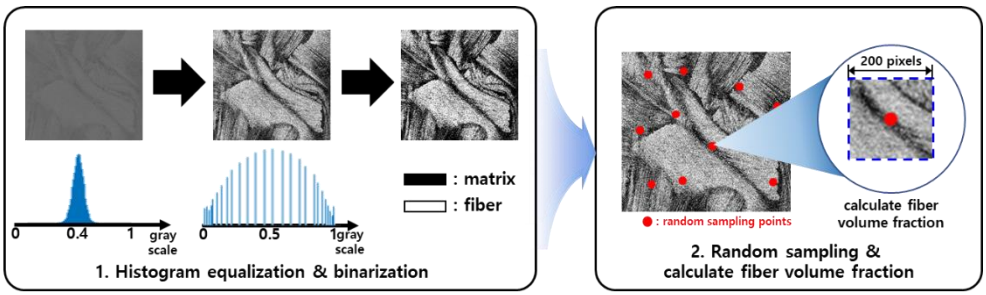

Figure 3.4. Computation procedure of the local volume fraction at randomly preset sample points

The results of orientation and local volume fraction distribution are summarized in Figure 3.5. Figure 3.5(a) is the orientation distribution in the probability density function (PDF). It has uniform probabilities at every angle, indicating that the SMC composites have randomly oriented bundles. Figure 3.5(b) exhibits the local volume fraction distribution. It has a shape of Gaussian distribution with COV=0.133. The fiber volume fraction from the micro-CT image processing is 55%, set as input quantity. The distributions of the orientation and local volume fraction are directly utilized in the reconstruction algorithm to generate high-fidelity SMC models.

The effect of the initial charge's size was investigated in the work of Evans [73]. But, the size of the initial charge used in this study was $200\text{mm} \times 200\text{mm}$ for making the $300\text{mm} \times 300\text{mm}$ size SMC plate. The large size of the initial charge is designed to minimize the variation in the properties of the molded plate. Therefore, sampling from the middle of the SMC plate can represent the SMC plate, and since the sample contains several fiber bundles in the thickness direction, a sufficient amount of information can be obtained.

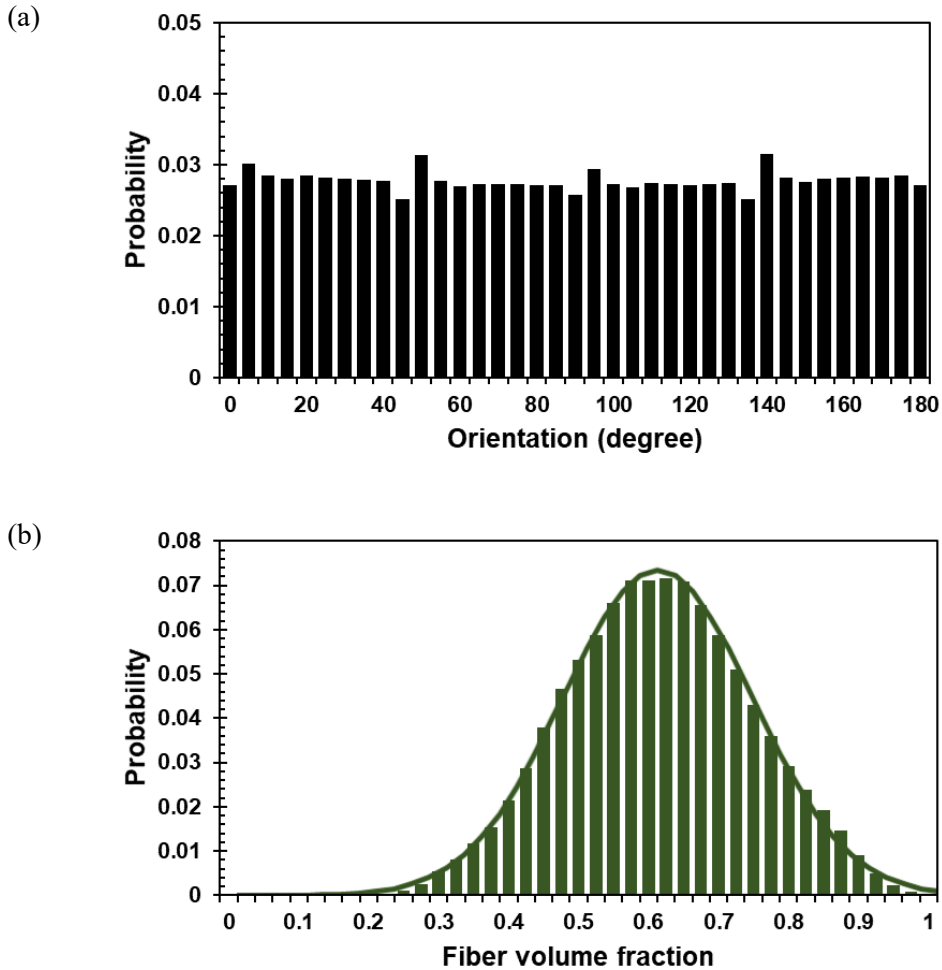

Figure 3.5. Statistical distributions from micro-CT image processing: (a) Orientation (b) local volume fraction

3.1.2 Bundle packing reconstruction algorithm

A novel reconstruction algorithm through bundle packing is developed to generate high-fidelity SMC mesostructure models in a voxelated square space. For the reconstruction algorithm, manufacturing-dependent parameters are selected as

inputs. It includes the sizes of the bundles and the plates, the bundle volume fraction, and the targeted statistical distributions of the bundles' orientation and local volume fraction. Among the input parameters, the targeted statistical distributions of bundles' orientation and local volume fraction in cumulative distribution function (CDF) are from micro-CT images. Statistical distribution of the bundle local volume fraction within a preset domain is determined from the prescribed random sample points. The sample points are prescribed randomly at the beginning of the algorithm. These locations of sample points do not change during the reconstruction algorithm. Thus, the distribution of the local volume fraction changes depending on the location of bundle packing. The input parameters are summarized in Table 3.1 by classifying them into two.

Table 3.1. List of the input parameters for the proposed SMC reconstruction algorithm

Classification		Symbol
Initial charge	Plate size	L_{plate}
	Number of layers in the plate	n_{layer}
	Length of the bundle	L_{bundle}
	Width of the bundle	W_{bundle}
	The volume fraction of the bundles	V_{bundle}
Compression molding	Orientation of bundles	$F_{ori}(x)$
	The local volume fraction of bundles	$F_{local}(x)$

Before bundle packing, pre-processing is performed to build a repository of bundles based on the targeted orientation statistical distribution, as shown in Figure 3.6. The number of bundles is computed in terms of SMC plate size, bundle sizes, and the volume fraction of the bundles. In Eq. (3.2), NB_{layer} and NB_{plate} denote the number of bundles in a layer and plate, respectively.

$$NB_{layer} = \left\lceil \frac{L_{plate}^2 V_{bundle}}{W_{bundle} L_{bundle}} \right\rceil$$
$$NB_{plate} = NB_{layer} \cdot n_{layer} \tag{3.2}$$

Given the manufacturing-dependent parameters, the rectangular-shaped bundles are packed into the 3D voxelated square space one by one for a single layer using the modified random sequential adsorption (RSA) algorithm [30]. It dynamically moves the bundle segment to the upper and lower layers to maximize space utilization. After that, 3D SMC modeling is constructed by piling up bundle-packed layers.

This algorithm obeys two conditions. The first condition is to check the location feasibility of the bundles during the bundle packing process. The algorithm finds feasible packing locations during the bundle packing process, allowing one overlap between bundles at most. If more amount of overlap is allowed in the modeling, the shape of SMC composites could be distorted due to a bias in the bundles' location. The second condition calculates the local volume fraction at the preset points during the bundle packing process. The preset points are defined randomly in each layer. It is repeatedly checked if it is within the tolerance range by comparing it to the targeted statistical distribution. Otherwise, a candidate of the bundle location would be altered

and newly checked the conditions from the first condition. If these two conditions are satisfied, the bundle packing is conducted on the layer using a repository of fiber bundles created to follow the targeted orientation distribution. During the bundle packing, a rise and sink process is applied to represent the undulation by raising the overlapping parts to the upper layer. On the other hand, the overhanging parts of the bundle sink into the current layer. It is noted that this process creates the bent geometries of the bundles. As a result, the proposed bundle packing reconstruction algorithm reflects physical features accurately. Finally, a computational procedure for the bundle packing reconstruction algorithm is summarized as Pseudocodes in Table 3.2. The overall flow chart is also depicted in Figure 3.6.

Table 3.2. Pseudocode for bundle packing reconstruction algorithm

Numerical implementation

Input: L_{plate}, L_{bundle}, n_{layer}, $F_{local}(x)$, $F_{ori}(x)$, V_{bundle}, W_{bundle}
Output: 3D reconstructed model, the local orientations of bundles

```
1  for i=1: n_layer
2      Initialize internal variables and start to pack fiber bundles on the (i)-th
       layer
3      Define random sample points for the local volume fraction
4      while |V_bundle^target − V_bundle^(i)| ≤ tol
5          Build fiber bundle repository using Eq. (3.2) and F_ori(x).
6          for j=1: NB_layer
7              Define the bundle location: (x_bundle, y_bundle)
8              if location feasible
9                  overlapped parts: pack on the (i+1)-th layer
10                 overhanging parts: pack on the (i)-th layer
11             else not feasible
12                 go to line 7
13             end if
14             Calculate the local volume fraction distribution of (i)-th layer:
               F_local^(i)(x)
15             if |F_local^(i) − F_local| ≤ tol
16                 continue the packing
17             else
18                 cancel the packing and go to line 7
19             end if
20         end for
21         Calculate the volume fraction on the (i)-th plate: V_bundle^(i)
22     end while
23     Check the orientation distribution with the target
24 end for
25 Stacking up the reconstructed layers
```

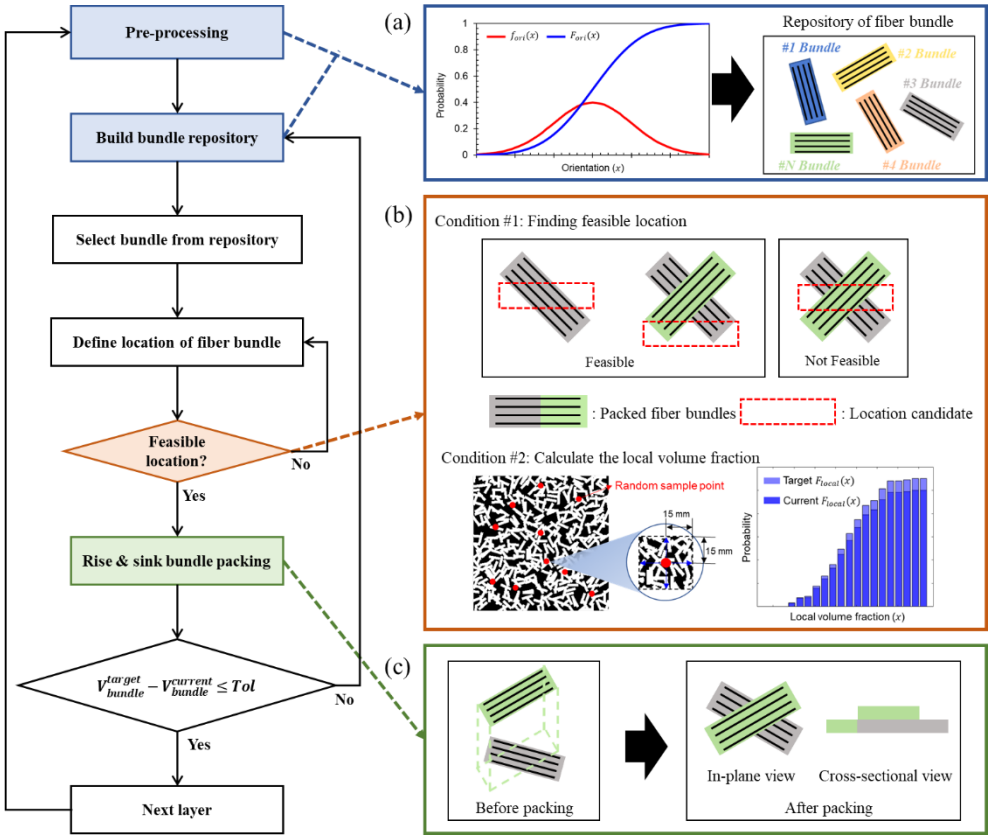

Figure 3.6. Flowchart of the reconstruction algorithm: (a) Building a repository of fiber bundles (b) Two conditions for finding a feasible location (c) rise-sink bundle packing methodology.

The proposed reconstruction algorithm generates more realistic high-fidelity SMC models based on the direct statistical distributions of the orientation and local volume fraction. It holds apparent advantages over the existing SMC modeling which matches only the orientation of the bundle with an averaged orientation tensor. The reconstructed single layer is generated based on the manufacturing-dependent parameters in Table 3.3, as summarized in Figure 3.7.

Table 3.3. The input parameters for the SMC reconstruction algorithm

Description	Value
Plate size	$300 \times 300\text{mm}^2$
Bundle size	$25 \times 5\text{mm}^2$
The volume fraction of the bundle	60%

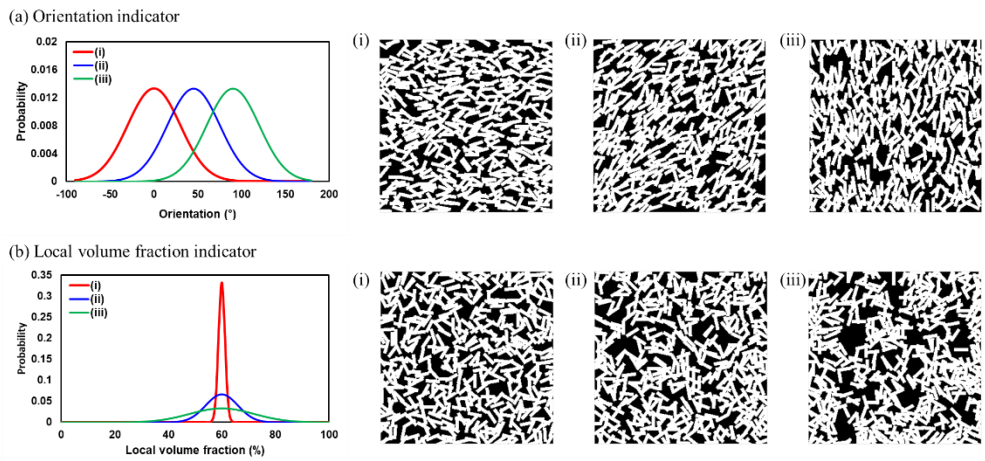

Figure 3.7. Reconstructed single layer with different statistical distributions: (a) Orientation (b) Local volume fraction (dispersion)

The single individual layer of SMC composites shows different morphology depending on the statistical indicators represented as a Gaussian distribution. The models in Figure 3.7(a) exhibit distinct orientations of fiber bundles depending on the targeted distribution while holding the uniform dispersion. In Figure 3.7(b), voids in the SMC layer are formed from an imbalanced arrangement of fiber bundles. This

occurrence realizes the resin-rich area that occurs in the compression molding process. It crucially happens with clumped dispersion of fiber bundles.

By changing the statistical parameters of the proposed reconstruction algorithm, multiple layers of the SMC composites are generated. The high-fidelity SMC model is composed in the 3D voxelated cuboid space by stacking up the reconstructed layers. The voxels in the reconstruction model are converted into a solid element for FE simulation. Moreover, since each bundle is aligned at a specified angle, the elements corresponding to the bundle have a local orientation. In this study, nodes and connectivity of a C3D8 element are created according to Abaqus/Standard input format. All the process for FE modeling is depicted in Figure 3.8.

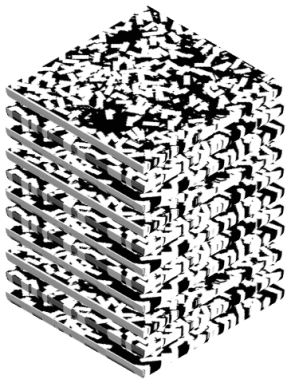

(a)

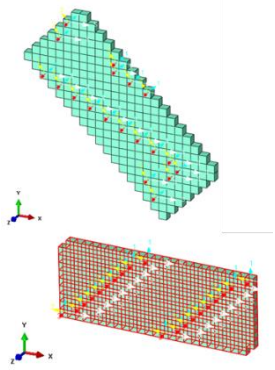

(b)

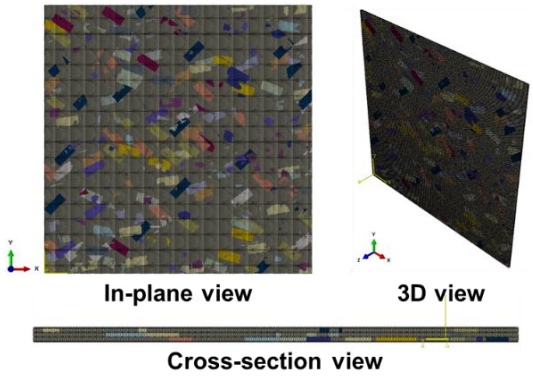

(c)

Figure 3.8. FE modeling from reconstruction model: (a) Stack of SMC reconstructed models (b) C3D8 FE models with different views (c) Defining the local orientation for fiber bundles

3.2 Experimental Setup

3.2.1 Tensile testing

An experimental tensile test is performed to obtain the mechanical properties of SMC composites. An initial charge of $200\text{mm} \times 200\text{mm}$ size is subjected to a

compression molding process to fabricate the SMC composite plate with a size of $300\text{mm} \times 300\text{mm} \times 3\text{ mm}$. The fiber bundles in the SMC plate have a quasi-isotropic orientation as observed in the micro-CT image processing. Tensile specimens are extracted from the molded plate with a 35mm width following the ASTM D3039. Considering the size of the fiber bundle, the specimen is designed to have a large enough width. Dimensions of the tensile specimen are depicted in Figure 3.9. Sandpapers are attached to 40mm long grip regions at both ends of the specimens to prevent slipping during the testing. Therefore, the gage length of the tensile specimen becomes 170mm. From trimming the boundary of specimens, five specimen samples are prepared. The displacement-controlled uniaxial tensile test is performed with a 30 kN MTS material test machine with a 2mm/min crosshead rate. The tensile specimens' photographs before and after testing are shown in Figure 3.10. After failure, as shown in Figure 3.10(b), it is observed that the matrix failure is dominant in the SMC specimen because the fiber bundles have their geometry even after specimen breakage. This failure pattern was also reported in the SMC composites study [74].

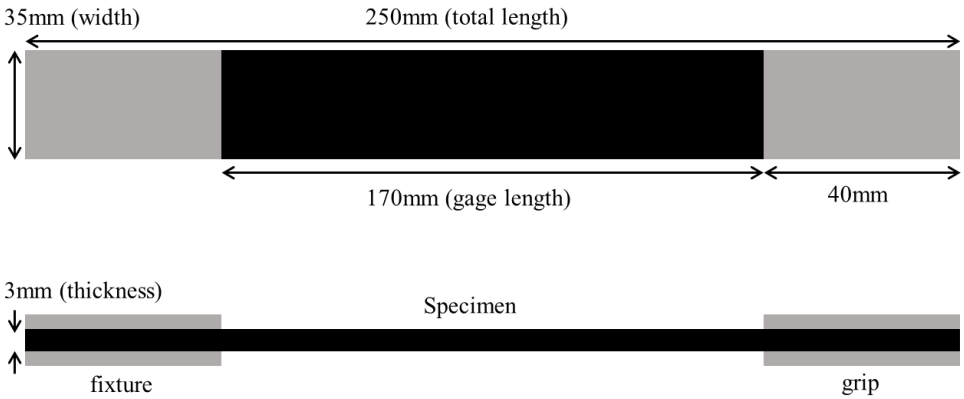

Figure 3.9. Dimensions of ASTM3039.

Figure 3.10. Experimental tensile specimens: (a) before testing (b) after testing

The experimental tensile tests are conducted by Seoul National University (SNU) and Hyundai Motors Group, with different strain measurement methods. In SNU, the strain is measured by dividing the crosshead displacement by the gage length of the tensile specimen. On the other hand, the average strain on the specimen surface using digital image correlation (DIC) equipment in the Hyundai is measured. It is noted that the different strains are estimated depending on the strain measurement

techniques [75]. Generally, the crosshead strain is significantly greater than the DIC measurement. As a result, the crosshead-based modulus underestimates compared with the DIC-based measurement. The stress-strain curves are plotted in Figure 3.11. Notably, because of the heterogeneity of the SMC composites, the difference in results between the two measurement techniques becomes more salient. Both stress-strain curves show linear behavior. The nominal stress is computed by dividing the force by the cross-sectional area of the tensile specimen. The elastic modulus is calculated by the curve's initial slope and measured in the 0.05 to 0.25% strain range. Likewise, the strength is measured based on the ultimate maximum strength, which is the maximum stress of the stress-strain curve.

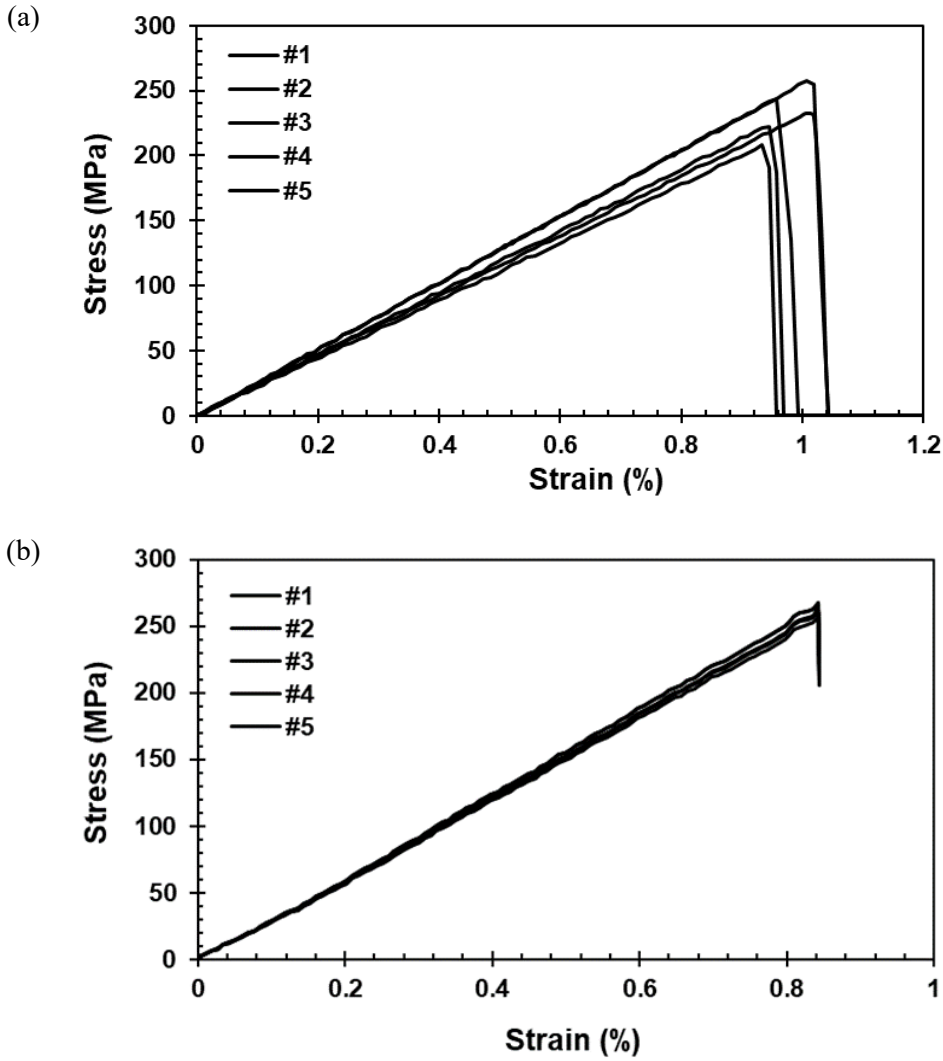

Figure 3.11. Stress-Strain curves from experiments: (a) Crosshead-based strain (b) DIC-based strain

Figure 3.12 shows the stress-strain curves of pure vinyl ester resin from the tensile test. The vinyl ester resin is utilized as the matrix in the SMC composites. The properties are employed in the simulation.

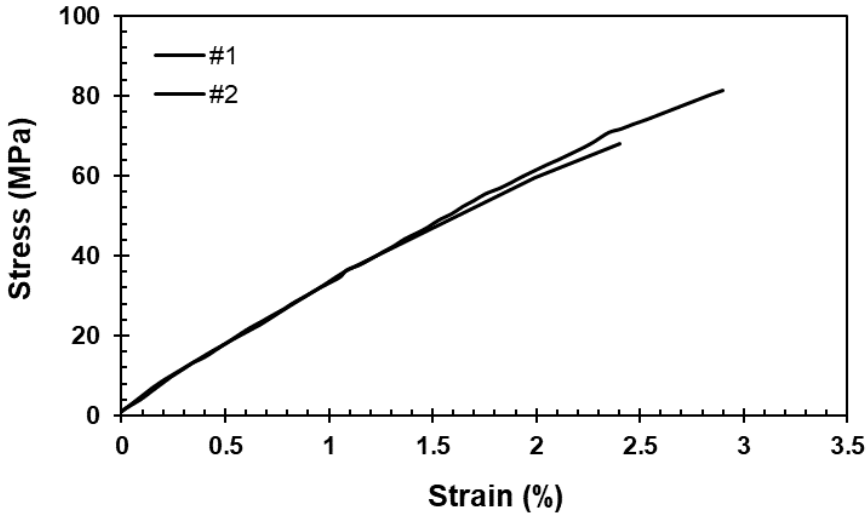

Figure 3.12. Stress-strain curve of pure vinyl ester resin from the tensile experimental test

3.2.2 Tensile specimen modeling and measurement

Uniaxial tensile simulations are conducted with the reconstructed SMC models. The SMC plate and fiber bundle size are designed to have $300\text{mm} \times 300\text{mm} \times 3\text{mm}$ and $50.8\text{mm} \times 20\text{mm}$, respectively. The fiber volume fraction in the SMC plate is 55%, as revealed by micro-CT image processing. Therefore, the fiber bundle is assumed to comprise 78% fiber, and a unit layer is assumed to have a 70% fiber bundle volume fraction to match 55% fiber volume fraction by 70%×78%=55%.

The microstructure of the fiber bundle is shown in Figure 3.13. The computational homogenization technique is required to obtain the effective properties of the fiber bundle. The microscale RVE with unidirectional fibers is shown in Figure 3.13. The constituents are T700 carbon fiber and vinyl ester resin. The mechanical properties

of the constituents are from literature and experimental tests. FE-based DNS is conducted for the effective properties of the fiber bundle. The mechanical properties are summarized in Table 3.4.

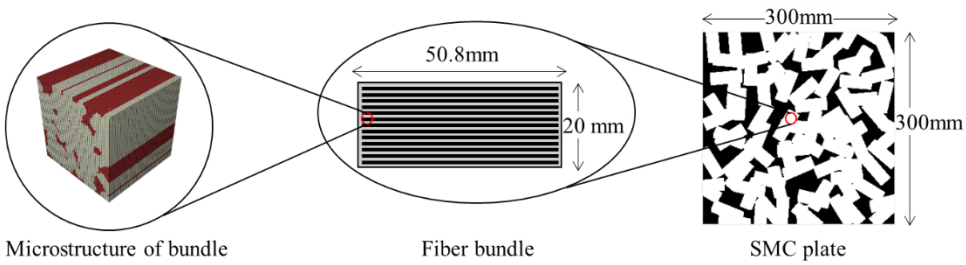

Figure 3.13. Multiscale modeling of the SMC composites

Table 3.4. Elastic mechanical properties of SMC composites

	T700	Vinyl ester	Fiber bundle
E_1 (MPa)	240000	3480	203292
E_2 (MPa)	14700		11639
G_{12} (MPa)	6400		5027
G_{23} (MPa)	5400		4206
ν_{12}	0.3	0.3	0.01737
ν_{23}	0.35		0.349

The reconstruction algorithm uses the statistical distributions from micro-CT image processing to generate an SMC model with a 70% bundle volume fraction. As a result, a series of reconstructed layers are obtained, as shown in Figure 3.14(a). After that,

Figure 3.14(b) shows that tensile specimens are extracted from the reconstructed SMC models. A total of 15 tensile specimens are prepared from the five reconstructed SMC models. A coupling constraint is applied to elements at both ends of the specimen with reference points for the tensile simulation. After that, boundary and loading conditions are applied to the reference points that correspond with the parts of the grip and fixture in the tensile testing system, as shown in Figure 3.14(c).

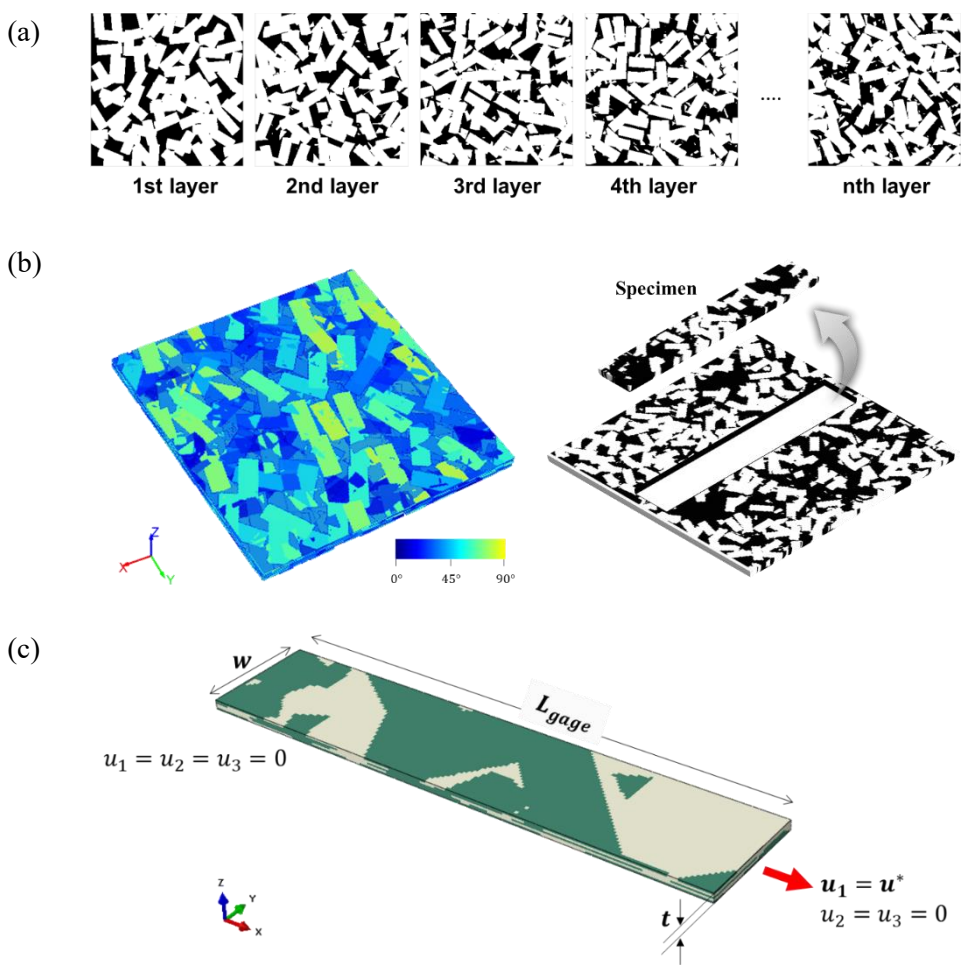

Figure 3.14. High-fidelity SMC modeling: (a) Reconstructed models for each layer

(b) orientation contour and specimen extraction (c) boundary condition for tensile test

For strain measurement in the tensile simulation, two different methods are performed. The first is to measure the strain based on the crosshead displacement. Like the experiment, the strain from the simulation is obtained by dividing displacement by the gage length. The calculations of uniaxial strain and stress are expressed in Eq. (3.3).

$$\varepsilon_1 = \frac{u^*}{L_{gage}}, \qquad \sigma_1 = \frac{RF_1}{wt} \tag{3.3}$$

The second strain measurement method is by the digital image correlation (DIC) equipment. The effective strain is calculated by applying the volume-averaging scheme in terms of strain fields after tensile simulation. Although DIC is measured only on the surface of the specimen, the volume-averaging in simulations can be performed over the entire specimen domain. The equation can be expressed as Eq. (3.4).

$$\varepsilon_1 = \frac{\int_\Omega \hat{\varepsilon}_1 d\Omega}{\int_\Omega d\Omega}, \qquad \sigma_1 = \frac{RF_1}{wt} \tag{3.4}$$

Herein, Ω is the total element domain of the specimen. This domain does not include the jig parts, which is also not ROI in the DIC measurement. $\hat{\varepsilon}_1$ is the uniaxial strain value at Gaussian points. With different types of strain measurement, the comparison of tensile modulus can be achieved with experimental results.

3.3 Results and Discussion

Static finite element analysis is performed on the reconstructed SMC models subjected to tensile loading. Based on the strain measurements described above, the modulus of the SMC composites is calculated from the initial slope of the stress-strain curve. Figure 3.15 shows the modulus change according to the number of layers constituting the ASTM 3039 specimen with 3 mm thickness. An increment of the SMC modulus is observed in thinner layers in both strain measurement methods, as shown in Table 3.5. It is because of the increasing heterogeneity of the SMC mesostructure through the thickness. The deformation in the z-direction due to the different properties of constituents occurs significantly during the tensile simulation. Thus, increasing the number of layers improves the stress transfer between layers in the z-direction and makes the SMC specimen stiffer. These investigations have also been handled in the literature to ensure the mechanical performance of SMC composites [35, 76, 77]. In addition, as the number of layers increases, the quasi-isotropy seems to increase, which means increasing the uniformity in the local volume fraction and orientation leads to reduced sample-to-sample variability in effective properties. Despite the same statistical parameters, different-shaped mesostructures are obtained. Therefore, simulations make such variability denoted by a standard error in the graph.

Table 3.5. Mean and COV of elastic modulus with different numbers of layers

(unit: GPa)

Layers	Mean		COV	
	Crosshead	DIC	Crosshead	DIC
5	20.2	31.6	0.26	0.37
7	21.2	34.5	0.22	0.25
10	30.5	48.5	0.16	0.17
13	33.3	54.7	0.14	0.14
15	35.6	57.3	0.12	0.13

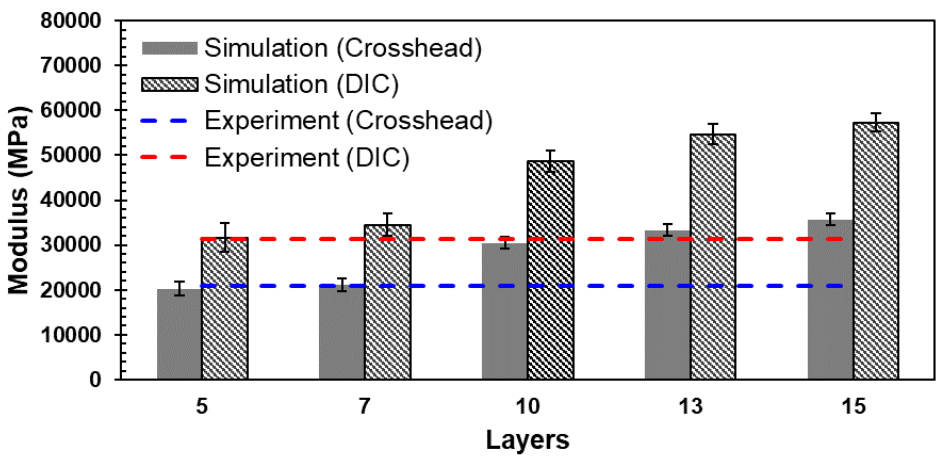

Figure 3.15. Effect of the number of layers on the tensile modulus

In comparison with the experiments, both crosshead and DIC measurements seem to fit well with experimental tests in the case of 5~7 layers. Since carbon fiber tows have $200\sim300\ \mathrm{g/m^2}$ fiber areal weight (FAW), they are assumed to have a

0.2mm~0.3mm thickness. From the bundle thickness, the ideal lamination in the fiber bundles could be 10~15 layers for 3 mm specimen thickness when the resin is excluded. However, the number of layers becomes 5.5~8.25 when applied 55% fiber volume fraction to the number of the ideal lamination. Therefore, it is validated that the prediction with tensile simulation has a good agreement with experimental results. Next, a method is introduced for predicting tensile strength through the FE static simulation. The tensile strength of SMC composites is mainly dependent on the matrix based on the existing reports and inspection of failure patterns in Figure 3.10. Therefore, this study proposes that the strength of the SMC composite is predicted based on the matrix strength. In the previous section, the vinyl ester resin has a strength of 65~80MPa from tensile tests. An assumption is made that failure of SMC composites yields when the volume-averaged stress of the matrix region in the simulation models reaches the pure vinyl ester's strength from the experimental test. The volume-averaged stress of the matrix region is computed as follows.

$$\sigma_{Matrix} = \frac{\int_{\Omega_{Matrix}} \hat{\sigma}_1 d\Omega_{Matrix}}{\int_{\Omega_{Matrix}} d\Omega_{Matrix}} \tag{3.5}$$

The volume-averaged stress in the matrix region is calculated when the uniaxial stress level of the specimen calculated in Eq. (3.3) reaches 260MPa, the tensile strength from the experimental tests. Figure 3.16 shows the volume-averaged stress of the matrix for the different number of layers at the moment of reaching the experimental strength (260MPa). It is noted that decreasing the matrix volume-averaged stress with the increasing number of layers implies decreasing load-carrying by the matrix and increasing load-carrying by the fiber bundles. The higher

modulus of the SMC specimen with the increasing number of layers, as shown in Figure 3.15, seems to be attributed to this mechanism. The red band in Figure 3.16 represents the range of pure resin strength from the experimental test. The matrix volume-averaged stress from the simulation matches well with the experimental strength in the case of 5~7 layers. This match sufficiently supports the proposed strength evaluation method using the high-fidelity SMC composite models. In Figure 3.17, the heterogeneous strain distribution can be identified in the simulation, which is also observed in the experiment. It shows the influence of the spatially varying distribution of fiber bundles. In conclusion, it is demonstrated that the proposed SMC reconstruction algorithm can directly reflect the mesostructure of the actual SMC composites, and also, the proposed strength and stiffness evaluation method can accurately predict the mechanical properties of actual SMC composites.

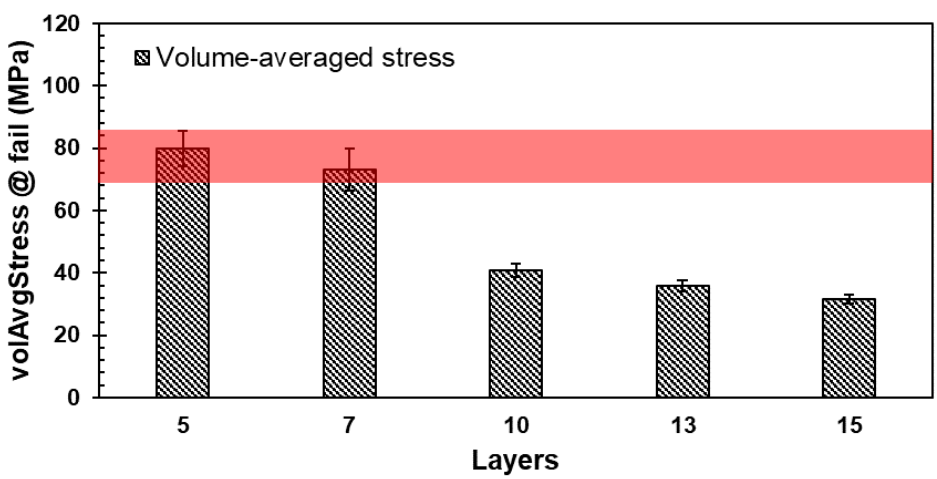

Figure 3.16. Volume average stress in the matrix region for the number of layers

(red band: strength from the experiment)

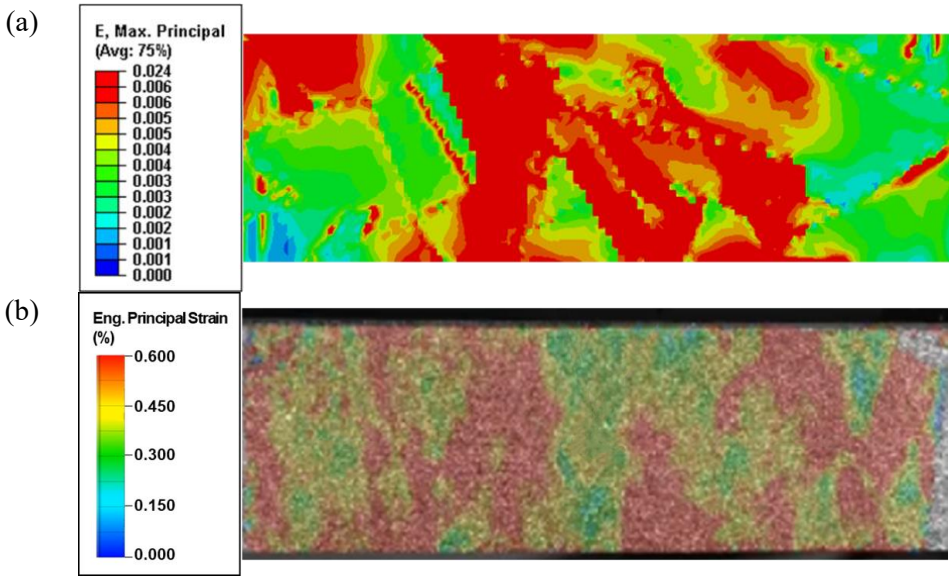

Figure 3.17. Engineering principal strain contours: (a) SMC simulation (b) DIC measurement

Chapter 4. Damage Characterization for SMC Composites

4.1 Study Background

Composite materials have a variety of failure modes, making it more difficult to predict strength than linear behavior. The strength is inherently dependent on the fiber's orientation. In the case of CFRP laminate composites, for example, the longitudinal strength is greater than the transverse strength, and the tensile strength and compressive strength are different. Due to the concentration of stresses and strains in the matrix around the fibers, transverse tensile strength exhibits the lowest value. In early research, multiaxial strength criteria were used to determine the failure of composites. The purpose of this approach is to enable designers to quickly predict when failures will occur under complex loading conditions. Microscopic failure modes such as fiber pullout, fiber breakage, buckling, matrix cracking, and delamination are not considered in this semi-empirical study. The failure modes of real-world composites are complex, occurring in various combinations and sequences. A wide range of multiaxial composite failure criteria has been reported from the world-wide failure exercise (WWFE) [78]. The WWFE was a global movement in which nineteen leading developers of composite failure theory were asked to use their theories to predict failure in sufficient test environments. These failure theories are phenomenological and originate in an attempt to express experimental observations. These models are preferred since it allows a systematic approach to design and reduces the number of experiments.

Many failure criteria for anisotropic composites are based on the plasticity theory for isotropic metallic materials. Accordingly, by drawing the failure point in the stress domain of the material, a failure envelope can be obtained as with plasticity theory. In general, the coordinate axes of the stress space correspond to the principal material axes. According to this idea, stress combinations inside the surface do not lead to failure, whereas stresses outside the surface cause failure. The maximum stress criterion was first introduced to the composite failure model [79]. However, this model does not account for possible interactions between the stress components, which means that when a particular stress component exceeds its limit value, failure occurs independently of all other stress components. It shows a good agreement in uniaxial stress but has a large difference in multiaxial stress cases. This analysis indicates that the prediction of the maximum stress criterion agrees reasonably well with the experiment when it is close to 0° or 90° relative to the composite fiber direction, but does not fit well at other angles. In a similar way, Waddoups extended the maximum normal strain theory (or Saint Venant's theory) for anisotropic materials and proposed a maximum strain criterion for composite materials [80]. This criterion predicts failure when the principal material axial strain component exceeds an ultimate strength. In the case of an isotropic material, the ultimate values in stress and the strain criterion based on the main axes are the same. On the other hand, in the case of anisotropic composite materials, they show different values. Simulating complex failure mechanisms is also limited by a simple mathematical expression, which is why predicted values from a model cannot be experimentally verified.

Similarly, the quadratic interaction criteria were developed from the initial failure theory for isotropic materials, but they differ from the maximum stress and strain criterion in that they can explain the interaction between stresses. The von Mises criterion is a quadratic interaction that is widely used to determine the yield point for isotropic metals. Furthermore, Hill modified the von Mises criterion for anisotropic materials [81]. It allows the Tsai-Hill equation to express the failure criteria of materials with different tensile and compressive strengths as quadratic functions [82]. The model shows a good result with asymmetric materials, such as thermoplastics [83]. Due to the plasticity theory, only shear stress and strain have an influence on these models. However, it has been demonstrated that hydrostatic pressure causes shear deformation and failure in composite materials [84]. Taking hydrostatic pressure into account, Tsai and Wu presented a failure model for composite materials [85]. Furthermore, Hasin suggested that each composite failure mode should be individually considered using the quadratic interaction [86]. Despite the challenge of defining the strength of each component, the model shows excellent agreement in predicting the strength of fiber-reinforced composites.

In this chapter, failure analysis of SMC composite materials is presented by focusing on the failure model of SMC constituents. The direction and distribution of fiber bundles in SMC composite material greatly influence failure behavior as well as linear behavior. Material constitutive models are implemented to simulate the failure behavior in the fiber bundle, matrix, and interfaces. The proposed model allows for predicting the effects of the fiber bundles' orientation and dispersion on the modulus and strength. Finally, the simulation results are compared with the

experimental tensile test. In this validation, the degree of scattering is also exploited. Failure mechanisms are then observed through SEM scanning to verify the local damage from simulation models.

4.2 Material Constitutive Modeling for Failure Analysis

Based on the four major failure modes of SMC composites, material constitutive models of each constituent are discussed and constructed. After that, depending on the statistical indicators, a tendency of composites' behavior is demonstrated. In the failure behavior of the SMC composites, there are four major failure modes: matrix crack, bundle splitting/breakage, and interface failure between two bundles or the bundle and matrix [34]. This observation indicates that tensile failure is initiated by matrix failure or interface failure, possibly caused by stress concentration due to the mesostructure heterogeneity of the SMC composites. The propagation of the initial cracks induces bundle splitting and carbon fiber breakage. Therefore, it is necessary to consider these mechanisms within the proposed FE modeling. Three constitutive models are introduced as follows. The fiber bundle constitutive material model is established using the Hahsin progressive failure criterion [87]. For the matrix region, the damage plasticity model is introduced by combining J_2 plasticity and Lemaitre-Chaboche ductile damage models [88]. The interface between the matrix and bundle is modeled using a cohesive element with a traction-separation law [89].

4.2.1 Progressive failure model for fiber bundles

Failure criteria are generally used for finding out the onset of damage initiation at a material point. Once damage initiation occurs, softening behavior proceeds at corresponding material points In this work, a three-dimensional failure criterion is formulated by Hashin's theory and integrated with the continuum damage model (CDM) for progressive damage behavior. The Hashin's failure criteria equations incorporate the effect for both tension and compression states of matrix and fiber as follows:

Fiber tension failure ($\sigma_{11} > 0$)

$$e_{ft} = \left(\frac{\sigma_{11}}{F_{1t}}\right)^2 + \alpha\left(\frac{\sigma_{12} + \sigma_{13}}{F_{ls}}\right)^2 \geq 1$$

Fiber compression failure ($\sigma_{11} < 0$)

$$e_{fc} = \left(\frac{\sigma_{11}}{F_{1c}}\right)^2 \geq 1$$

Matrix tension failure ($\sigma_{22} > 0$)

$$e_{mt} = \left(\frac{\sigma_{22}}{F_{2t}}\right)^2 + \left(\frac{\sigma_{12}}{F_{ls}}\right)^2 + \left(\frac{\sigma_{23}}{F_{ts}}\right)^2 \geq 1 \tag{4.1}$$

Matrix compression failure ($\sigma_{22} < 0$)

$$e_{mc} = \left(\frac{\sigma_{22}}{2F_{ls}}\right)^2 + \left[\left(\frac{F_{2c}}{2F_{ls}}\right)^2 - 1\right]\frac{\sigma_{22}}{F_{2c}} + \left(\frac{\sigma_{12}}{F_{ts}}\right)^2 \geq 1$$

In the above equations, e_{ft}, e_{fc}, e_{mt}, and e_{mc} represents the failure criteria at each mode, which depend on the current stress components. Once failure criteria for each mode reach the value 'one', the damage is initiated. The parameters of F_{1t}, F_{1C} denote tensile and compressive strengths in the axial direction. F_{2t} and F_{2c} denote tensile and compressive strengths in the transverse direction. F_{ls} and F_{ts} denote the longitudinal and transverse shear strengths. This work does not consider the

through-the-thickness failure because the effect of through-the-thickness failure for the bundle is insignificant in a tensile test. The coefficient α $(0 \leq \alpha \leq 1)$ in Eq. (4.1) is employed to determine the contribution of the shear stress on the fiber tensile failure. This coefficient was taken as 'one' in Hashin's and Hou's failure criteria [90, 91]. In Guo's and Li's work, the value is specified as 'zero' [92, 93]. In this study, the coefficient α=0.06 for a fiber bundle of the same material is adopted by work of Zhang et al. [94, 95].

After failure criteria are satisfied, progressive loading results in material stiffness degradation. The damage variables control the stiffness degradation, which Kachanov first proposed through CDM theory [96]. The damage variables play an essential role in representing the softening behavior. The evolution of the damage variables is based on the energy dissipated during the damage process. The crack band model with characteristic element length is adopted to alleviate the mesh dependence [87]. The dissipated energy of the elements is expressed as follows,

$$G_I = \frac{1}{2}\sigma_{I,eq}^{o}\varepsilon_{I,eq}^{o}L_c, \tag{4.2}$$

where G_I is the dissipated energy of each damage mode; $\sigma_{I,eq}^{0}$ and $\varepsilon_{I,eq}^{0}$ are the equivalent stress and strain after the damage occurs; Subscript "*I*" is each of four failure modes (i.e., *I*=*ft*, *fc*, *mt*, and *mc*). Superscript "o" denotes the damage onset. L_c is the characteristic length of the element. The damage variables d_I of each mode are expressed in Eq. (4.3).

$$d_I = \frac{\delta_{I,eq}^{f}\left(\delta_{I,eq} - \delta_{I,eq}^{o}\right)}{\delta_{I,eq}\left(\delta_{I,eq}^{f} - \delta_{I,eq}^{o}\right)}, \tag{4.3}$$

$$\delta_{I,eq}^{0} \leq \delta_{I,eq} \leq \delta_{I,eq}^{f}, \quad I \in \{ft, fc, mt, mc\}$$

$$\delta_{I,eq}^{f} = \frac{2G_I}{\sigma_{I,eq}^{o}}$$

Here, the superscript "f" denotes the fully damaged state. As a result, equivalent displacement and stress are summarized in Table 4.1. In the table, the operator $\langle x \rangle$ is Macauley bracket, which defined as $\langle x \rangle = \frac{x+|x|}{2}$.

Table 4.1. Equivalent displacement and stress with characteristic length

Failure Mode	δ_{eq}	σ_{eq}
Fiber tension ($\sigma_{11} > 0$)	$L_c\sqrt{\langle \varepsilon_{11} \rangle^2 + \alpha(\varepsilon_{12}^2 + \varepsilon_{13}^2)}$	$\frac{L_c(\langle \sigma_{11} \rangle \langle \varepsilon_{11} \rangle + \alpha(\sigma_{12}\varepsilon_{12} + \sigma_{13}\varepsilon_{13}))}{\delta_{ft,eq}}$
Fiber compression ($\sigma_{11} < 0$)	$L_c\langle -\varepsilon_{11} \rangle$	$\frac{L_c\langle -\sigma_{11} \rangle \langle -\varepsilon_{11} \rangle}{\delta_{fc,eq}}$
Matrix tension ($\sigma_{22} > 0$)	$L_c\sqrt{\langle \varepsilon_{22} \rangle^2 + \varepsilon_{12}^2 + \varepsilon_{23}^2}$	$\frac{L_c(\langle \sigma_{22} \rangle \langle \varepsilon_{22} \rangle + \sigma_{12}\varepsilon_{12} + \sigma_{23}\varepsilon_{23})}{\delta_{mt,eq}}$
Matrix compression ($\sigma_{22} < 0$)	$L_c\sqrt{\langle -\varepsilon_{22} \rangle^2 + \varepsilon_{12}^2}$	$\frac{L_c(\langle -\sigma_{22} \rangle \langle -\varepsilon_{22} \rangle + \sigma_{12}\varepsilon_{12})}{\delta_{mc,eq}}$

The damage model is adopted following Matzenmiller et al. [97]. to estimate stiffness degradation using damage variables. In this model, the relation between nominal stress $\boldsymbol{\sigma}$ and effective stress $\hat{\boldsymbol{\sigma}}$ are expressed with the damage operator $\boldsymbol{M}$.

$$\hat{\boldsymbol{\sigma}} = \boldsymbol{M}:\boldsymbol{\sigma}, \text{ where } \boldsymbol{M} = \begin{bmatrix} \frac{1}{d_f} & & & & & \\ & \frac{1}{d_m} & & & & \\ & & 1 & & & \\ & & & \frac{1}{d_s} & & \\ & & & & \frac{1}{d_f} & \\ & & & & & \frac{1}{d_m} \end{bmatrix} \tag{4.4}$$

Here, d_f, d_m, and d_s are the global damage variables associated with fiber, matrix, and shear components. They have a relation with specific modes, which consist of tension and compression.

$$\begin{aligned} d_f &= (1 - d_{ft})(1 - d_{fc}) \\ d_m &= (1 - d_{mt})(1 - d_{mc}) \\ d_s &= (1 - d_{ft})(1 - d_{fc})(1 - d_{mt})(1 - d_{mc}) \end{aligned} \tag{4.5}$$

In the above equations, the subscript t and c denotes tension and compression, which means there are four kinds of damage variables (e.g., d_{ft}, d_{fc}, d_{mt}, d_{mc}). Using these descriptions, the 3D damaged compliance matrix $S(d_I)$ has the following form.

$$\boldsymbol{S}(d_I) = \begin{bmatrix} \frac{1}{d_f E_{11}} & -\frac{\nu_{21}}{E_{22}} & -\frac{\nu_{31}}{E_{33}} & & & \\ -\frac{\nu_{12}}{E_{11}} & \frac{1}{d_m E_{22}} & -\frac{\nu_{32}}{E_{33}} & & & \\ -\frac{\nu_{13}}{E_{11}} & -\frac{\nu_{22}}{E_{22}} & \frac{1}{E_{33}} & & & \\ & & & \frac{1}{d_s G_{12}} & & \\ & & & & \frac{1}{d_f G_{13}} & \\ & & & & & \frac{1}{d_m G_{23}} \end{bmatrix} \tag{4.6}$$

The viscous regularization method and limiting factor of 0.8 for the damage variables are utilized to reduce damage localization and improve convergence. The elastic parameters are adopted from our previous study which investigated the mechanical properties of fiber bundles through numerical homogenization with microstructure [71]. The constants of progressive Hashin's failure used in the analysis are listed in Table 4.2 [40]

Table 4.2. Material parameters of a carbon fiber bundle

Parameters	**Value**
Longitudinal modulus, E_1 (GPa)	203.29
Transverse modulus, E_2 (GPa)	11.639
Shear modulus, $G_{12} = G_{13}$ (GPa)	5.027
Shear modulus, G_{23} (GPa)	4.206
Poisson's ratios, $\nu_{12} = \nu_{13}$	0.017
Poisson's ratios, ν_{23}	0.349
Longitudinal tensile strength, F_{1t} (MPa)	2157
Longitudinal compressive strength, F_{1t} (MPa)	1270
Transverse tensile strength, F_{2t} (MPa)	78
Transverse compressive strength, F_{2c} (MPa)	113
Longitudinal shear strength, F_{ls} (MPa)	109
Transverse shear strength, F_{ts} (MPa)	100
Fracture energy, $G_{1t} = G_{1c}$ (kJ/m^2)	12
Fracture energy, $G_{2T} = G_{2c}$ (kJ/m^2)	1

4.2.2 Ductile damage plasticity model for vinyl ester resin

In this work, the vinyl ester resin for the matrix phase is modeled as an isotropic solid. The damage plasticity model is defined by the yield criterion and plastic flow rule accounting for the Lemaitre-Chaboche damage behavior in the matrix region [88]. The material parameters for the matrix are characterized through inverse

identification based on the experiment results [98]. The procedures of inverse identification and material constitutive model are provided in Appendix B. The characterized material parameters are summarized in Table 4.3.

Table 4.3. Material parameters of matrix

Parameter	Values
Elastic Modulus, E (GPa)	3.158
Poisson ratio, ν	0.312
Initial yield stress, σ_{y0} (MPa)	68.3
Hardening parameter, k (MPa)	447
Hardening parameter, m	0.0074
Damage parameter, S_0	0.235
Damage parameter, s	2.189

4.2.3 Traction-separation law for interface

A cohesive zone model is employed to simulate delamination initiation and propagation at the contact face of adjacent bundles and the interface between bundle and matrix. Before the onset of delamination, an elastic traction-relative displacement law is specified to hold together the interface of the adjacent elements, and an uncoupled traction-relative displacement law is expressed in terms of three traction stresses, as follows,

$$\begin{Bmatrix} t_n \\ t_s \\ t_t \end{Bmatrix} = (1-D)\begin{bmatrix} K_{nn} & 0 & 0 \\ 0 & K_{ss} & 0 \\ 0 & 0 & K_{tt} \end{bmatrix}\begin{Bmatrix} u_n \\ u_s \\ u_t \end{Bmatrix}, \tag{4.7}$$

where t_n, t_s and t_t represent the normal and two shear traction stress components, respectively. u_n, u_s and u_t are the corresponding separations. K_{nn}, K_{ss} and K_{tt} are the penalty stiffness parameters. D denotes the overall damage variable in the material. The penalty stiffnesses are set to $5 \times 10^4 \mathrm{MPa/mm}$, which is assumed as $K_{nn} = K_{ss} = K_{tt}$.

After the onset of delamination, the behavior of the interface is controlled by a softening law for delamination propagation. The maximum stress criterion is used for damage initiation, as follows,

$$Max\left[\frac{\langle t_n \rangle}{t_n^{max}}, \frac{t_s}{t_s^{max}}, \frac{t_t}{t_t^{max}}\right] = 1, \tag{4.8}$$

where t_n^{max}, t_s^{max}, and t_t^{max} are the maximum stress in the normal direction and two shear directions. The tension and shear traction-separation responses are considered to be independent of one another. $\langle \quad \rangle$ is a Macaulay bracket, showing that no damage occurs under pure compression. In the numerical simulation, the cohesive strengths are set to $t_n^{max} = 80\mathrm{MPa}$, $t_s^{max} = t_t^{max} = 150\mathrm{MPa}$.

The crack propagation is described as $\frac{G_I}{G_{IC}} + \frac{G_{II}}{G_{IIC}} + \frac{G_{III}}{G_{IIIC}} = 1$, linear fracture mechanics law. G_I, G_{II}, and G_{III} are the energy release rates with respect to traction and separation. The critical fracture energy is denoted by subscripted "C". The numerical values for the critical energy release rates are adopted as $G_{IC} = 1.436\mathrm{kJ/m^2}$ and $G_{IIC} = G_{IIIC} = 2.380\mathrm{kJ/m^2}$ from previous research [99].

4.3 Results and Discussion

4.3.1 Effect of fiber bundle orientation

First, the mechanical properties' changes of SMC composites are investigated according to fiber bundle orientation. The size of the plate and fiber bundle is set to $300 \times 300 \times 3\text{mm}^3$ and $30 \times 10\text{mm}^2$, respectively, to generate a reconstructed molded SMC plate. The plate is modeled to have ten layers. Thus each layer has a thickness of 0.3mm. Reconstructed molded plates composed of 60% fiber bundle volume fraction are generated according to different bundle orientation distributions, as depicted in Figure 4.1.

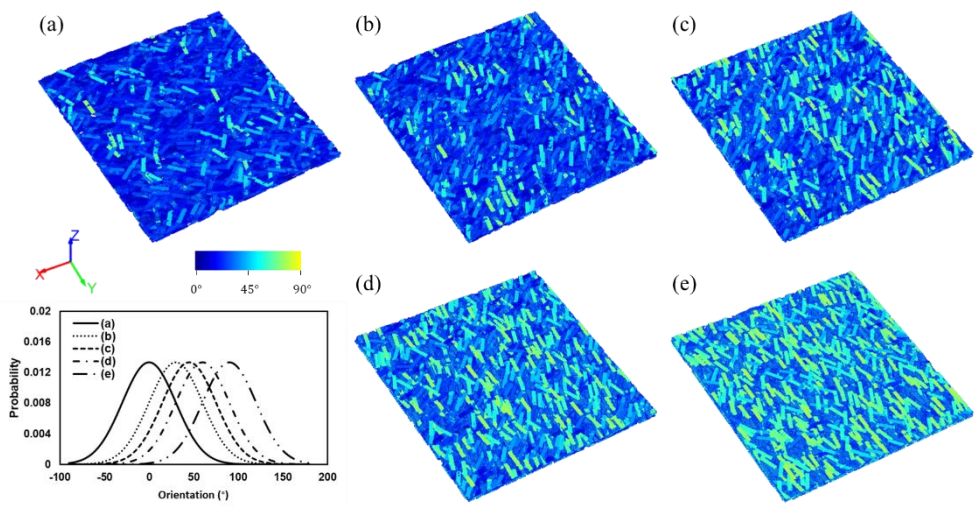

Figure 4.1. The SMC RVE samples under the different distribution of orientation (σ=30)

The bundle orientations are expressed based on the Gaussian function, a function of a mean value (μ) and standard deviation (σ). SMC molded plates with different

morphologies are created by changing the mean value while the standard deviation is fixed at 30. The contour color of fiber bundles varies depending on the orientation in the plate. When the bundle is aligned to the x-axis direction (zero-degree), it has a blue color. On the other hand, the yellow color appears if it is placed in the y-axis direction (ninety-degree). In this simulation, the orientation of the bundle is only used as a variable. Thus, uniform bundle dispersion is assumed to be a control variable. Therefore, the local volume fractions at the preset points are equal to each other. Because the reconstructed SMC plates are only statistically identical, each sample inevitably has a different mesoscale structural morphology, which leads to a deviation of simulation results at every sample. For this reason, a total of six tensile specimens are prepared. Displacement-control loading is applied to the specimen in the x-axis direction, and nonlinear simulation is performed with a sufficient number of increments. The macroscopic strain and stress are calculated as the elongation divided by the gage length and the reaction force divided by the cross-sectional area.

Figure 4.2(a) shows the stress-strain curves of the specimens following distribution with mean values of zero, forty-five, and ninety degrees. The curves show linear dominant behavior, which is one of the characteristics of carbon fiber-reinforced composites. To evaluate the mechanical properties of SMC composites, the modulus and strength are measured by the initial slope within 0.05 to 0.25% strain range and the ultimate maximum strength of the stress-strain curve, respectively.

(a)

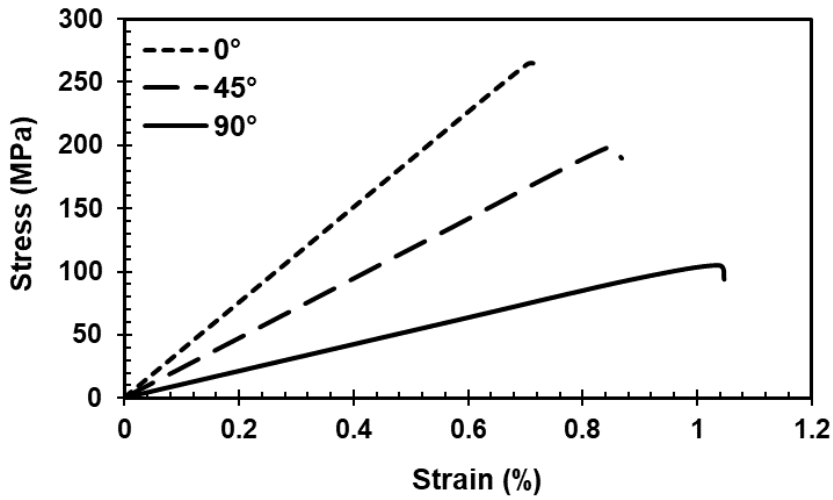

(b)

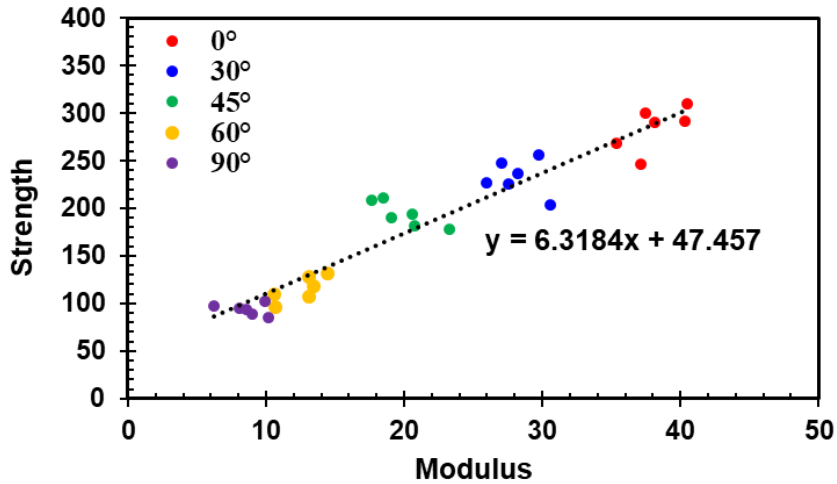

Figure 4.2. Results according to fiber bundle orientation: (a) Stress-strain curves (b) Relationship between modulus and strength

The results of specimen samples are plotted in the modulus-strength domain, and five groups according to the mean value of the orientation distribution are distinguished by different colors, depicted in Figure 4.2(b). Depending on the bundle

orientation, the modulus and strength have a positive correlation, expressed through a linear equation. Next, while the modulus shows the same level of deviation for each orientation group, it is seen that the deviations are large at zero and thirty degrees. On the contrary, the specimen with forty-five or more has a low deviation in strength, and this tendency of failure of SMC composites is elucidated through the damage patterns. Figure 4.3 shows damage contours that occur in the fiber bundle and matrix of the specimen with zero and ninety degrees.

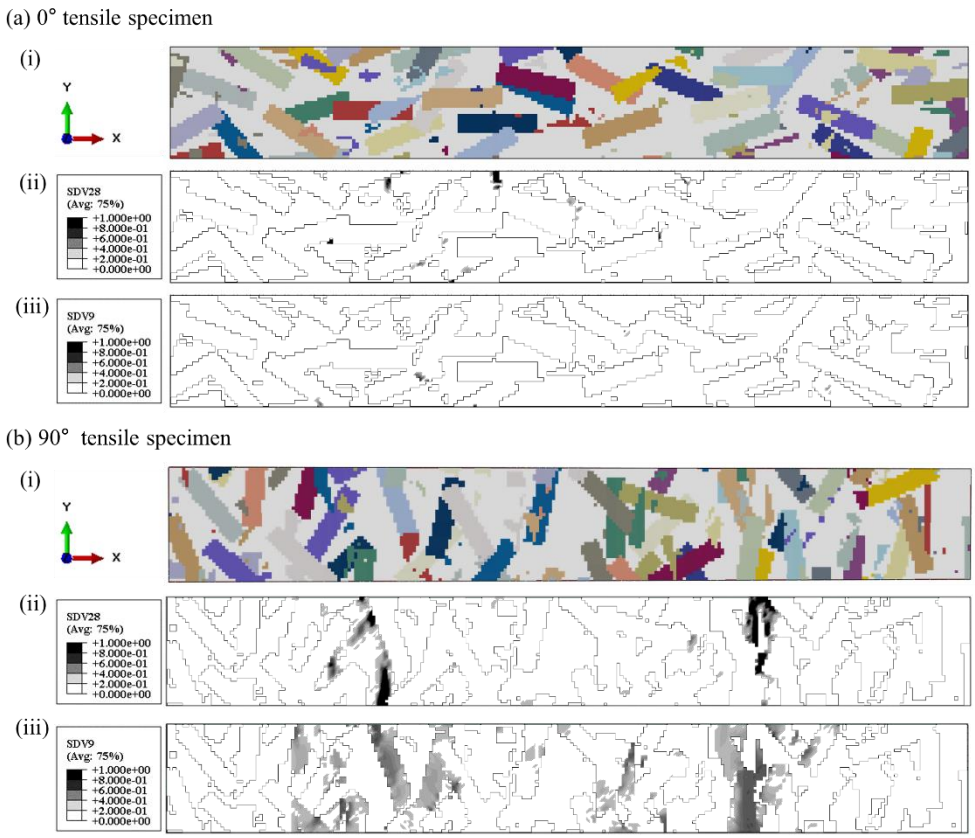

Figure 4.3. The geometry of specimen and damage occurrence in fiber bundle and

matrix.

Figure 4.3(i) shows the geometry in the x-y plane of the specimen composed of different colors of individual fiber bundles. Figure 4.3(ii) and (iii) are damage contours of the matrix and fiber bundle, respectively. Based on the damage contour in specimens with different orientations, the following characteristics are summarized. In the case of the ninety-degree specimen subjected to a uniaxial loading, the damage is shown equally to the fiber bundle and matrix. However, the zero-degree specimen shows the damage concentrated at the interface between constituents or the end location of the fiber bundle. Therefore, if the orientation of the fiber bundle coincides with the loading direction, unexpected damage is experienced due to the emergence of damage at a local location from stress concentration. Next, it is observed that the damage is dominant in the matrix region in both simulation cases. It is a characteristic of SMC composites subjected to tensile loading and confirmed in experiments [100]. Carbon fibers loaded in the longitudinal direction show superior resistance to the tensile direction than the compression direction, and this feature is extended to the fiber bundle. However, because the strength is too high in these two directions, longitudinal damage rarely occurs. In addition, since the fiber bundle composed of continuous fibers aligned in the longitudinal direction is vulnerable to transverse directional loading, transverse damage related to the matrix properties has emerged quickly. As a result, it is demonstrated that the failure of SMC composites in terms of macroscopic behavior is highly related to the matrix properties.

4.3.2 Mechanical properties depending on the dispersion

Next, the change of modulus and strength of SMC composite material according to the dispersion of fiber bundles is observed. The dispersion of the fiber bundle is defined based on the distribution of the local volume fraction calculated at preset points in the molded plate. In this modeling, fiber bundles with random orientation are packed to follow the target local volume fraction distribution. The statistic of bundles' local volume fraction is also generated through the Gaussian function by adjusting the mean value and coefficient of variation (COV). The conditions for modeling are the same as in Chapter 3.1. According to the COV, recombined molded plates with a fiber bundle volume ratio of 60% are generated and classified into six groups. Figure 4.4 shows the 3D view of reconstructed models and a 2D binary image on the XY-plane corresponding to each group.

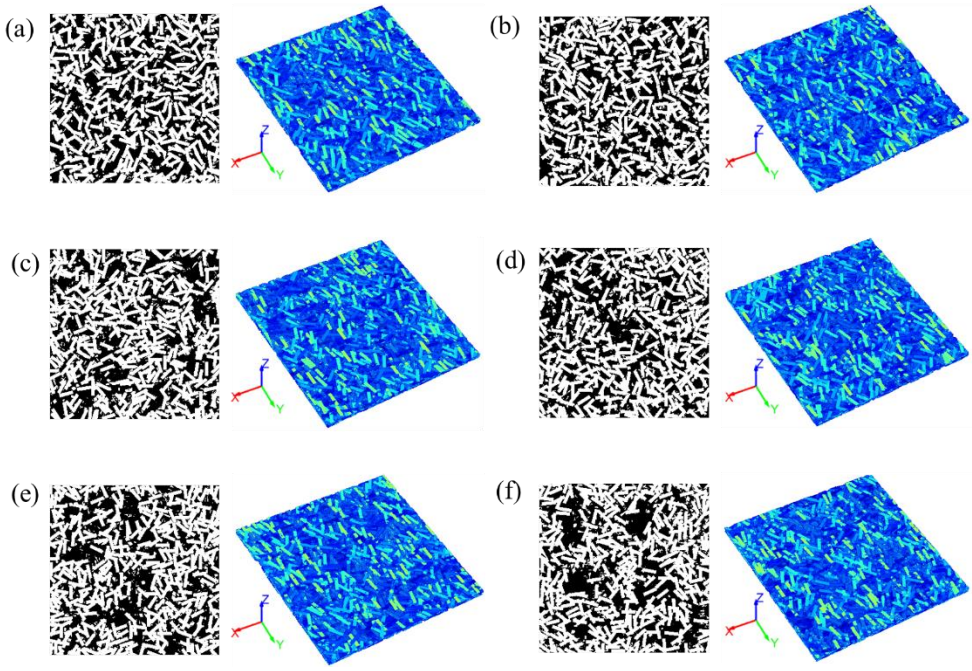

Figure 4.4. The SMC RVE samples under the different distribution of local volume fraction (dispersion): (a) 0.01 (b) 0.1 (c) 0.2 (d) 0.3 (e) 0.4 (f) 0.5.

The 2D binary images demonstrate that the COV of the local volume fraction distribution directly affects the position of the fiber bundle on the plate. A reconstructed model produces an imbalanced geometry as the COV increases. The voids in the layers can represent the matrix-rich area of natural SMC composites. Thus, when a specimen is cut out of a reconstructed plate with a high COV, the fiber bundle varies from specimen to specimen, directly related to the tensile behavior. For this reason, many specimens for statistical analysis are prepared for each group.

(a)

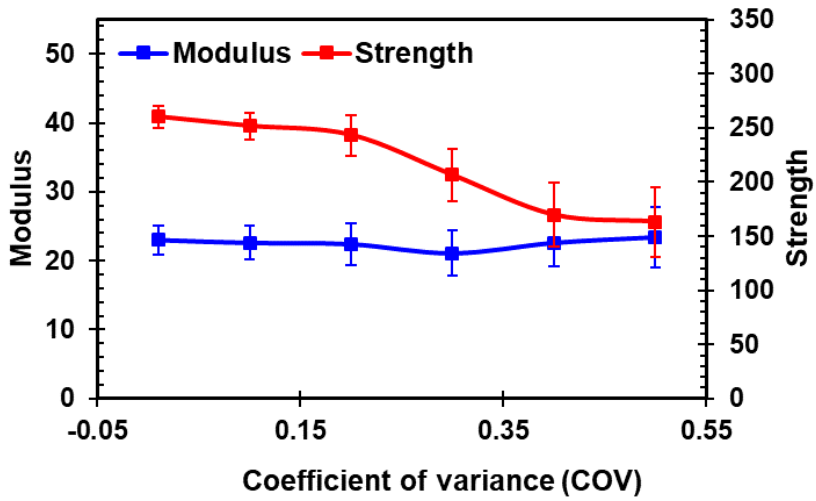

(b)

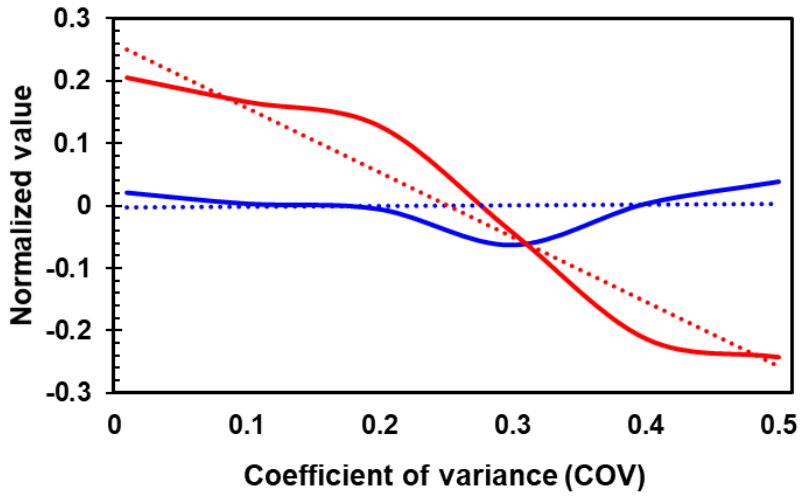

Figure 4.5. The modulus and strength according to the dispersion

Figure 4.5 illustrates the results of modulus and strength according to COV using fifteen tensile specimens per group. The line and error bar of the graph represents the average value and standard error of the results, respectively. Modulus and strength are expressed in blue and red, and the range of values is indicated on the left

and right axes, respectively. Several changes in the graph are observed as the COV changes. First, when measuring a standard error using multiple samples, it is seen that it grows with an increase in COV in both modulus and strength. A sizeable morphological difference occurs for each sample when the specimen is produced in the SMC plate with clumped dispersion of fiber bundle. Furthermore, as the COV increases, while the modulus hardly changes, the strength tends to decrease remarkably. In particular, it shows a drastic change in the 0.2-0.4 range because the morphological imbalance is noticeable in that range, as shown in Figure 4.4. This trend is more pronounced when normalized to the average value, as shown in Figure 4.5(b). Also, it is possible to predict the degradation rate of the SMC composite material according to the COV through the normalized trend line.

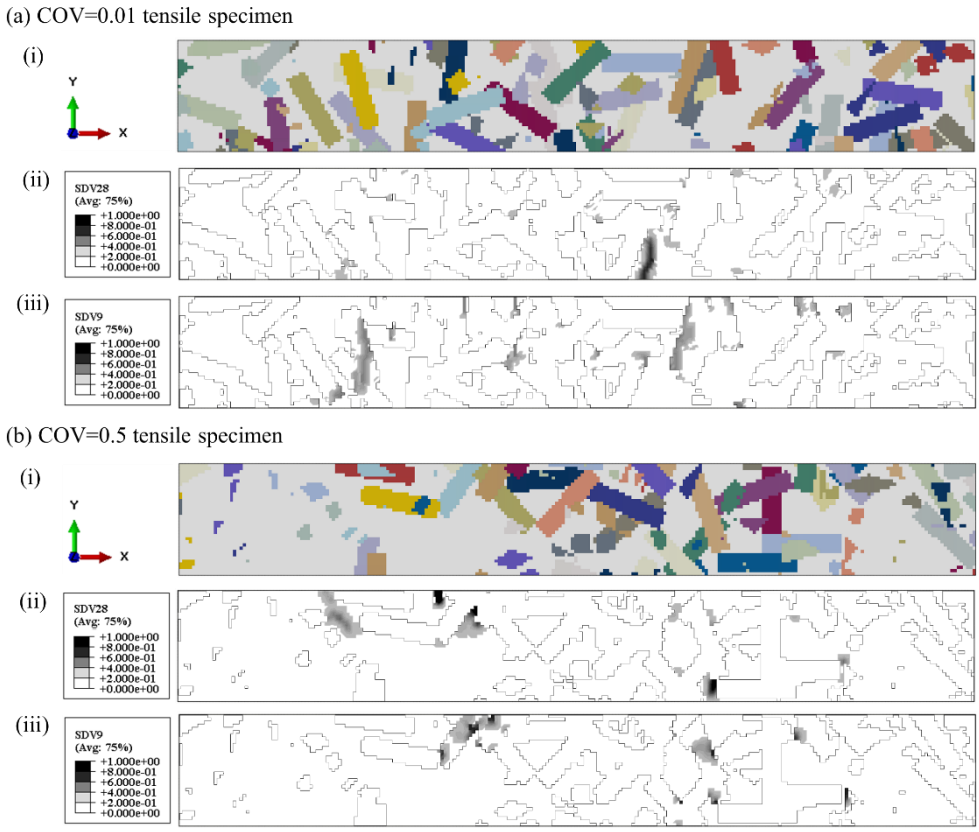

Figure 4.6. The geometry of specimens and damage occurrence in the fiber bundle and matrix

Figure 4.6 shows the damage patterns in the specimens with different bundle dispersion. The damage pattern is widely distributed in a specimen with a uniform bundle distribution of COV=0.01 because the load transmission is uniformly performed. Therefore, uniform results are expected for each specimen. In contrast, specimens with a clumped dispersion of COV=0.5 have morphological imbalances resulting in warped deformation in the tensile direction and deformation in other directions. Therefore, in samples with clamp dispersion, deformations other than the

tensile direction are prominent. It is explained by Figure 4.7, which shows the z-direction deformation contour with ten times scaling into the z-direction deformation for specimens with different bundle dispersions. The initial elastic behavior is consistent because both models consist of fiber bundles with 60% volume fraction and random orientation. However, morphological imbalance due to clumped bundle dispersion rapidly develops local damage, and it tends to fail faster than in uniform bundle dispersion.

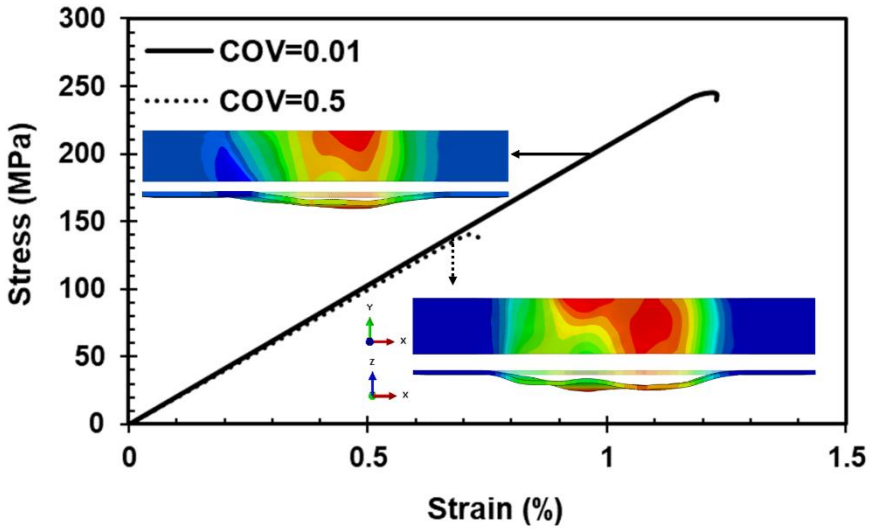

Figure 4.7. The stress-strain curves of specimens with different dispersion of fiber bundles

4.4 Experiemental Validation

4.4.1 Effect of fiber bundle orientation

As manufacturing-dependent parameters for the reconstruction algorithm, the dimensions of the SMC molded plate and fiber bundle are designed. A series of reconstructed layers following the statistical indicators of real-life SMC composites are obtained. After that, the realization of an individual specimen produces different morphology of mesostructures, allowing the numerical study of a multiscale model. Five tensile specimens are prepared as in the experiment. Because carbon fiber tows have $200\sim300\ \mathrm{g/m^2}$ fiber areal weight (FAW), which assumes that they have a $0.2\mathrm{mm}\sim0.3\mathrm{mm}$ thickness, the individual tensile specimens consist of seven layers as discussed in our previous study [71]. The reconstructed molded plate and specimens are summarized in Figure 4.8.

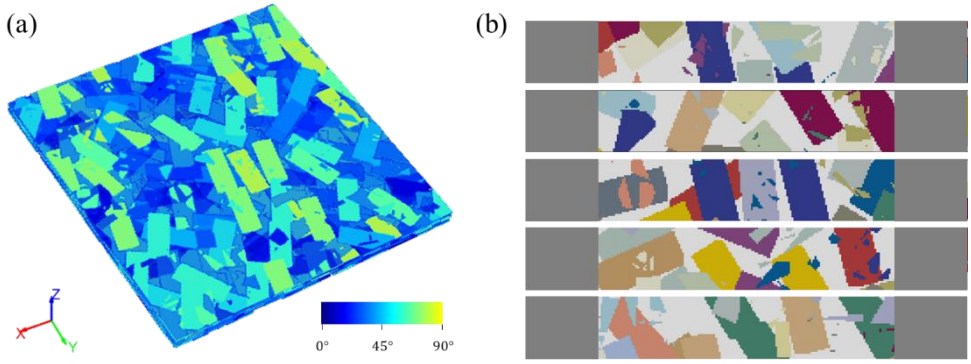

Figure 4.8. A reconstructed molded plate and specimens using characterized statistical indicators

(a)

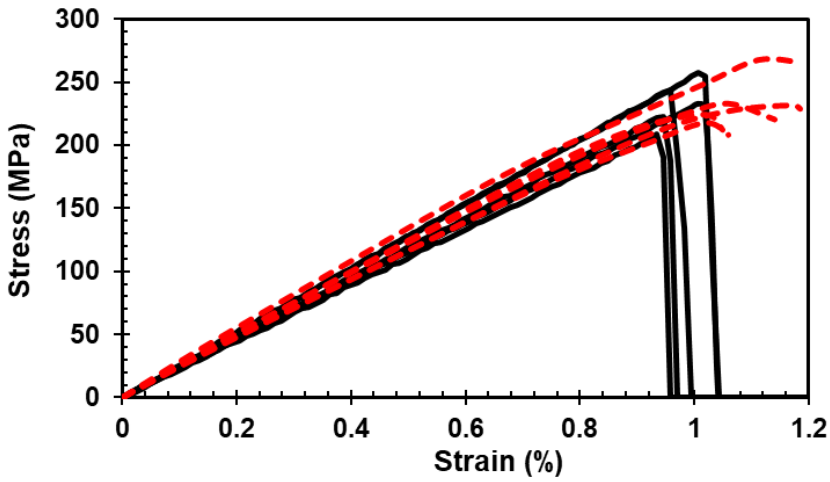

(b)

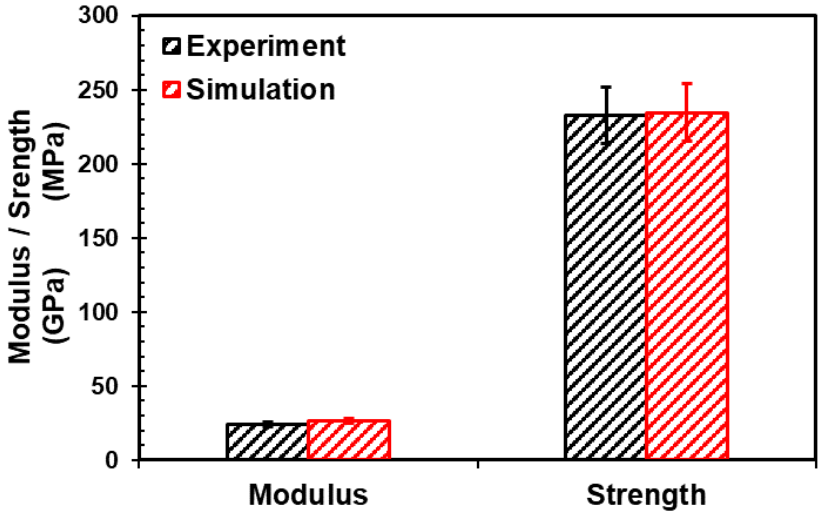

Figure 4.9. Comparison simulation results with experiments

Table 4.4. Mechanical properties from experiment and simulation

Description	Mechanical properties						
	#1	#2	#3	#4	#5	Average	COV
Experiment							
Modulus (GPa)	22.21	22.98	25.63	25.40	23.59	23.96	0.062
Strength (MPa)	208.2	232.5	257.6	243.8	222.6	232.9	0.081
Simulation							
Modulus (GPa)	25.88	28.69	24.73	26.86	24.52	26.14	0.065
Strength (MPa)	223.7	267.4	217.2	233.0	231.3	234.5	0.082

The stress-strain curves from the simulation and experiment are co-plotted in Figure 4.9(a). The experiment and simulation results are expressed in solid black lines and red dotted lines, respectively. Figure 15(b) shows quantitative comparisons of experimental and simulation results. The deviation of mechanical properties, as well as the average value, is successfully compared. The estimated value of each specimen is summarized in Table 4.4.

4.4.2 Comparison with failure patterns of SMC composites

After validating the proposed reconstruction modeling, failure patterns of SMC composites are observed through the EmCrafts Cube-II scanning electron microscope (SEM) machine to verify the constitutive material models. As shown in Figure 4.10, failure patterns are summarized as matrix failure, fiber breakage, and

delamination. Figure 4.10(a) shows the matrix failure in the resin-rich area. Because the mechanical properties of the matrix are lower than that of the fiber, the failure occurs mainly in the resin-rich area. Figure 4.10(b) shows delamination occurring at the interface between fiber bundles. It leads to matrix cracking in the fiber bundle. As a result, the failure primarily happened in the matrix region. Figure 4.10(c)-(d) shows fiber breakage and delamination between fiber and matrix. This fiber breakage has the role of load transferring until the breakage of the SMC composite material. Thus fiber breakage means complete breakage of the tensile specimen.

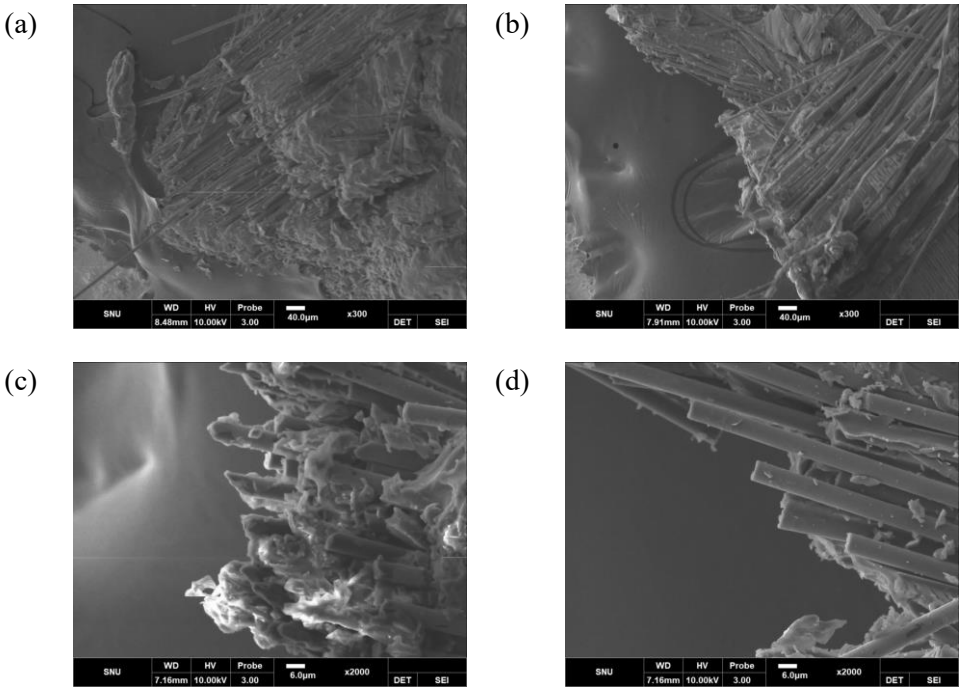

Figure 4.10. Morphological failure patterns: (a) Matrix failure in the resin-rich area (b) Matrix cracking from delamination between fiber bundles (c) Fiber breakage

(d) Fiber pullout from delamination between fiber and matrix

The observation of SEM scanning shows the microscopic failure patterns which lead to mesoscopic failure patterns indicated in Chapter 4.4. It is explicitly considered through the constitutive material models in this study. Furthermore, the simulation results reveal the evolution of damage accumulation corresponding to each damage mechanism, which is understood in-situ according to the loading conditions.

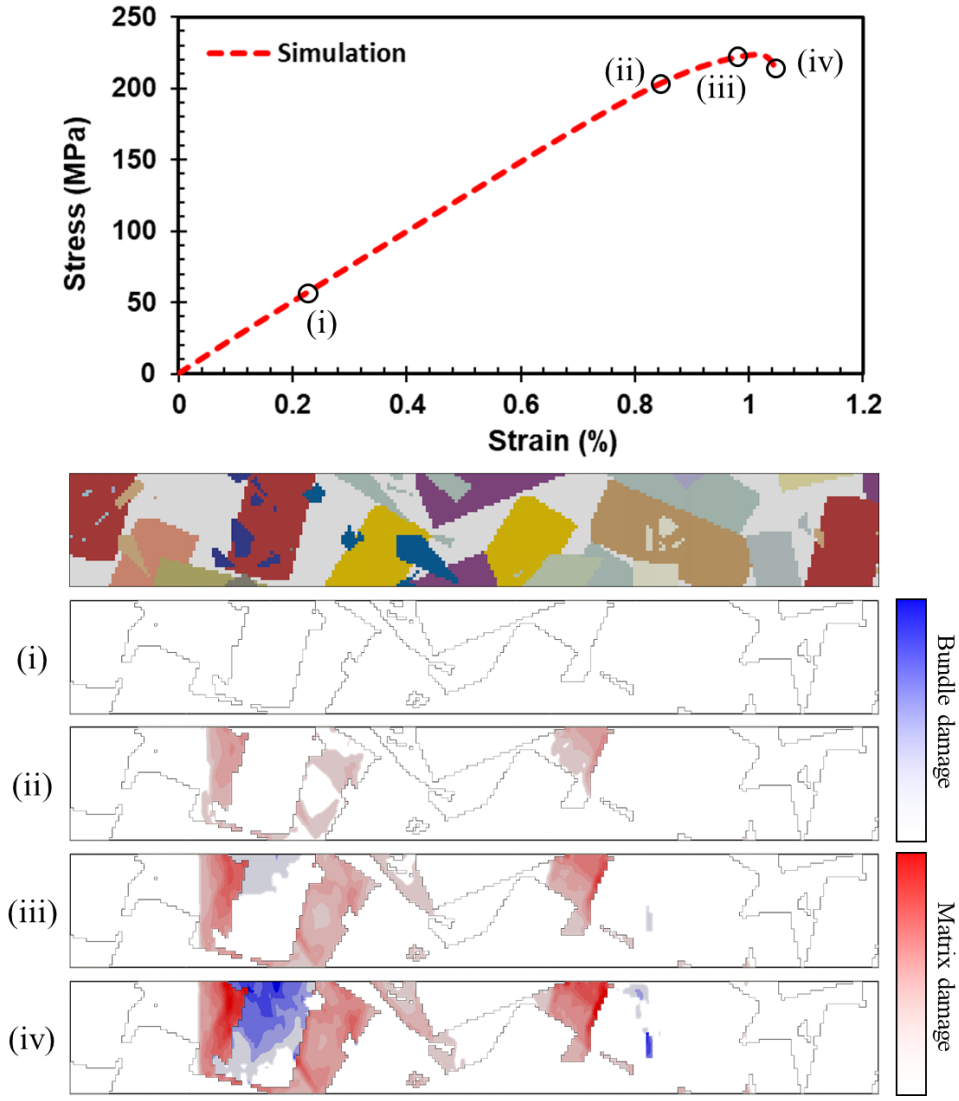

Figure 4.11. Damage evolution of individual constituents according to the loading history

Figure 4.11 expresses the damage occurring in each material constitutive model according to the loading history. No damage occurs in an initial state. However, as the loading increases, damage begins to take place in the matrix and interface regions.

Although additional loading also causes damage to the fiber bundle, the transverse direction failure of the fiber bundle dominates, which means that failure in the matrix occurs mainly in simulation. Since this analysis is implicit, the SMC specimen's complete failure cannot be observed due to the convergence problem. Therefore, there is a limit to observing up to the longitudinal direction failure in the fiber bundle. Moreover, because only mesoscopic damage of SMC composites is considered in this research, the delamination between fiber and matrix in microstructure is not investigated. However, as observed by SEM and experiments, major failure occurs in the matrix. These results indicate successful material constitutive modeling and the proposed reconstruction algorithm for SMC composites.

Chapter 5. Micromechanics model for SMC composites

In this chapter, a novel hierarchical micromechanics model is presented through a multi-step homogenization method. There are three steps for homogenization in terms of a fiber bundle, SMC layer, and SMC composite. The first homogenization is to model the fiber bundles with wavy fibers. The waviness is implemented by a polynomial mathematical expression, a curve-fitting result, and the selected points from the prescribed normal distribution. Next, the second homogenization is to model the fiber bundles with direction on a single layer. A rotational transformation is applied to express the rotated fiber bundle. The overlapping between the fiber bundles is also considered through multi-site (MS) Mori-Tanaka (MT) modeling. Finally, the third homogenization is introduced by the Rule of Mixtures (ROM) and bonds the individual layers into solid SMC composites. The integration of J_2 flow rule and Lemaitre-Chaboche damage model are achieved to express the nonlinear behavior of SMC composites. The effects of fiber waviness and fiber bundles' orientation on mechanical performance are evaluated by parametric study. Moreover, the validity of the proposed model is demonstrated by comparing it with the result of the literature.

5.1 Hierarchical Micromechanics Model for SMC composites

A hierarchical micromechanics model using multi-step homogenization is utilized for SMC composites. In particular, the overlapping between fiber bundles could

significantly influence the mechanical properties of the composites. The multi-step homogenization method proposed in this section can realize such real-life mesostructure morphology in the MT model with computational efficiency [101].

There are three steps for evaluating the effective behavior of SMC composites. The first homogenization step is to model individual fiber bundles. The second homogenization step is to model a unit SMC layer comprising the randomly oriented fiber bundles and resin. The third homogenization step is performed based on the Rule of Mixtures (ROM) to estimate the effective properties of the final SMC composite. The schematic flows for multi-step homogenization are depicted in Figure 5.1.

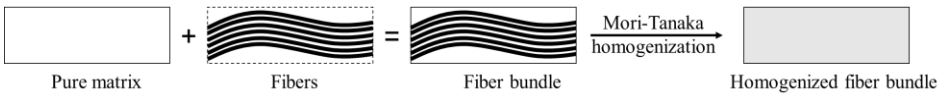

(a) First homogenization: homogenized fiber bundles

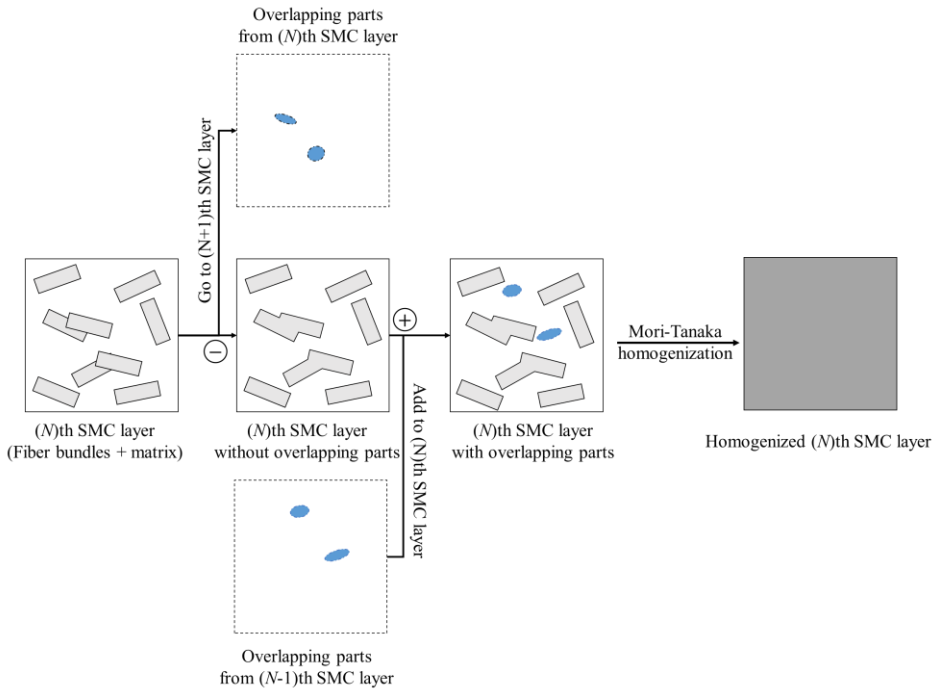

(b) Second homogenization: homogenized SMC individual layers

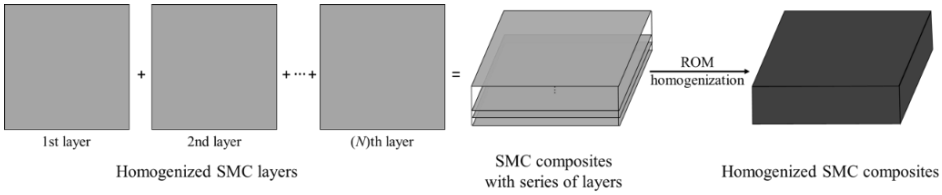

(c) Third homogenization: homogenized SMC composites

Figure 5.1. The procedure for the proposed multi-homogenization method

5.1.1 First homogenization: Modeling Fiber bundle with wavy fibers

The first homogenization models a bundle with wavy fibers by the OS MT method. The projection length of fiber on the x-axis is firstly designated to express the wavy fibers in the bundles. By generating z-coordinate values for the locations along the x-axis, the wavy fiber can take any arbitrary shape on the x-z plane.

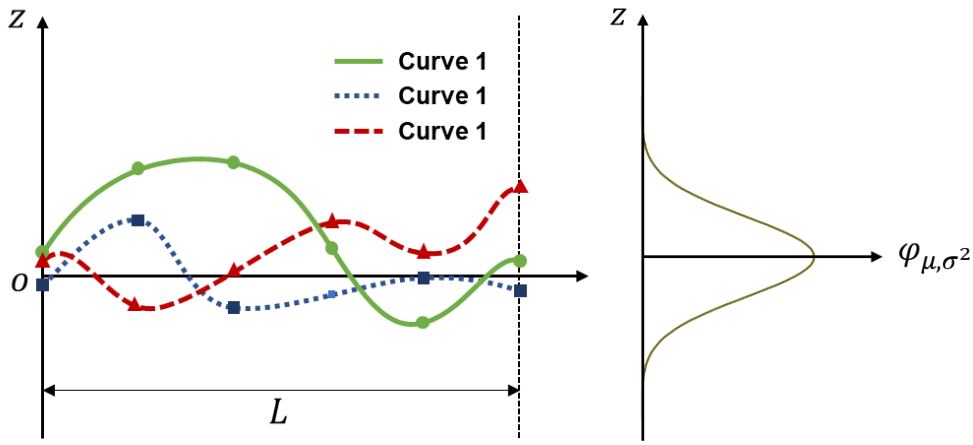

(a) (b)

Figure 5.2. (a) Randomly wavy fibers, (b) Probability function of a z-coordinate value

In Figure 5.2, three wavy fibers are exhibited by the same fiber projection length L with six points. These are made of equidistant x-coordinate values and arbitrary z-coordinate values. The arbitrary z-coordinate values are determined by random sampling from a preset normal distribution. Therefore, a standard derivation of the normal distribution can control the degree of fibers' waviness. As the standard derivation increases, the waviness of the fiber becomes more random. For the straight fiber, the standard deviation of the normal distribution is set to zero.

As shown in Figure 5.3, a fiber is assumed to lie on the x-z plane. L and W indicate the length and width of fiber bundles, respectively. The wavy fiber is in a polynomial mathematical expression, $z(x) = ax^3 + bx^2 + cx + d$. The coefficients are determined by curve-fitting. It is necessary to calculate the gradient along the x-axis. An analytical differentiation determines the gradient along with the wavy fiber.

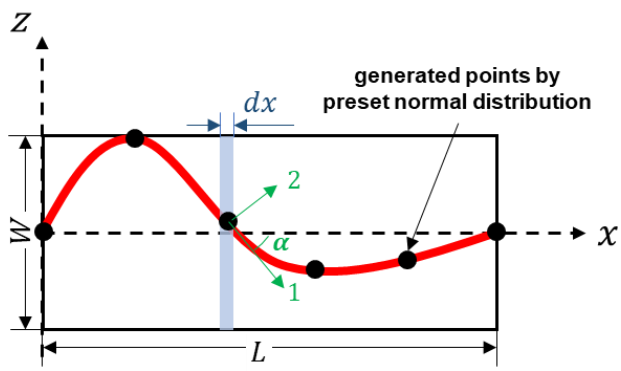

Figure 5.3. Representation of random fiber waviness

From the global to local coordinates system, the stress and strain tensors are converted through a rotational transformation tensor $[T_{ij}]$, as follows:

$$\begin{bmatrix} \sigma_{xx} \\ \sigma_{yy} \\ \sigma_{zz} \\ \tau_{yz} \\ \tau_{xz} \\ \tau_{xy} \end{bmatrix} = [T_{ij}]^{-1} \begin{bmatrix} \sigma_{11} \\ \sigma_{22} \\ \sigma_{33} \\ \tau_{23} \\ \tau_{13} \\ \tau_{12} \end{bmatrix} \text{ and } \begin{bmatrix} \varepsilon_{xx} \\ \varepsilon_{yy} \\ \varepsilon_{zz} \\ \gamma_{xy} \\ \gamma_{xz} \\ \gamma_{xy} \end{bmatrix} = [T_{ij}]^{-1} \begin{bmatrix} \varepsilon_{11} \\ \varepsilon_{22} \\ \varepsilon_{33} \\ \gamma_{23} \\ \gamma_{13} \\ \gamma_{12} \end{bmatrix} \tag{5.1}$$

$[T_{ij}]$ is expressed using fiber angle α, which is expressed as

$$T_{ij} = \begin{bmatrix} m^2 & 0 & n^2 & 0 & 2mn & 0 \\ 0 & 1 & 0 & 0 & 0 & 0 \\ n^2 & 0 & m^2 & 0 & -2mn & 0 \\ 0 & 0 & 0 & m & 0 & -n \\ -mn & 0 & mn & 0 & m^2 - n^2 & 0 \\ 0 & 0 & 0 & n & 0 & m \end{bmatrix} \tag{5.2}$$

, where $m = \cos\alpha$ and $n = sin\,\alpha$.

As shown in Figure 5.3, the angle α is determined by the derivative of $z(x)$. Using the line integral with $[T_{ij}]$ in Eq. (5.2), the stiffness matrix in the global coordinates system can be transformed into the local coordinates system as follows:

$$\boldsymbol{C}_{wavy}^{bundle} = \frac{1}{L}\int_0^L T_{ij}^{-1}\,\boldsymbol{C}^{MT} T_{ij} dx \tag{5.3}$$

Here, $\boldsymbol{C}^{MT}$ is the effective stiffness of the fiber bundle with the unidirectional fiber from Eq. (2.24), which can also be denoted as $\boldsymbol{C}_{straight}^{bundle}$. Finally, the stiffness of a single wavy fiber bundle is obtained through the rotational transformation expressed in Eq. (5.3). Figure 5.4 illustrates the modeling procedures of the fiber bundle. f_m and f_f are the volume fractions of the matrix and fiber, respectively.

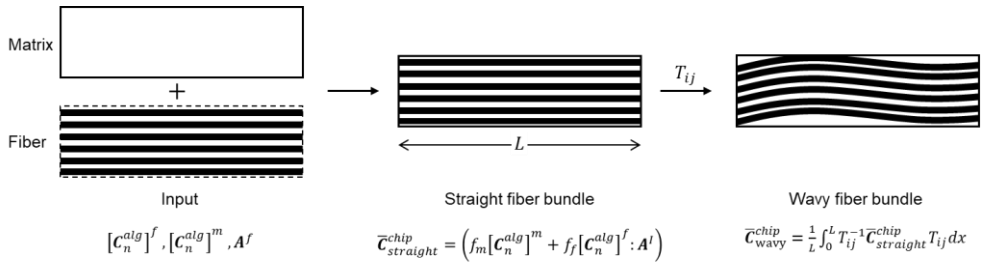

Figure 5.4. The micromechanics modeling of a wavy fiber bundle

5.1.2 Second homogenization: Modeling unit SMC layer with directional flow and overlapping parts

Next, the second MT modeling and homogenization are performed by embedding the fiber bundles with the desired orientation into the SMC layer. In the classical Mori-Tanaka homogenization, the fiber bundles are aligned to the x-axis direction in the global coordinate system. However, in the case of SMC composites manufactured by the compression molding process, the fiber bundles could be non-uniformly oriented. Therefore, each layer of SMC composites comprises non-uniformly oriented fiber bundles. Effects of such non-uniform orientation on the effective properties of the composites are evaluated through an orientation averaging tensor, which is initially proposed by Odegard et al. [102]. The stiffness tensor with the direction of the SMC layer is expressed in Eq. (5.4).

$$\boldsymbol{C}^{layer} = \left(f_0 \boldsymbol{c}^0 + \sum_{I=1}^{N} f_I \langle \boldsymbol{c}^I : \boldsymbol{a}^I \rangle \right) : \left(f_0 \langle \boldsymbol{a}^0 \rangle + \sum_{I=1}^{N} f_I \langle \boldsymbol{a}^I \rangle \right)^{-1} \tag{5.4}$$

In this equation, the inclusion stiffness ($\boldsymbol{c}^I$) is replaced into $\boldsymbol{C}_{wavy}^{chip}$ in the first homogenization step. The fiber bundles are considered inclusions in the second homogenization for the SMC layer modeling. The notation $\langle \quad \rangle$ represents the orientation-averaging tensor computed by Eq. (5.5), as follows,

$$\langle X \rangle_{ijkl} = \frac{\int_0^{\frac{\pi}{2}} \int_{-\pi}^{\pi} X'_{ijkl}(\phi, \theta) \lambda(\theta) sin\theta d\phi \, d\theta}{\int_0^{\frac{\pi}{2}} \int_{-\pi}^{\pi} \lambda(\theta) sin\theta d\phi \, d\theta}, \tag{5.5}$$

where $\lambda(\theta)$ is the function of θ. X'_{ijkl} is the transformed tensor from the local to global coordinate systems. X'_{ijkl} is defined in Eq. (5.6).

$$X'_{ijkl} = t_{ip}t_{jq}t_{kr}t_{ls}X_{pqrs}$$

$$, \text{ where } \boldsymbol{t} = \begin{bmatrix} \cos\theta & -\sin\theta & 0 \\ \sin\theta\cos\phi & \cos\theta\cos\phi & -\sin\phi \\ \sin\theta\sin\phi & \cos\theta\sin\phi & \cos\phi \end{bmatrix}, \tag{5.6}$$

Here, ϕ and θ are the azimuthal and polar angles denoted in Figure 5.5.

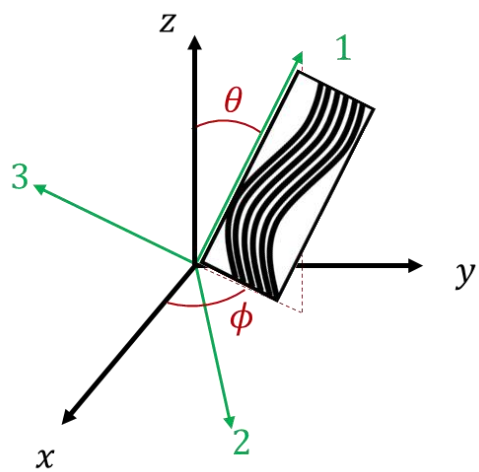

Figure 5.5. Defining the angles of fiber bundles' orientation

To express the random orientation of the fiber bundles, $\lambda(\theta)$ is assumed to follow Eq. (5.7).

$$\lambda(\theta) = e^{-k\theta^2} \tag{5.7}$$

As k decreases to zero, the fiber bundles are randomly oriented. On the other hand, when the k diverges to an infinite value, fiber bundles become aligned in the x-axis

direction. Thus, the fiber bundles' orientation changes with $\lambda(\theta)$. The manufacturing process naturally makes randomly distributed fiber bundles.

The orientation of fiber bundles and the overlapping between fiber bundles occur due to the high volume fraction during the compression molding process. Since the SMC layer is set to one unit depth, as shown in Figure 5.6, the overlapping parts from the lower layer are considered existent inclusions in the current layer.

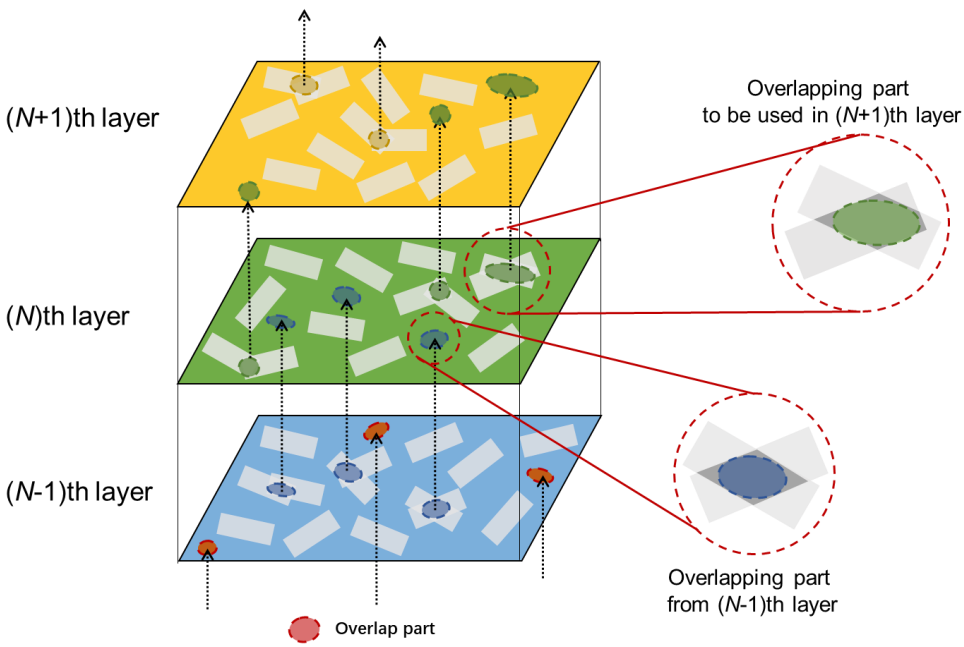

Figure 5.6. Overlapping parts of bundles and mapping to the upper layer

In this paper, the overlapping parts are assumed individual ellipsoidal inclusions. Therefore, the shape of overlapping parts is defined by a diameter and aspect ratio. As shown in Figure 5.7(a), there are many overlapping parts because of the high volume fraction of the SMC composites. Therefore, the realization of an overlapping

part, defined as an arbitrary size, is achieved in the micromechanics model. Because the shape of the overlapping parts is unpredictable, the aspect ratio is assumed to follow the normal distribution, as shown in Figure 5.7(b). The SMC layer modeling uses the multi-site (MS) MT model because the overlapping parts are considered ellipsoidal inclusions with different sizes.

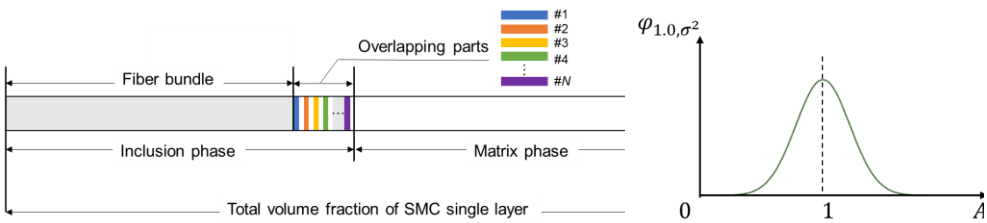

(a) (b)

Figure 5.7. (a) The contents of SMC composites (b) the normal distribution in terms of aspect ratio (AR) for overlapping parts

A suitable volume fraction of the overlapping phases should be determined for the MS MT modeling. The 20 trials with a 10% overlapping volume fraction of the MS-MT model are computed for the elastic modulus. The 20 trial simulations use the parameters in the simulation. The results are then compared with that of Görthofer et al. [22]. As shown in Figure 5.8, when the overlapping phases are insufficient, the calculated modulus is slightly larger than the value in the literature. Moreover, the variance of modulus appears to be gradually converged as the number of overlapping phases increases. Given that a large number of phases lead to tremendous computational time, the number of overlapping phases is set to five, which satisfies both validity and computational efficiency.

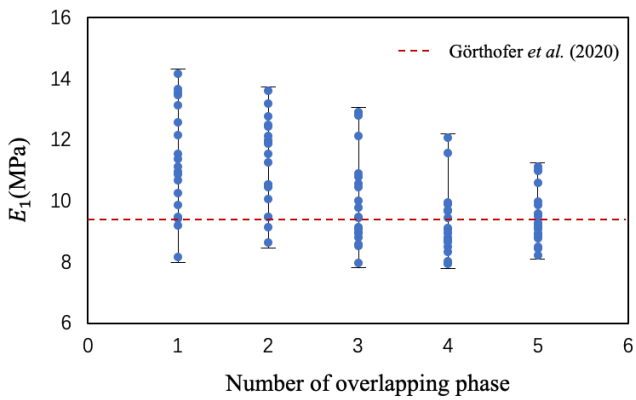

Figure 5.8. Effect of the number of overlapping phases on the effective elastic modulus

5.1.3 Third homogenization: Combining SMC layers using ROM

Finally, the effective properties of the SMC composites are obtained through the Rule of the mixtures (ROM) with virtual layer-by-layer laminations. The homogenized unit SMC layers are laminated into an SMC solid composite. Depending on the preset variables, SMC layers have different homogenized properties calculated in the second homogenization. The effective stiffness of SMC composites is expressed with the homogenized unit layers' stiffnesses, as follows:

$$\boldsymbol{C}^{SMC} = \sum_{i}^{N_{layer}} \frac{\boldsymbol{C}_i^{layer}}{N_{layer}} \tag{5.8}$$

where N_{layer} is the total number of layers. In Eq.(5.8), because the layers constituting the SMC composite are assumed to have the same thickness, the volume

fraction of each layer is $1/N_{layer}$. As a result, the average value of layers' effective stiffness is the effective stiffness of the SMC composites.

The multi-step homogenization for SMC composites is summarized in Figure 5.9. The OS and MS models of the MT method are utilized on the fiber bundle and SMC layer, respectively. And then, the Rule of Mixtures (ROM) is applied to calculate the effective stiffness of SMC composites. This algorithm starts from the strain increment of SMC composites. The SMC composites' strain is divided into phases of matrix and fiber bundles. Furthermore, the strain of fiber bundles is once more separated into the matrix and fiber phases. The first homogenization is conducted based on the material properties of fiber and matrix. The effective stiffness and stress of the fiber bundle with wavy fibers are transferred to the second homogenization. The effective stiffness of the SMC layer is constructed based on the orientation averaging tensor owing to non-uniformly distributed fiber bundles. During the second homogenization, overlapping parts are simultaneously considered by assuming ellipsoidal inclusions. The final step is to obtain the effective stiffness of SMC composites through ROM. The simulations at each stage are concurrently performed because ductile damage plasticity of the matrix is applied to the matrix phase. As an input, the strain increment of SMC composites is entered into this algorithm. Through the multi-step homogenization, the stress increment of SMC composites is calculated as output.

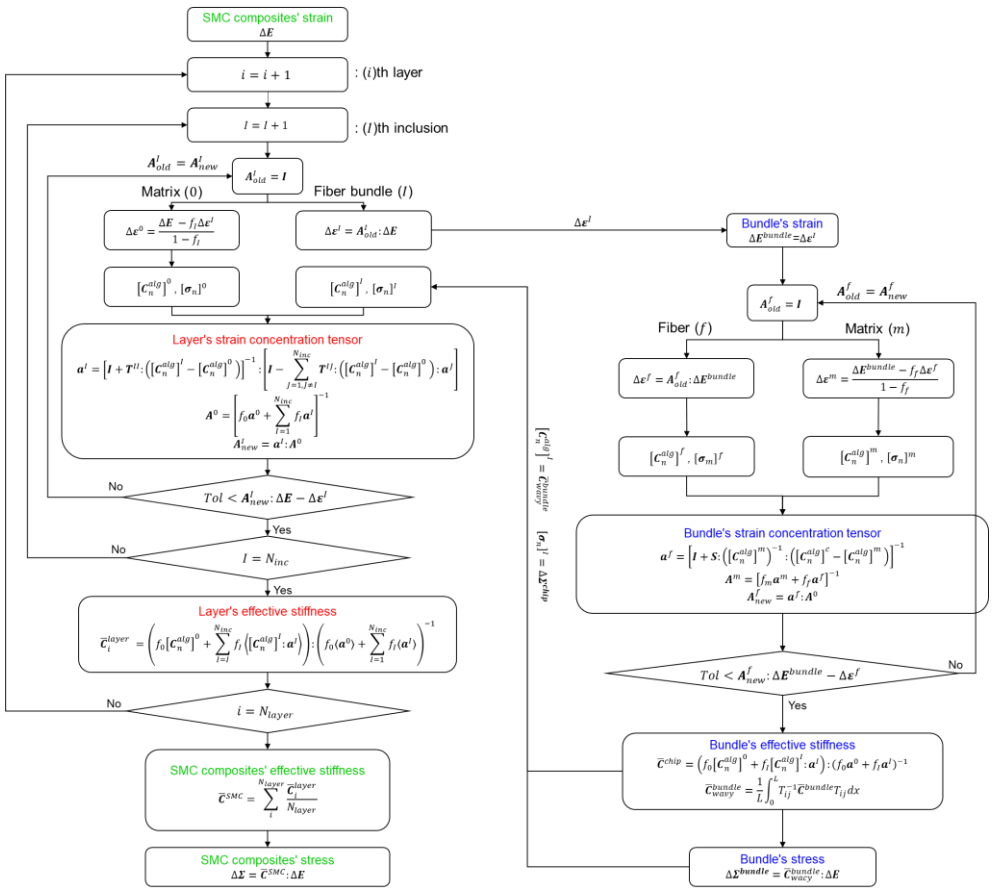

Figure 5.9. Flowchart of multi-step homogenization

5.2 Numerical Simulation Results and Discussion

5.2.1 Model Validation with the literature

The proposed hierarchical micromechanics model is validated based on the results from the literature. Görthofer et al. developed a rapid microstructure generator of SMC composites through closure approximations for the fiber orientation tensor [22]. They utilized E-glass fiber and unsaturated polyester polyurethane hybrid (UPPH) resin for fiber bundles. The material properties are summarized in Table 5.1.

Table 5.1. Material parameters of fiber bundles [103]

	E-glass fibers	UPPH matrix
Young's Modulus (GPa)	72	3.4
Shear Modulus (GPa)	29.51	1.23
Poisson ratio	0.22	0.385

They used numerical full-field homogenization of a representative fiber bundle. Fiber bundles consisting of approximately 225 aligned continuous fibers with a diameter of approximately 13.5 μm are cut to a 25.4mm length. A fiber volume fraction within a fiber bundle is set to 50%. The comparison of elastic properties, with "L" standing for longitudinal and "T" for transverse direction, is summarized in Table 5.2.

Table 5.2. Results comparison of fiber bundles

	Görthofer [22]	MT method
E_L (GPa)	37.73	38.75
E_T (GPa)	10.33	10.61
G_L (GPa)	3.58	4.87
G_T (GPa)	3.64	4.87
v_L	0.477	0.489
v_T	0.292	0.318

All the material properties reasonably match with results from the literature. And then, the elastic properties of SMC composites are evaluated and also compared with the literature. Görthofer et al. constructed the SMC model with a fiber bundle [22]. The size of fiber bundles is designed 50mm×5mm and distributed in 250mm×250mm plates with seven layers. The orientation tensor is determined through μ-CT (Computed Tomography) scans and image processing. The resulting effective orthotropic engineering properties are collected in Table 5.3.

Table 5.3. Comparison of effective elastic properties of SMC composites for the proposed method and literature (unit: GPa).

	Görthofer [22]	Trauth [36]	Kehrer [103]	MT model
E_x	9.42	10.96 ± 0.3	10.92 ± 0.6	9.88 ± 0.5
E_y	8.21	9.25 ± 1.0	8.28 ± 0.5	7.46 ± 0.6
E_z	6.19			7.46 ± 0.6
G_{yz}	1.95			3.02 ± 0.5
G_{xz}	1.96			3.02 ± 0.5
G_{xy}	3.11			3.43 ± 0.4
v_{yz}	0.398			0.398 ± 0.1
v_{xz}	0.368			0.385 ± 0.1
v_{xy}	0.342			0.385 ± 0.1

In the proposed model, for imitating the orientation tensor in the literature, fiber bundles are distributed in a matrix with an orientation variable k=0.32. The number of overlapping types is set to five (six types of inclusions, including SMC bundles) with a 10% volume ratio in the total fiber volume. With the 50% bundles' volume fraction in each layer, the fiber volume fraction of 25% is achieved in this comparison. The variance of the material properties is obtained out of ten trials with the randomness of the waviness (std=1). The proposed method is compared with experiments and the literature with high accuracy, demonstrating the proposed

method's validity. The slight difference may be attributed to waviness and orientation effects that cannot coincide precisely with the experiments and the literature.

5.2.2 Effect of waviness and orientation

The manufacturing-dependent fibers' waviness and bundles' orientation greatly influence on elastic properties of the SMC composites. In this section, the effect of fibers' waviness within bundles is investigated through a case study. For micromechanics modeling, the material properties of constituents in Table 5.1 are assumed, and a monotonic loading is applied in the longitudinal direction. Wavy fibers are set as explained in Chapter 5.1 and classified into three cases. The stress-strain responses of fiber bundles are summarized in Figure 5.10(a). The results show that the existence of waviness reduces mechanical properties.

(a)

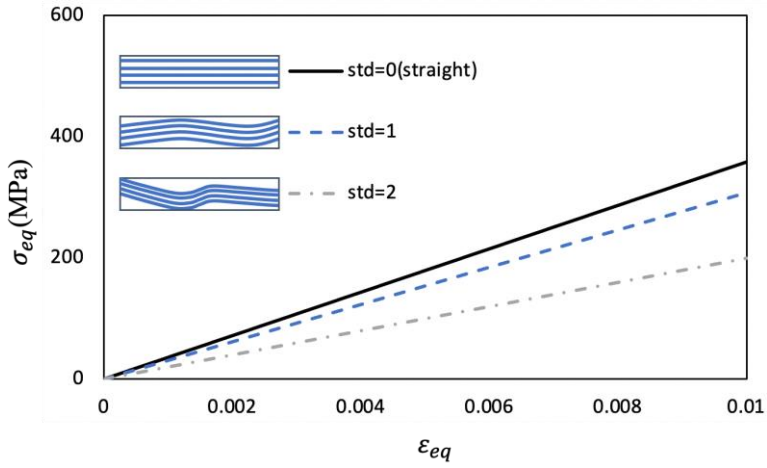

(b)

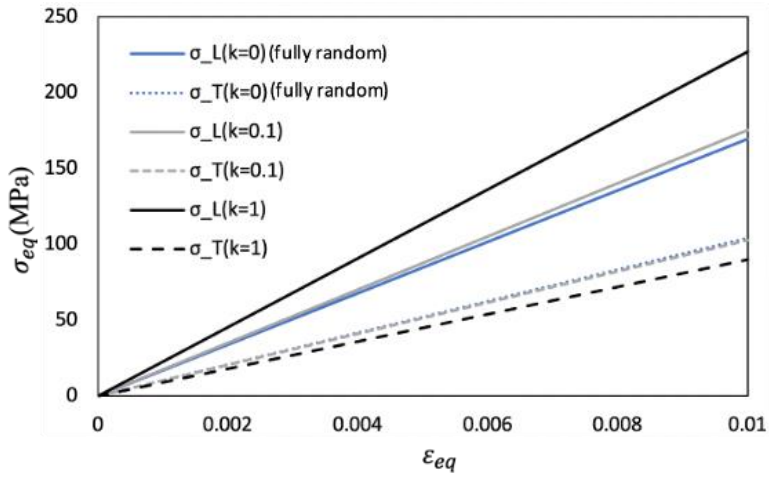

Figure 5.10. The stress-strain curves (a) the influence of the waviness on the SMC bundle and (b) the influence of the orientation on SMC composites

Next, with the increment of the orientation variable k, the longitudinal and transverse stress-strain behavior of the SMC composites are plotted in Figure 5.10(b). The anisotropy of SMC composites is expressed by $\lambda(\theta)$ that is a function of k. The schematic tendency of anisotropy is depicted in Figure 5.11. The behavior in the longitudinal direction becomes stiffer as fiber bundles are aligned to the corresponding direction. When fiber bundles are randomly distributed, the elastic behavior along the x and y directions becomes similar. The parametric study demonstrates that waviness and orientation are critical parameters determining the elastic behavior of both fiber bundles and SMC composites. Further study is conducted by calculating the nonlinear behavior of SMC composites under cyclic loading.

Figure 5.11. The change of bundle orientation with an increment of $\boldsymbol{k}$

5.2.3 The SMC micromechanics model under cyclic loading

In this section, the hierarchical micromechanics model is conducted to obtain the nonlinear behavior of the SMC composites under cyclic loading. The cyclic loading condition is applied to the x-axis, as shown in Figure 5.12. The strain is cyclic in the interval [-0.04, 0.04]. The amplitude of strain is prescribed so that it reaches a plastic regime for nonlinear behavior.

(a)

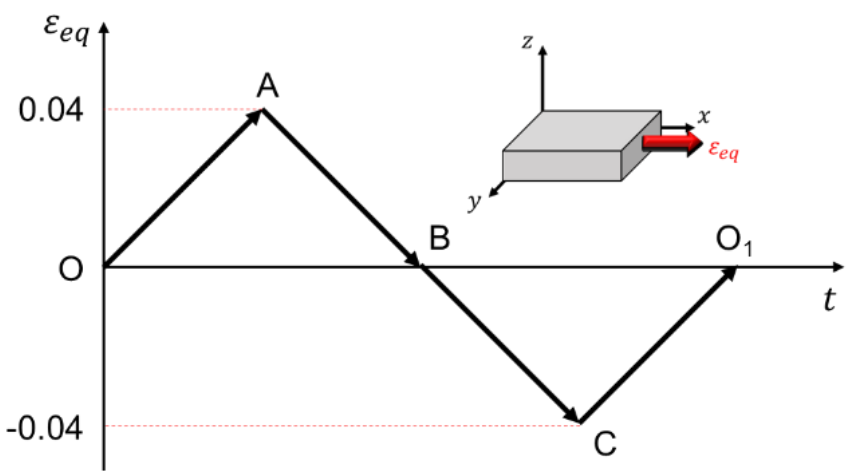

(b)

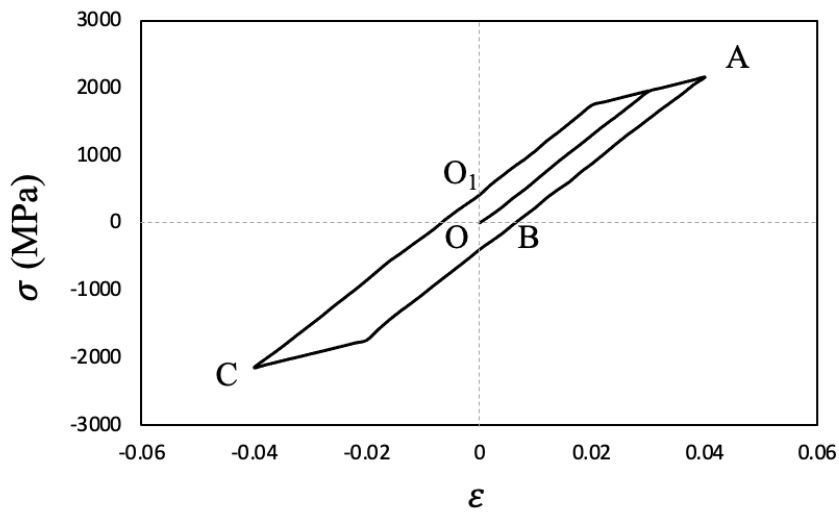

Figure 5.12. Cyclic loading condition and the response of SMC composites: (a) Cyclic loading condition (b) cyclic stress-strain curve

During the OA loading process, the continuous increment of strain causes plasticity with ductile damage. Once the strain arrives at the positive maximum loading point A, the loading strain begins to decrease until the negative maximum loading point C linearly. The response of SMC composites follows the elastic properties until reaching the plastic regime. After that, a hardening slope with ductile damage appears. As a result, unrecoverable plastic strain is generated in the compressive loading. In this simulation, CF/PA6 SMC composites are modeled. The material parameters are referred from the literature [104, 105]

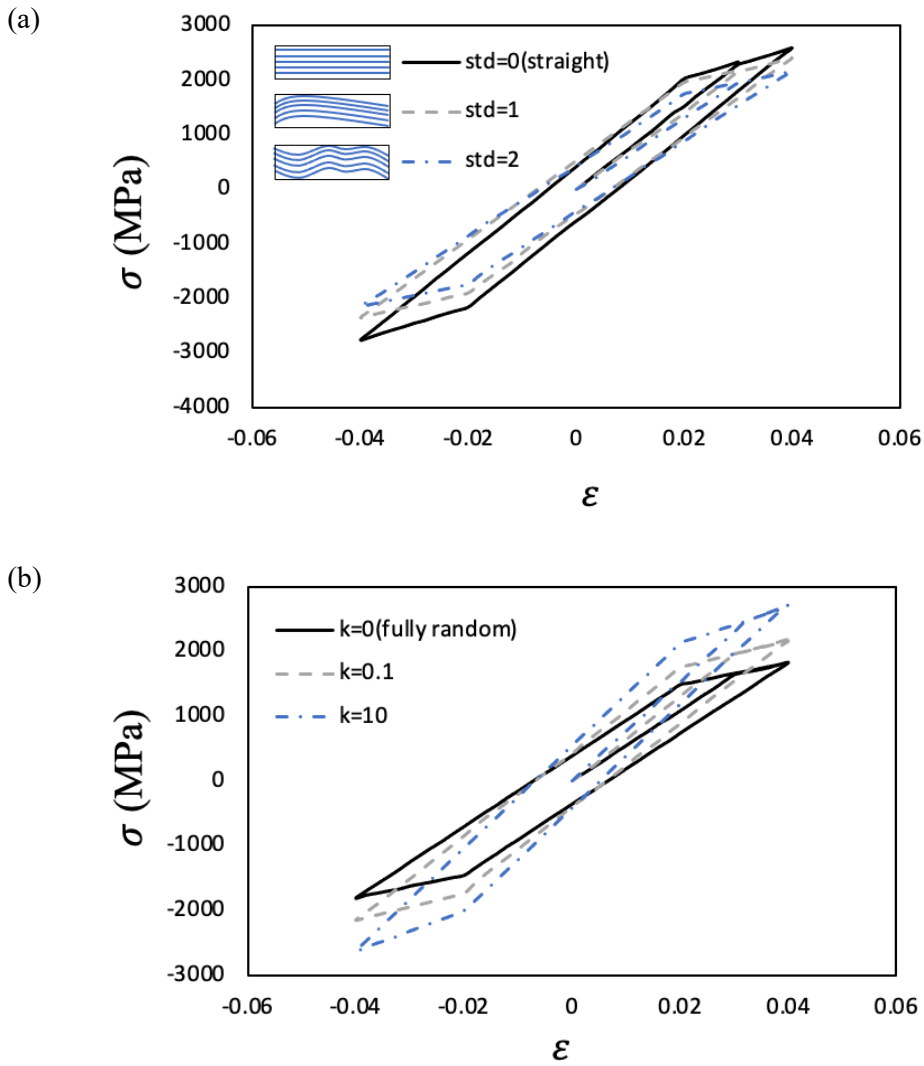

Figure 5.13. Cyclic stress-strain responses (a) waviness (b) orientation distribution

Figure 5.13(a) indicates the effect of waviness on the cyclic stress-strain responses of SMC composites. The volume fraction of fiber and orientation variable k are prescribed as 20% and 0.1, respectively. The fiber bundles with three different kinds of waviness are generated through the calculation. Figure 5.13(a) shows that the

waviness negatively influences both elastic and damage-plastic regimes. Next, Figure 5.13(b) shows that the random distribution with k=0 decreases the material properties not only elastic but also damage-plastic regime. All the models have wavy fibers in the fiber bundles with std=2. Since the aligned fibers to the loading direction provide enormous elastic and plastic, the randomly distributed fiber bundles lead SMC composites to diminish the performance along the loading direction.

Chapter 6. Conclusion

6.1 Summary

In the dissertation, novel multiscale modeling and analysis were presented to understand the mechanical behavior of SMC composites. Mechanical modulus and strength are investigated and further validated with the experimental results.

First, the homogenization methods for composite materials having heterogeneous microstructures were introduced in Chapter 2. Homogenization methods mainly dealt with FE-based direct numerical simulation (DNS) and Mori-Tanaka (MT) method as mean-field homogenization (MFH). The types and features of boundary conditions for DNS were covered. As a result, microstructure representative volume element (RVE) under periodic boundary condition (PBC) showed a good agreement with the experimental results even in small size RVE. Next, MT homogenization is implemented for efficient analysis. The interactive method for global concentration tensor was introduced for nonlinear analysis. It allowed the calculation of effective properties through the interaction between different inclusions. The shape of inclusion was expressed as Eshelby tensor, and isotropization of the tangent modulus when calculating Eshelby's solution was implemented to avoid over-estimating the mechanical properties of composite materials. J_2 plasticity and Lemaitre-Chaboche ductile damage models were combined to predict the ductile damage behavior of the epoxy matrix. These highly nonlinear constitutive modeling schemes were integrated into an incremental Mori-Tanaka (MT) micromechanics framework. The ductile

damage plasticity MT model was reasonably verified by comparing it with the FE-based DNS model in predicting the effective stress-strain behavior. Both DNS and MT models gave rise to higher reinforcing effects on the composite by increasing the volume fraction. Salient softening behavior was observed at a relatively lower volume fraction.

Next, a novel multiscale modeling method for SMC composites is proposed using micro-CT image processing procedures and a novel bundle packing reconstruction algorithm. The dispersion and direction as well as the shape of fiber bundles were determined by micro-CT image processing. Linear static finite element analysis was conducted based on the reconstructed models. Different strain measurement techniques were adopted when predicting the SMC composites' elastic modulus and successfully validated the prediction against the experimental results. The effect of the number of layers in the predictions of strength and modulus of actual specimens was identified, and the comparison was successfully conducted with experimental results measured differently: crosshead-based and DIC-based. Furthermore, the prediction of SMC composites' strength and modulus through static FE simulations was investigated.

Based on the reconstructed SMC mesostructure model, a multiscale failure and damage analysis methodology was presented. The reconstructed model efficiently considered the inherent characteristics of SMC composites. The elastic modulus and strength were evaluated depending on the statistical indicators representing the fiber bundle's orientation and dispersion. Because the mechanical performance was highly related to the orientation indicator, the analytical expression between orientation and

mechanical properties was constructed. According to the dispersion of fiber bundles, the degree of scattering in modulus and strength is changed simultaneously. Although highly clumped dispersion decreased the strength of SMC composites, the modulus maintains a consistent value. As a result, it was revealed that the influence of dispersion was only related to strength property. The validation for the reconstruction SMC RVE was well conducted by comparing the stress-strain curve with the tensile experimental result. Moreover, reasonable verification for material constitutive models was also achieved by investigating the damage patterns with SEM images.

Finally, a novel multi-step homogenization method for SMC composites was developed by considering manufacturing-induced defects. Mainly, fibers' waviness and bundles' orientation were defined in the micromechanics model through a statistical formulation. The influence of these parameters on the elastic and nonlinear behavior of SMC composites was investigated through the parametric study. Moreover, the proposed method was successfully validated against the literature.

6.2 Contributions of the Present Work

The major contributions of the present dissertation can be summarized as follows:

i. A novel stochastic reconstruction algorithm is developed to construct SMC mesostructure, which employs orientation and local volume fraction (dispersion) as statistical indicators. Depending on the

statistical indicators, the reconstructed SMC mesostructure shows different geometry and different mechanical behavior. Most of all, deviations from experiments are realized as a function of statistical indicators. Therefore, the mechanical behavior of SMC composites including elastic modulus and strength is predictable using the computational simulation.

ii. Because of the high fiber volume fraction and geometric complexity, both flexible and rigorous conditions have to be applied in the reconstruction algorithm. The solution is to realize the overlapping between the fiber bundles which can consider the undulation of the bundles laid on the upper side. Moreover, it can allow high-dense inclusion in the designed space, which is suitable for SMC composites.

iii. Micro CT-image processing is presented to characterize the microstructure of SMC composite. Fiber orientation and dispersion are determined through captured CT images, which are employed as statistical indicators in the reconstruction algorithm. Average tensors are replaced with the direct probability density function (PDF) to express more sophisticated distributions.

iv. Depending on the number of layers of SMC composites, modulus and strength are varied because of the capacity of load transfer between the adjacent layers. It implies that the parts with thinner layers can expect higher mechanical performance. Moreover, the methodology of

strength prediction in linear static analysis is presented by calculating the volume-averaging scheme in the matrix region.

v. A three-dimensional (3D) multiscale analysis is conducted by bridging between micro-meso-macroscopic features. Nonlinear analysis for SMC composites is conducted to predict both elastic modulus and strength. Through this methodology, major failure modes observed in tensile testing are also expressed in the computational simulation.

vi. Because SMC composites can be involved in chopped fiber-reinforced composites, this method can extend its ability to other short-fiber reinforced composites in terms of considering orientation and dispersion.

vii. Three-step homogenizations are performed to bridge the features in each length scale. At the micro-scale, manufacturing-induced defects are considered in the RVE models in terms of waviness. It incurs a significant decline in the mechanical modulus of the fiber bundle. Adopting overlapping when modeling the mesostructure of SMC reduces the variance of outcomes, which is led to good agreement with the experimental values. Finally, nonlinear analysis is conducted with low-computing power.

As a result, the present dissertation successfully suggests multiscale analysis for SMC composite materials. SMC modulus and strength are evaluated based on the material constitutive models and mesostructure. Nonlinear behavior is also

investigated with both FE and MT. Its validity is demonstrated by comparison with experimental results.

6.3 Limitation and Future Work

In addition to the present work, there are a few challenging further works as follows:

i. Compression molding simulation should be accompanied to determine a correlation between molding conditions and the placement of fiber bundles. As a purpose of design, manufacturing conditions will be changed.

ii. Mapping features from the mesostructure to the macroscale part with complex geometry is required to develop the structural simulation. In the automotive industry, SMC composites are applied to front and rear panels as well as battery cases.

iii. For large SMC parts, multiple initial charges are utilized and create weld lines during the compression molding process. It is among the most detrimental defects. Although many studies have been reported on short-fiber composite, bundle-based weld lines are still unclear.

iv. Process-structure-property relationship can be defined when the above future works are addressed. Eventually, an efficient design process can be achieved using virtual models. Based on the accumulated data from

the simulation, artificial intelligence is also adapted to the design problem.

Appendix A

Progressive Damage Model for Mori-Tanaka Method

A.1 Ductile Damage Plasticity Model

All state variables such as stress, strain, stiffness, etc. are for the ductile matrix. The strain components of the material can be divided into elastic and plastic parts,

$$\boldsymbol{\varepsilon} = \boldsymbol{\varepsilon}^e + \boldsymbol{\varepsilon}^p, \tag{A.1}$$

where $\boldsymbol{\varepsilon}$ denotes the total strain tensor and superscripts "e" and "p" indicate the elastic and plastic parts, respectively. Then, by Hooke's law and Eq. (A.1), the stress-strain relation is expressed as

$$\boldsymbol{\sigma} = \boldsymbol{C}:\boldsymbol{\varepsilon}^e = \boldsymbol{C}:(\boldsymbol{\varepsilon} - \boldsymbol{\varepsilon}^p), \tag{A.2}$$

where $\boldsymbol{C}$ is the fourth-order elasticity tensor. For an isotropic linear elastic material, $\boldsymbol{C}$ is expressed as index notation,

$$C_{ijkl} = \frac{E}{2(1+\nu)}\left(\delta_{il}\delta_{jk} + \delta_{ik}\delta_{jl}\right) + \frac{\nu E}{(1+\nu)(1-2\nu)}\delta_{ij}\delta_{kl}, \tag{A.3}$$

where δ_{ij} is the Kronecker delta; and E and ν are Young's modulus and Poisson ratio, respectively. An internal variable D represents the damage state in the matrix. Any solution variable in a damaged state is denoted by $(\cdot)$ as

$$(\cdot) = (1-D)(\bar{\cdot}), \text{where } (0 \le D < 1). \tag{A.4}$$

For an elastoplastic material that obeys J_2 flow, the von Mises yield function, ϕ is represented as

$$\phi(\bar{\sigma}_e, R(p)) = \bar{\sigma}_e - R(p) - \sigma_{y0}, \tag{A.5}$$

where σ_e is the effective stress, σ_{y0} is the initial yield stress, $R(p)$ is the hardening function, and p is the effective plastic strain. They are defined as follows:

$$\sigma_e = \sqrt{\frac{3}{2}\bar{\boldsymbol{s}}:\bar{\boldsymbol{s}}} \quad \text{, where } \bar{\boldsymbol{s}} = \bar{\boldsymbol{\sigma}} - \frac{1}{3}tr(\bar{\boldsymbol{\sigma}})$$
$$R(p) = kp^m \quad \text{, where } p = \frac{r}{1-D} \tag{A.6}$$

Here, k and m are parameters associated with isotropic hardening in the form of power laws. $\boldsymbol{s}$ is the deviatoric stress. In this paper, isotropic hardening is only considered because the primary interest is the expansion and contraction behavior of the yield surface during plastic deformation under monotonic loading. If $\phi < 0$, the behavior remains elastic. On the other hand, if $\phi > 0$, then $\dot{p}$ is positive. the plastic strain tensor increment obeys the normal plastic flow, which is summarized by

$$\dot{\varepsilon}^p = \dot{p}\boldsymbol{N} \quad \text{, where } \boldsymbol{N} = \frac{\partial\phi}{\partial\bar{\boldsymbol{\sigma}}} = \frac{3}{2}\frac{\bar{\boldsymbol{s}}}{\bar{\sigma}_e}, \ \dot{p} = \sqrt{\frac{3}{2}\dot{\varepsilon}^p:\dot{\varepsilon}^p} \tag{A.7}$$

where $\boldsymbol{N}$ is the normal vector to the yield surface in the effective stress space. In this formulation, the internal variable p stands for the accumulated plastic strain. In a damaged state, the constitutive relationship is expressed as:

$$\boldsymbol{\sigma} = (1-D)\boldsymbol{C}:(\boldsymbol{\varepsilon} - \boldsymbol{\varepsilon}^p). \tag{A.8}$$

The evolution of the damage is associated with $\dot{p}$ in the Lemaitre-Chaboche model.

$$\dot{D} = \begin{cases} 0 & if\ p \le p_c \\ \left(\frac{\mathrm{Y}}{\mathrm{S}_0}\right)^s \dot{p} & if\ p > p_c \end{cases} \tag{A.9}$$

In this expression, p_c is a plastic threshold for the evolution of damage prescribed as zero in this paper. In other words, the onset of damage occurs when plastic deformation is initiated. The damage variables are defined as follows,

$$y = \left(\frac{Y}{S_0}\right)^s$$

$$Y = \frac{1}{2E}\left(\frac{\bar{\sigma}_e}{1-D}\right)^2 R_v \tag{A.10}$$

$$R_v = \frac{2}{3}(1+\nu) + 3(1-2\nu)\left[\frac{\bar{\sigma}_H}{\bar{\sigma}_e}\right]^2 \quad , \bar{\sigma}_H = \frac{\bar{\sigma}_{kk}}{3},$$

where S_0 and s are material parameters and $\bar{\sigma}_H$ is the hydrostatic pressure. This section derives an iterative stress update algorithm for the matrix phase used in both elastic and plastic regimes. The stress update is related to hardening and ductile damage. [98, 106].

A.2 Algorithm Tangent Operator for Mori-Tanaka Method

All variables with subscript "$(\cdot)_{n+1}$" are computed at the current time increment. The algorithmic tangent operator relates the increments of stress and strain as

$$\delta\hat{\boldsymbol{\sigma}}_{n+1} = \hat{\boldsymbol{C}}^{alg} : \delta\boldsymbol{\varepsilon}_{n+1} \tag{A.11}$$

In the general framework for $\hat{\boldsymbol{C}}^{alg}$, the derivation is proposed by Doghri [107]. In this paper, we summarize the important formulations leading to the effective algorithmic tangent operator $\hat{\boldsymbol{C}}^{alg}$. This can be expressed as follows:

$$\hat{\boldsymbol{C}}^{alg} = \boldsymbol{C}^{el} - (2G)^2 \frac{\Delta p}{1+3/2\,g} \frac{\partial^2\phi}{\partial\hat{\boldsymbol{\sigma}}\partial\hat{\boldsymbol{\sigma}}} - \frac{2}{3}\hat{\boldsymbol{N}}\otimes\left(2G\hat{\boldsymbol{N}}\right) + \left(\frac{2}{3}\frac{dR}{dr}\hat{\boldsymbol{N}}\right)\otimes\frac{\boldsymbol{n}^{alg}}{h^{alg}} \tag{A.12}$$

where G denotes the material shear modulus and the operator "$\otimes$" designates the tensor product. The parameter g and tensor $\frac{\partial^2\phi}{\partial\hat{\boldsymbol{\sigma}}\partial\hat{\boldsymbol{\sigma}}}$ are given by:

$$g = \frac{2G\Delta p}{J_2(\widehat{\boldsymbol{\sigma}})}$$

$$\frac{\partial^2 \phi}{\partial \widehat{\boldsymbol{\sigma}} \partial \widehat{\boldsymbol{\sigma}}} = \frac{1}{J_2(\widehat{\boldsymbol{\sigma}})}\left(\frac{3}{2}\boldsymbol{I}^{dev} - \widehat{\boldsymbol{N}} \otimes \widehat{\boldsymbol{N}}\right) \tag{A.13}$$

Here, $\boldsymbol{I}^{dev}$ the deviatoric part of the fourth-order symmetric identity tensor. In Eq. (A.12), the tensorial quantity $\boldsymbol{n}^{alg}$ yields:

$$\boldsymbol{n}^{alg} = \left[(1-D) - y\Delta p + 2G(\Delta p)^2 \frac{\partial y}{\partial \widehat{\boldsymbol{s}}} : \widehat{\boldsymbol{N}}\right]\left(2G\widehat{\boldsymbol{N}}\right)$$

$$-3G(\Delta p)^2 \left[\boldsymbol{C}^{el} - (2G)^2 \frac{\Delta p}{\left[1 + \left(\frac{3}{2}\right) g\right]} \frac{\partial^2 \phi}{\partial \widehat{\boldsymbol{\sigma}} \partial \widehat{\boldsymbol{\sigma}}}\right] : \frac{\partial y}{\partial \widehat{\boldsymbol{\sigma}}} \tag{A.14}$$

The parameter h^{alg} is expressed as follows:

$$h^{alg} = 3G + \left[(1-D) - y\Delta p + 2G(\Delta p)^2 \frac{\partial y}{\partial \widehat{\boldsymbol{s}}} : \widehat{\boldsymbol{N}}\right]\frac{dR}{dr} \tag{A.15}$$

Differentiation of the damage model *y* for the effective stress $\widehat{\boldsymbol{\sigma}}$ and deviatoric stress $\widehat{\boldsymbol{s}}$ in Eq. (A.14) and (A.15) are given by:

$$\frac{\partial y}{\partial \widehat{\boldsymbol{\sigma}}} = \frac{\partial y}{\partial Y} : \frac{\partial Y}{\partial \widehat{\boldsymbol{\sigma}}}$$

$$= \left(s\left(\frac{1}{S_0}\right)^s Y^{s-1}\right)\left[\frac{1}{2E(1-D)^2}\left(2(1+\nu_m)\boldsymbol{I}^{dev}\widehat{\boldsymbol{\sigma}}^{dev} + \frac{2}{3}\sigma_H(1-2\nu_m)\boldsymbol{I}^{vol}\right)\right] \tag{A.16}$$

, where $\boldsymbol{I}^{vol} = [1 \quad 1 \quad 1 \quad 0 \quad 0 \quad 0]^T$

$$\frac{\partial y}{\partial \widehat{\boldsymbol{s}}} = \frac{\partial y}{\partial \widehat{Y}} : \frac{\partial \widehat{Y}}{\partial \widehat{\boldsymbol{s}}} = \left(s\left(\frac{1}{S_0}\right)^s Y^{s-1}\right)\left[\frac{1}{2E(1-D)^2}\left(2(1+\nu_m)\widehat{\boldsymbol{\sigma}}^{dev}\right)\right]$$

Taking variation of $\sigma = (1-\mathrm{D})\hat{\sigma}$, we obtain the relationship

$$\delta\boldsymbol{\sigma} = (1-D)\delta\widehat{\boldsymbol{\sigma}} - \widehat{\boldsymbol{\sigma}}\delta D \tag{A.17}$$

$$\delta D = y\delta p + (\Delta p)\frac{\partial y}{\partial \hat{\boldsymbol{\sigma}}} : \delta \hat{\boldsymbol{\sigma}}$$

After deriving variations of the damage variable D from Eq. (A.17), we can derive the algorithmic tangent operator $\boldsymbol{C}^{\mathrm{alg}}$, such that:

$$\boldsymbol{C}^{alg} = (1-D)\hat{\boldsymbol{C}}^{alg} - \hat{\boldsymbol{\sigma}} \otimes \left\{ (\Delta p)\hat{\boldsymbol{C}}^{alg} : \frac{\partial y}{\partial \hat{\boldsymbol{\sigma}}} + \frac{2}{3} y \hat{\boldsymbol{N}} - \frac{y}{3G}\frac{dR}{dr}\frac{\boldsymbol{n}^{alg}}{h^{alg}} \right\} \tag{A.18}$$

We introduce the mid-point rule at $n+\alpha$ to alleviate the increment size effect and improve the accuracy. The effective consistent(or algorithmic) tangent stiffness is newly calculated as

$$C_{n+\alpha}^{alg} = (1-\alpha)C_n^{alg} + \alpha C_{n+1}^{alg} \tag{A.19}$$

Explicit and implicit integrations correspond to $\alpha = 0$ and $\alpha > 0$, respectively, with special cases: $\alpha = 1$(backward Euler) and $\alpha = 1/2$(mid-point rule). The mid-point rule is utilized for both inclusion and matrix for calculating the algorithmic tangent operator.

A.3 Fully implicit update of interval variables

The J_2 plasticity model with the Lemaitre-Chaboche damage model includes three independent variables $(r_{n+1}, D_{n+1}, \hat{\boldsymbol{\sigma}}_{n+1})$ at $\mathrm{t_{n+1}}$ To solve for the internal state variable at $\mathrm{t_{n+1}}$, the fully implicit radial return mapping method is utilized in this paper.

$$\hat{\boldsymbol{\sigma}}_{n+1} = \boldsymbol{C}^{el} : \left(\boldsymbol{\varepsilon}_n + \Delta\boldsymbol{\varepsilon} - \boldsymbol{\varepsilon}_n^p - \Delta\boldsymbol{\varepsilon}^p\right) = \hat{\boldsymbol{\sigma}}_{n+1} = \hat{\boldsymbol{\sigma}}_{n+1}^{trial} - \boldsymbol{C}^{el} : \Delta\boldsymbol{\varepsilon}^p \tag{A.20}$$

where $\hat{\sigma}_{n+1}^{trial}$ is the equivalent trial stress. The assumption of the trial stress is incorrect when plastic deformation occurs. In this case, we need to find a $\hat{\sigma}_{n+1}$ that

satisfies $\phi = 0$. This process is called as a plastic corrector. Due to $Tr(\Delta\varepsilon^p) = 0$, Eq. (A.20) is converted to the form

$$\hat{\boldsymbol{\sigma}}_{n+1} = \hat{\boldsymbol{\sigma}}_{n+1}^{trial} - 2G\Delta\boldsymbol{\varepsilon}^p \tag{A.21}$$

The main equations for updating the internal variables are summarized as follows.

$$\begin{aligned} &\hat{\boldsymbol{\sigma}}_{n+1} = \hat{\boldsymbol{\sigma}}_{n+1}^{trial} - 2G\Delta\boldsymbol{\varepsilon}^p \qquad where\ \Delta\boldsymbol{\varepsilon}^p = \Delta p\hat{\boldsymbol{N}} \\ &\phi = \hat{\sigma}_e - R(p) - \sigma_{y0} = 0 \\ &\Delta D = y(\hat{\sigma})\Delta p \qquad where\ \Delta p = \frac{1}{(1-D)}\Delta r \end{aligned} \tag{A.22}$$

In Eq. (A.22), equations are rearranged to the following system of nonlinear equations to be simultaneously solved for three unknowns Δr, ΔD and $\hat{\sigma}_e$.

$$\begin{aligned} &f_1 \equiv \hat{\sigma}_e - \hat{\sigma}_e^{trial} + 3G\frac{\Delta r}{1-D} = 0 \\ &f_2 \equiv \hat{\sigma}_e - R(r) - \sigma_{y0} = 0 \\ &f_3 \equiv \Delta D - y(\hat{\sigma})\frac{\Delta r}{1-D} = 0 \end{aligned} \tag{A.23}$$

It is considerably complicated when damage evolution is coupled with plastic deformation because of the increasing number of solution variables. Newton's iterative method is utilized to solve this complex nonlinear system. For each iteration, the corrections obey the equations in Eq. (A.23). Note that solving all three equations simultaneously with Newton's method may create a convergence problem. Therefore, we solve the first two equations (i.e., f_1 and f_2) that are independent of ΔD and these two equations are solved for Δr. Once Δr is found, the remaining unknown parameters ΔD can be calculated. First, a new function f_4 is defined by combining f_1 with f_2.

$$f_4 = \hat{\sigma}_e^{trial} - 3G\frac{\Delta r}{1-D} - R(r) - \sigma_{y0} = 0 \tag{A.24}$$

Which is a nonlinear function of incremental plastic strain Δr. Therefore, it is solved by Newton's iterative method. For this purpose, f_4 is expressed in the Taylor series up to the first-order term

$$\begin{aligned} & f_4 + \frac{\partial f_4}{\partial \Delta r} d\Delta r + \cdots = \\ & \hat{\sigma}_e^{trial} - 3G\frac{\Delta r}{1-D} - kr^m - \sigma_{y0} + \left(-3G\frac{1}{1-D} - kmr^{m-1}\right) d\Delta r = 0 \end{aligned} \tag{A.25}$$

From this formulation, we can obtain Δr through Newton's iteration until satisfying $\phi = 0$ as expressed in Eq. (A.26).

$$\begin{aligned} & d\Delta r = \frac{\hat{\sigma}_e^{trial} - 3G\frac{\Delta r}{1-D} - kr^m - \sigma_{y0}}{-3G\frac{1}{1-D} - kmr^{m-1}} \\ & \Delta r^{(k+1)} = \Delta r^{(k)} + d\Delta r \end{aligned} \tag{A.26}$$

where (k) denotes the number of iterations. After the plastic strain increment, Δr is determined, Δp and ΔD are also determined by the relations in Eq. (A.27).

$$\begin{aligned} & \Delta p = \frac{\Delta r}{1-D} \\ & \Delta D = \frac{y\Delta r}{1-D} \end{aligned} \tag{A.27}$$

Therefore, the algorithmic tangent operator in Eq. (A.18) can be calculated using the updated internal variables. Finally, we can update stresses, damage, and plasticity-related variables at the time t_{n+1} as follows:

$$\begin{aligned} & \hat{\boldsymbol{\sigma}}_{n+1} = \hat{\boldsymbol{\sigma}}_n + \Delta\hat{\boldsymbol{\sigma}}^{(k+1)} \\ & p_{n+1} = p_n + \Delta p^{(k+1)} \end{aligned} \tag{A.28}$$

$$D_{n+1} = D_n + \Delta D^{(k+1)} \Delta D = \frac{y \Delta r}{1 - D}$$

Finally, a computational procedure for the modified Mori-Tanaka scheme is summarized as Pseudocode in Table. A.1. A flow chart for multiscale damage simulation implemented in UMAT of ABAQUS is also depicted in Figure A.1.

Table. A.1. Pseudocode for the modified Mori-Tanaka scheme

Numerical implementation
1. Compute the strain increment in the inclusions : $\Delta\boldsymbol{\varepsilon}^I = \boldsymbol{A}^I : \Delta\boldsymbol{E}$
2. Compute stress and algorithmic moduli of the inclusion: $\left[\boldsymbol{\sigma}_{n+1}, \boldsymbol{C}_{n+1}^{alg}\right]^I$
3. Compute the strain increment in the matrix: $\Delta\boldsymbol{\varepsilon}^0 = \frac{\Delta\boldsymbol{E} - f_I \Delta\boldsymbol{\varepsilon}^I}{1 - f_I}$
4. Compute internal variables in the matrix: $[p_{n+1}, \boldsymbol{D}_{n+1}, \boldsymbol{\sigma}_{n+1}]^0$
5. Update algorithmic moduli in the matrix: $\left[\boldsymbol{C}_{n+1}^{alg}\right]^0$
6. Apply the mid-point rule at the time $t_{n+\alpha}$ to the algorithmic moduli of the matrix: $\left[\boldsymbol{C}_{n+\alpha}^{alg}\right]^0 = \left[(1-\alpha)\boldsymbol{C}_n^{alg} + \alpha\boldsymbol{C}_{n+1}^{alg}\right]^0$
7. Compute the global strain concentration tensor: $\boldsymbol{A}^I = \boldsymbol{a}^I : \boldsymbol{A}^0$
8. Check the compatibility of average strain in the inclusions phase by computing residual: $R = \boldsymbol{A}^I : \Delta\boldsymbol{E} - \Delta\boldsymbol{\varepsilon}^I$
9. If $\lvert R \rvert \leq TOL$, then exit the loop and go to step 11
10. Else: new iteration (go to step 1) using the computed value of the global strain concentration tensor
11. Compute the homogenized tangent properties: $\boldsymbol{C}_{modified}^{MT} = \left(f_0\left[\boldsymbol{C}_{n+\alpha}^{alg}\right]^0 + f_I\left[\boldsymbol{C}_{n+\alpha}^{alg}\right]^I : \boldsymbol{a}^I\right) : \left[f_0\boldsymbol{I} + f_I\left(\boldsymbol{I} + \boldsymbol{H}^I : \left[\boldsymbol{C}_{n+\alpha}^{alg}\right]^I\right) : \boldsymbol{a}^I\right]^{-1}$
12. After convergence, compute the macroscopic stress increment: $\Delta\boldsymbol{\sigma} = \boldsymbol{C}_{modified}^{MT} : \Delta\boldsymbol{E}$

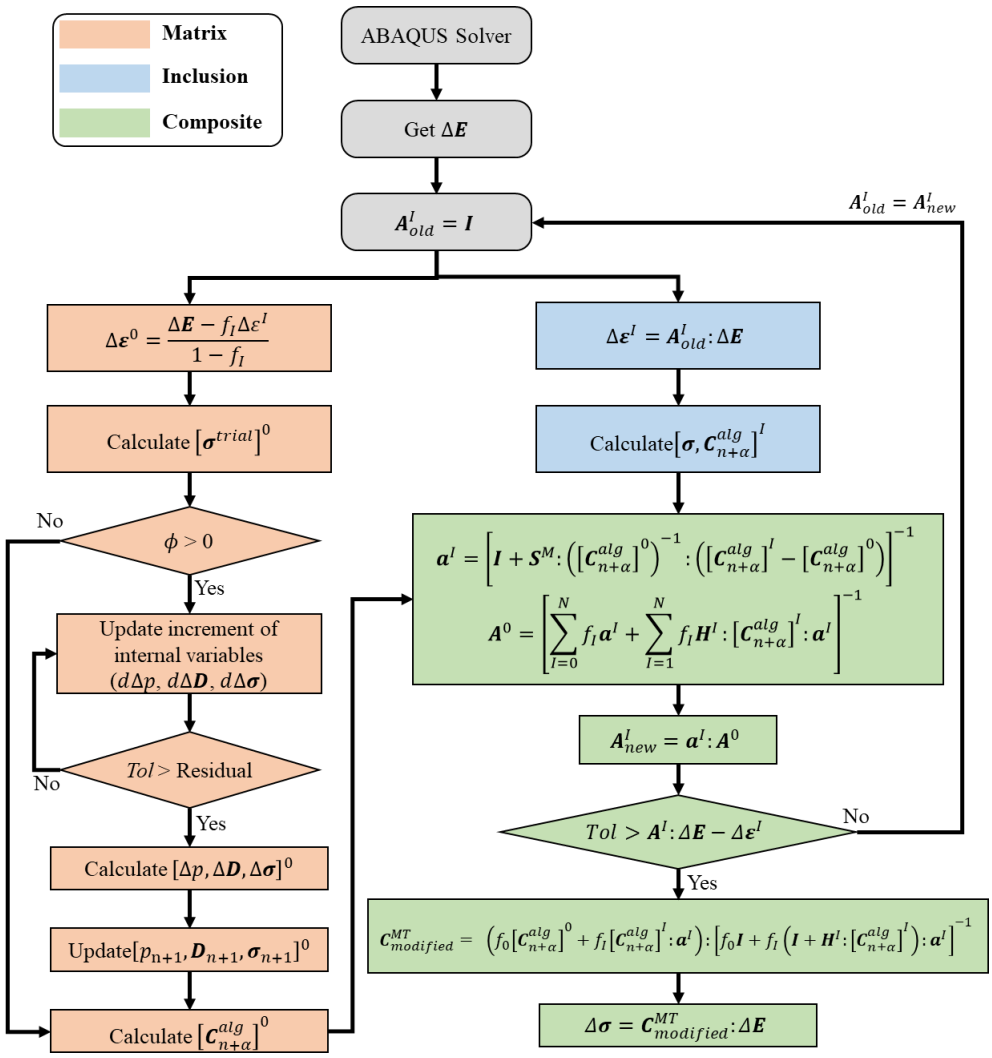

Figure A.1. Flowchart for the modified Mori-Tanaka scheme

Appendix B

Inverse Identification

For material parameter estimation, we apply the numerical-experimental methodology of finite element model updating (FEMU) optimization [108]. Figure B.1 shows the overall algorithmic procedure of the FEMU approach. For example, the reaction force is obtained through displacement-driven analysis. The obtained reaction force data are compared with those from the experimental test. The difference of reaction force data between the simulation and experiment is employed to construct an objective function to be minimized. Depending on the problem sets, other response variables can be used instead of reaction forces. The unconstrained optimization problem of FEMU utilizes the objective function in Eq. (B.1) which consists of mean average error (MAE), root mean square error ($RMSE$), correlation (R) between the reaction force and displacement of simulations.

$$f_{FEMU}(p_k: k = 1, \dots, m) = \sum_{i=1}^{n} \frac{RMSE_i\left(RF^{sim} - RF^{exp}\right) + MAE_i(RF^{sim} - RF^{exp})}{R_i(RF^{sim} - RF^{exp})} \tag{B.1}$$

where p_k is the material property to be identified and n is the number of load or time steps used to increase sensitivity for the optimization problem. The statistical error measures and the correlation used in the objective function are defined as follows,

$$R(A,B) = \frac{\sum_n (A_n - \bar{A})(B_n - \bar{B})}{\sqrt{(\sum_n (A_n - \bar{A})^2)(\sum_n (B_n - \bar{B})^2)}}$$

$$RMSE(A,B) = \sqrt{\frac{\sum_n (A_n - B_n)^2}{n}} \tag{B.2}$$

$$MAE(A,B) = \frac{\sum_n |A_n - B_n|}{n}$$

where A and B indicate that stress or strain data are from either simulation FE analysis or experiment.

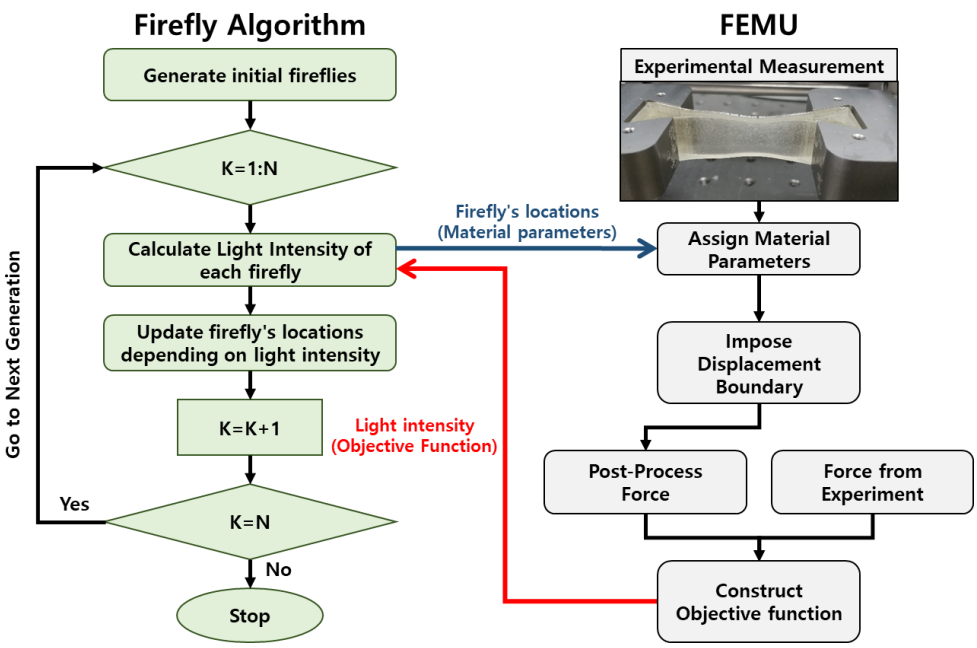

Figure B.1. Algorithm procedure of inverse analysis

The CFA (Chaotic Firefly Algorithm) is selected to search for the optimal material properties since it is efficient in searching for a global optimizer. CFA is one of the

metaheuristic optimization algorithms that mimic the social behavior of fireflies [109].

References

[1] Y. Kim and G. J. Yun, "Effects of microstructure morphology on stress in mechanoluminescent particles: Micro CT image-based 3D finite element analyses," *Composites Part A: Applied Science and Manufacturing,* vol. 114, pp. 338-351, 2018.

[2] Y. Yang, F. Xu, X. Gao, G. Liu, and M. Zhang, "Two failure modes of C/SiC composite under different impact loads," *Composites Part B: Engineering,* vol. 136, pp. 158-167, 2018.

[3] Y. Yang, F. Xu, X. Gao, and G. Liu, "Impact resistance of 2D plain-woven C/SiC composites at high temperature," *Materials & Design,* vol. 90, pp. 635-641, 2016.

[4] X. Zeng, L. P. Brown, A. Endruweit, M. Matveev, and A. C. Long, "Geometrical modelling of 3D woven reinforcements for polymer composites: Prediction of fabric permeability and composite mechanical properties," *Composites Part A: Applied Science and Manufacturing,* vol. 56, pp. 150-160, 2014.

[5] S. Y. Fu, B. Lauke, E. Mäder, C. Y. Yue, and X. Hu, "Tensile properties of short-glass-fiber- and short-carbon-fiber-reinforced polypropylene composites," *Composites Part A: Applied Science and Manufacturing,* vol. 31, no. 10, pp. 1117-1125, 2000.

[6] T. Webbe Kerekes, H. Lim, W. Y. Joe, and G. J. Yun, "Characterization of process–deformation/damage property relationship of fused deposition modeling (FDM) 3D-printed specimens," *Additive Manufacturing,* vol. 25, pp. 532-544, 2019.

[7] H. J. Lim, H. Choi, F.-Y. Zhu, T. W. Kerekes, and G. J. Yun, "Multiscale damage plasticity modeling and inverse characterization for particulate composites," *Mechanics of Materials,* vol. 149, p. 103564, 2020.

[8] H. You, H. Lim, H. Choi, and G. Yun, "Prediction of Viscoelastic Behavior of Particulate Composites by a Time-Domain Homogenization Approach," in *AIAA Scitech 2021 Forum*, 2021, p. 1230.

[9] S. Jeong, H.-J. Lim, F.-Y. Zhu, C. Park, Y. Kim, and G. Yun, "Nano-Micro Multiscale Modeling for Graphene-Reinforced Nanocomposites," in *2018 AIAA/ASCE/AHS/ASC Structures, Structural Dynamics, and Materials Conference*, 2018,

[10] N. Meyer, L. Schöttl, L. Bretz, A. N. Hrymak, and L. Kärger, "Direct Bundle Simulation approach for the compression molding process of Sheet Molding Compound," *Composites Part A: Applied Science and Manufacturing,* vol. 132, p. 105809, 2020.

[11] J. Görthofer *et al.*, "Virtual process chain of sheet molding compound: Development, validation and perspectives," *Composites Part B: Engineering,* vol. 169, pp. 133-147, 2019.

[12] L. M. Abrams and J. M. Castro, "Predicting molding forces during sheet molding compound (SMC) compression molding. I: Model development," *Polymer Composites,* vol. 24, no. 3, pp. 291-303, 2003.

[13] J. D. Eshelby and R. E. Peierls, "The determination of the elastic field of an ellipsoidal inclusion, and related problems," *Proceedings of the Royal Society of London. Series A. Mathematical and Physical Sciences,* vol. 241, no. 1226, pp. 376-396, 1957.

[14] I. Doghri and A. Ouaar, "Homogenization of two-phase elasto-plastic composite materials and structures: Study of tangent operators, cyclic plasticity and numerical algorithms," *International Journal of Solids and Structures,* vol. 40, no. 7, pp. 1681-1712, 2003.

[15] I. Doghri, L. Brassart, L. Adam, and J. S. Gérard, "A second-moment incremental formulation for the mean-field homogenization of elasto-plastic composites," *International Journal of Plasticity,* vol. 27, no. 3, pp. 352-371, 2011.

[16] F. Meraghni and M. L. Benzeggagh, "Micromechanical modelling of matrix degradation in randomly oriented discontinuous-fibre composites," *Composites Science and Technology,* vol. 55, no. 2, pp. 171-186, 1995.

[17] G. P. Carman and K. L. Reifsnider, "Micromechanics of short-fiber composites," *Composites Science and Technology,* vol. 43, no. 2, pp. 137-146, 1992.

[18] J. Fitoussi, G. Guo, and D. Baptiste, "A statistical micromechanical model of anisotropic damage for S.M.C. composites," *Composites Science and Technology,* vol. 58, no. 5, pp. 759-763, 1998.

[19] J. Fitoussi, N. Bourgeois, G. Guo, and D. Baptiste, "Prediction of the anisotropic damaged behavior of composite materials: introduction of multilocal failure criteria in a micro-macro relationship," *Computational Materials Science,* vol. 5, no. 1, pp. 87-100, 1996.

[20] J. Fitoussi, G. Guo, and D. Baptiste, "Determination of a tridimensional failure criterion at the fibre/matrix interface of an organic-matrix/discontinuous-reinforcement composite," *Composites Science and Technology,* vol. 56, no. 7, pp. 755-760, 1996.

[21] D. Anagnostou, G. Chatzigeorgiou, Y. Chemisky, and F. Meraghni, "Hierarchical micromechanical modeling of the viscoelastic behavior coupled to damage in SMC and SMC-hybrid composites," *Composites Part B: Engineering,* vol. 151, pp. 8-24, 2018.

[22] J. Görthofer, M. Schneider, F. Ospald, A. Hrymak, and T. Böhlke, "Computational homogenization of sheet molding compound composites based on high fidelity representative volume elements," *Computational Materials Science,* vol. 174, p. 109456, 2020.

[23] S. Tamboura *et al.*, "Experimental and numerical multi-scale approach for Sheet-Molding-Compound composites fatigue prediction based on fiber-matrix interface cyclic damage," *International Journal of Fatigue,* vol. 135, p. 105526, 2020.

[24] P. Feraboli, T. Cleveland, P. Stickler, and J. Halpin, "Stochastic laminate analogy for simulating the variability in modulus of discontinuous composite materials," *Composites Part A: Applied Science and Manufacturing,* vol. 41, no. 4, pp. 557-570, 2010.

[25] A. Ionita and Y. J. Weitsman, "On the mechanical response of randomly reinforced chopped-fibers composites: Data and model," *Composites Science and Technology,* vol. 66, no. 14, pp. 2566-2579, 2006.

[26] H. J. Lim, H. Choi, M. J. Lee, and G. J. Yun, "An efficient multi-scale model for needle-punched Cf/SiCm composite materials with experimental validation," *Composites Part B: Engineering,* vol. 217, p. 108890, 2021.

[27] H. Lim, H. Choi, M. J. Lee, and G. J. Yun, "Elasto-plastic damage modeling and characterization of 3D needle-punched Cf/SiCm composite materials," *Ceramics International,* vol. 46, no. 10, Part B, pp. 16918-16931, 2020.

[28] J. Yu, C. Zhou, and H. Zhang, "A micro-image based reconstructed finite element model of needle-punched C/C composite," *Composites Science and Technology,* vol. 153, pp. 48-61, 2017.

[29] S. Ghosh, K. Lee, and S. Moorthy, "Multiple scale analysis of heterogeneous elastic structures using homogenization theory and voronoi cell finite element method," *International Journal of Solids and Structures,* vol. 32, no. 1, pp. 27-62, 1995.

[30] Y. Li, Z. Chen, L. Su, W. Chen, X. Jin, and H. Xu, "Stochastic reconstruction and microstructure modeling of SMC chopped fiber composites," *Composite Structures,* vol. 200, pp. 153-164, 2018.

[31] K. Schladitz *et al.*, "Non-destructive characterization of fiber orientation in reinforced SMC as input for simulation based design," *Composite Structures,* vol. 160, pp. 195-203, 2017.

[32] Y. Pan, L. Iorga, and A. A. Pelegri, "Analysis of 3D random chopped fiber reinforced composites using FEM and random sequential adsorption," *Computational Materials Science,* vol. 43, no. 3, pp. 450-461, 2008.

[33] Z. Chen *et al.*, "Multiscale finite element modeling of sheet molding compound (SMC) composite structure based on stochastic mesostructure reconstruction," *Composite Structures,* vol. 188, pp. 25-38, 2018.

[34] Z. Chen *et al.*, "Failure of chopped carbon fiber Sheet Molding Compound (SMC) composites under uniaxial tensile loading: Computational prediction and experimental analysis," *Composites Part A: Applied Science and Manufacturing,* vol. 118, pp. 117-130, 2019.

[35] H. Tang *et al.*, "Computational micromechanics model based failure criteria for chopped carbon fiber sheet molding compound composites," *Composites Science and Technology,* vol. 200, p. 108400, 2020.

[36] A. Trauth, P. Pinter, and K. A. Weidenmann, "Investigation of Quasi-Static and Dynamic Material Properties of a Structural Sheet Molding Compound Combined with Acoustic Emission Damage Analysis," *Journal of Composites Science,* vol. 1, no. 2, p. 18, 2017.

[37] H. J. Lim, H.-i. Choi, and G. J. Yun, "Micro-CT Image-Based Reconstruction Model for Failure Analysis of Sheet Molding Compound (SMC) Composites," in *Proceedings of the American Society for Composites—Thirty-Sixth Technical Conference on Composite Materials*, 2021,

[38] H. J. Lim, H. Choi, and G. J. Yun, "Multiscale failure and damage analysis of sheet molding compound (SMC) composites using Micro-CT image-based reconstruction model," *Composites Part B: Engineering,* vol. 231, p. 109593, 2022.

[39] S. G. Advani and C. L. T. III, "The Use of Tensors to Describe and Predict Fiber Orientation in Short Fiber Composites," *Journal of Rheology,* vol. 31, no. 8, pp. 751-784, 1987.

[40] D. E. Sommer, S. G. Kravchenko, B. R. Denos, A. J. Favaloro, and R. B. Pipes, "Integrative analysis for prediction of process-induced, orientation-dependent tensile properties in a stochastic prepreg platelet molded composite," *Composites Part A: Applied Science and Manufacturing,* vol. 130, p. 105759, 2020.

[41] M. P. Alves, C. A. Cimini Junior, and S. K. Ha, "Fiber waviness and its effect on the mechanical performance of fiber reinforced polymer composites: An enhanced review," *Composites Part A: Applied Science and Manufacturing,* vol. 149, p. 106526, 2021.

[42] P. Kulkarni, K. D. Mali, and S. Singh, "An overview of the formation of fibre waviness and its effect on the mechanical performance of fibre reinforced polymer composites," *Composites Part A: Applied Science and Manufacturing,* vol. 137, p. 106013, 2020.

[43] J. A. Hudson, "Overall properties of heterogeneous material," *Geophysical Journal International,* vol. 107, no. 3, pp. 505-511, 1991.

[44] M. G. D. Geers, V. G. Kouznetsova, and W. A. M. Brekelmans, "Multi-scale computational homogenization: Trends and challenges," *Journal of Computational and Applied Mathematics,* vol. 234, no. 7, pp. 2175-2182, 2010.

[45] F. S. Almeida and A. M. Awruch, "Design optimization of composite laminated structures using genetic algorithms and finite element analysis," *Composite Structures,* vol. 88, no. 3, pp. 443-454, 2009.

[46] T. Kanit, S. Forest, I. Galliet, V. Mounoury, and D. Jeulin, "Determination of the size of the representative volume element for random composites: statistical and numerical approach," *International Journal of Solids and Structures,* vol. 40, no. 13, pp. 3647-3679, 2003.

[47] H.-i. Choi, C. Park, H. J. Lim, and G. J. Yun, "A Nano-Micro–Macro Multiscale Modeling for Carbon Fiber-Reinforced Graphene/Epoxy Nanocomposites," *Multiscale Science and Engineering,* vol. 3, no. 1, pp. 36-50, 2021.

[48] Z. Hashin, "The Elastic Moduli of Heterogeneous Materials," *Journal of Applied Mechanics,* vol. 29, no. 1, pp. 143-150, 1962.

[49] V. Kouznetsova, M. G. D. Geers, and W. A. M. Brekelmans, "Multi-scale constitutive modelling of heterogeneous materials with a gradient-enhanced computational homogenization scheme," *International Journal for Numerical Methods in Engineering,* vol. 54, no. 8, pp. 1235-1260, 2002.

[50] F.-Y. Zhu, S. Jeong, H. J. Lim, and G. J. Yun, "Probabilistic multiscale modeling of 3D randomly oriented and aligned wavy CNT nanocomposites and RVE size determination," *Composite Structures,* vol. 195, pp. 265-275, 2018.

[51] S. Jeong, F. Zhu, H. Lim, Y. Kim, and G. J. Yun, "3D stochastic computational homogenization model for carbon fiber reinforced CNT/epoxy composites with spatially random properties," *Composite Structures,* vol. 207, pp. 858-870, 2019.

[52] H.-I. Choi, F.-Y. Zhu, H. Lim, and G. J. Yun, "Multiscale stochastic computational homogenization of the thermomechanical properties of woven Cf/SiCm composites," *Composites Part B: Engineering,* vol. 177, p. 107375, 2019.

[53] K. Terada, M. Hori, T. Kyoya, and N. Kikuchi, "Simulation of the multi-scale convergence in computational homogenization approaches," *International Journal of Solids and Structures,* vol. 37, no. 16, pp. 2285-2311, 2000.

[54] K. Terada and N. Kikuchi, "A class of general algorithms for multi-scale analyses of heterogeneous media," *Computer Methods in Applied Mechanics and Engineering,* vol. 190, no. 40, pp. 5427-5464, 2001.

[55] W. Voigt, *Theoretische studien über die elasticitätsverhältnisse der krystalle*. Königliche Gesellschaft der Wissenschaften zu Göttingen, 1887.

[56] Z. Hashin and S. Shtrikman, "A variational approach to the theory of the elastic behaviour of multiphase materials," *Journal of the Mechanics and Physics of Solids,* vol. 11, no. 2, pp. 127-140, 1963.

[57] Z. Hashin and S. Shtrikman, "Note on a variational approach to the theory of composite elastic materials," *Journal of the Franklin Institute,* vol. 271, no. 4, pp. 336-341, 1961.

[58] T. Mori and K. Tanaka, "Average stress in matrix and average elastic energy of materials with misfitting inclusions," *Acta Metallurgica,* vol. 21, no. 5, pp. 571-574, 1973.

[59] R. Hill, "A self-consistent mechanics of composite materials," *Journal of the Mechanics and Physics of Solids,* vol. 13, no. 4, pp. 213-222, 1965.

[60] Z. Hashin, "On elastic behaviour of fibre reinforced materials of arbitrary transverse phase geometry," *Journal of the Mechanics and Physics of Solids,* vol. 13, no. 3, pp. 119-134, 1965.

[61] O. Pierard, C. Friebel, and I. Doghri, "Mean-field homogenization of multi-phase thermo-elastic composites: a general framework and its validation," *Composites Science and Technology,* vol. 64, no. 10, pp. 1587-1603, 2004.

[62] M. Paley and J. Aboudi, "Micromechanical analysis of composites by the generalized cells model," *Mechanics of Materials,* vol. 14, no. 2, pp. 127-139, 1992.
[63] S. Hazanov and C. Huet, "Order relationships for boundary conditions effect in heterogeneous bodies smaller than the representative volume," *Journal of the Mechanics and Physics of Solids,* vol. 42, no. 12, pp. 1995-2011, 1994.
[64] C. T. Sun and R. S. Vaidya, "Prediction of composite properties from a representative volume element," *Composites Science and Technology,* vol. 56, no. 2, pp. 171-179, 1996.
[65] H. You, H. J. Lim, and G. J. Yun, "A micromechanics-based time-domain viscoelastic constitutive model for particulate composites: Theory and experimental validation," *Advances in Aircraft and Spacecraft Science,* vol. 9, no. 3, pp. 217-242,
[66] P. Vieville, A. Bonnet, and P. Lipiński, "Modelling effective properties of composite materials using the inclusion concept. General considerations," *Archives of Mechanics,* vol. 58, no. 3, pp. 207-239, 2006.
[67] S. Li, R. A. Sauer, and G. Wang, "The Eshelby Tensors in a Finite Spherical Domain—Part I: Theoretical Formulations," *Journal of Applied Mechanics,* vol. 74, no. 4, pp. 770-783, 2006.
[68] A. Tchalla, W. L. Azoti, Y. Koutsawa, A. Makradi, S. Belouettar, and H. Zahrouni, "Incremental mean-fields micromechanics scheme for non-linear response of ductile damaged composite materials," *Composites Part B: Engineering,* vol. 69, pp. 169-180, 2015.
[69] A. J. Favaloro, B. R. Denos, D. E. Sommer, R. A. Cutting, and J. E. Goodsell, "Validation of process simulation workflow for thermosetting prepreg platelet molding compounds," *Composites Part B: Engineering,* vol. 224, p. 109198, 2021.
[70] A. Keller, C. Dransfeld, and K. Masania, "Flow and heat transfer during compression resin transfer moulding of highly reactive epoxies," *Composites Part B: Engineering,* vol. 153, pp. 167-175, 2018.
[71] H. J. Lim, H. Choi, S.-J. Yoon, S. W. Lim, C.-H. Choi, and G. J. Yun, "Micro-CT image-based reconstruction algorithm for multiscale modeling of Sheet Molding Compound (SMC) composites with experimental validation," *Composite Materials and Engineering,* vol. 3, no. 3, pp. 221-239, 2021.
[72] M. Miletić *et al.*, "Gradient-based fibre detection method on 3D micro-CT tomographic image for defining fibre orientation bias in ultra-high-performance concrete," *Cement and Concrete Research,* vol. 129, p. 105962, 2020.
[73] A. D. Evans, C. C. Qian, T. A. Turner, L. T. Harper, and N. A. Warrior, "Flow characteristics of carbon fibre moulding compounds," *Composites Part A: Applied Science and Manufacturing,* vol. 90, pp. 1-12, 2016.
[74] L. M. Martulli, L. Muyshondt, M. Kerschbaum, S. Pimenta, S. V. Lomov, and Y. Swolfs, "Carbon fibre sheet moulding compounds with high in-

mould flow: Linking morphology to tensile and compressive properties," *Composites Part A: Applied Science and Manufacturing,* vol. 126, p. 105600, 2019.

[75] H. B. Motra, J. Hildebrand, and A. Dimmig-Osburg, "Assessment of strain measurement techniques to characterise mechanical properties of structural steel," *Engineering Science and Technology, an International Journal,* vol. 17, no. 4, pp. 260-269, 2014.

[76] P. Feraboli, E. Peitso, F. Deleo, T. Cleveland, and P. B. Stickler, "Characterization of Prepreg-Based Discontinuous Carbon Fiber/Epoxy Systems," *Journal of Reinforced Plastics and Composites,* vol. 28, no. 10, pp. 1191-1214, 2009.

[77] S. G. Kravchenko *et al.*, "Tensile properties of a stochastic prepreg platelet molded composite," *Composites Part A: Applied Science and Manufacturing,* vol. 124, p. 105507, 2019.

[78] P. D. Soden, A. S. Kaddour, and M. J. Hinton, "Chapter 7.1 - Recommendations for designers and researchers resulting from the world-wide failure exercise," in *Failure Criteria in Fibre-Reinforced-Polymer Composites*, M. J. Hinton, A. S. Kaddour, and P. D. Soden Eds. Oxford: Elsevier, 2004, pp. 1223-1251.

[79] W.-x. Fan, "On phenomenological anisotropic failure criteria," *Composites Science and Technology,* vol. 28, no. 4, pp. 269-278, 1987.

[80] M. Waddoups, "Advanced composite material mechanics for the design and stress analyst," *General dynamics, Fort Worth Division Report FZM-4763, Fort Worth, TX,* 1967.

[81] R. Hill and E. Orowan, "A theory of the yielding and plastic flow of anisotropic metals," *Proceedings of the Royal Society of London. Series A. Mathematical and Physical Sciences,* vol. 193, no. 1033, pp. 281-297, 1948.

[82] V. D. Azzi and S. W. Tsai, "Anisotropic strength of composites," *Experimental Mechanics,* vol. 5, no. 9, pp. 283-288, 1965.

[83] M.-H. R. Jen and C. H. Lee, "Strength and life in thermoplastic composite laminates under static and fatigue loads. Part II: Formulation," *International Journal of Fatigue,* vol. 20, no. 9, pp. 617-629, 1998.

[84] P. J. Hine, R. A. Duckett, A. S. Kaddour, M. J. Hinton, and G. M. Wells, "The effect of hydrostatic pressure on the mechanical properties of glass fibre/epoxy unidirectional composites," *Composites Part A: Applied Science and Manufacturing,* vol. 36, no. 2, pp. 279-289, 2005.

[85] S. W. Tsai and E. M. Wu, "A General Theory of Strength for Anisotropic Materials," *Journal of Composite Materials,* vol. 5, no. 1, pp. 58-80, 1971.

[86] Z. Hashin and A. Rotem, "A Fatigue Failure Criterion for Fiber Reinforced Materials," *Journal of Composite Materials,* vol. 7, no. 4, pp. 448-464, 1973.

[87] I. Lapczyk and J. A. Hurtado, "Progressive damage modeling in fiber-reinforced materials," *Composites Part A: Applied Science and Manufacturing,* vol. 38, no. 11, pp. 2333-2341, 2007.

[88] J. Lemaitre, "A Continuous Damage Mechanics Model for Ductile Fracture," *Journal of Engineering Materials and Technology,* vol. 107, no. 1, pp. 83-89, 1985.
[89] D. S. Dugdale, "Yielding of steel sheets containing slits," *Journal of the Mechanics and Physics of Solids,* vol. 8, no. 2, pp. 100-104, 1960.
[90] Z. Hashin, "Failure Criteria for Unidirectional Fiber Composites," *Journal of Applied Mechanics,* vol. 47, no. 2, pp. 329-334, 1980.
[91] J. P. Hou, N. Petrinic, C. Ruiz, and S. R. Hallett, "Prediction of impact damage in composite plates," *Composites Science and Technology,* vol. 60, no. 2, pp. 273-281, 2000.
[92] W. Guo, P. Xue, and J. Yang, "Nonlinear progressive damage model for composite laminates used for low-velocity impact," *Applied Mathematics and Mechanics,* vol. 34, no. 9, pp. 1145-1154, 2013.
[93] X. Li, W. K. Binienda, and R. K. Goldberg, "Finite-Element Model for Failure Study of Two-Dimensional Triaxially Braided Composite," *Journal of Aerospace Engineering,* vol. 24, no. 2, pp. 170-180, 2011.
[94] C. Zhang, N. Li, W. Wang, W. K. Binienda, and H. Fang, "Progressive damage simulation of triaxially braided composite using a 3D meso-scale finite element model," *Composite Structures,* vol. 125, pp. 104-116, 2015.
[95] Z. Zhao, H. Dang, C. Zhang, G. J. Yun, and Y. Li, "A multi-scale modeling framework for impact damage simulation of triaxially braided composites," *Composites Part A: Applied Science and Manufacturing,* vol. 110, pp. 113-125, 2018.
[96] L. Kachanov, *Introduction to continuum damage mechanics*. Springer Science & Business Media, 1986.
[97] A. Matzenmiller, J. Lubliner, and R. L. Taylor, "A constitutive model for anisotropic damage in fiber-composites," *Mechanics of Materials,* vol. 20, no. 2, pp. 125-152, 1995.
[98] G. J. Yun, F.-Y. Zhu, H. J. Lim, and H. Choi, "A damage plasticity constitutive model for wavy CNT nanocomposites by incremental Mori-Tanaka approach," *Composite Structures,* vol. 258, p. 113178, 2021.
[99] S. G. Kravchenko, D. E. Sommer, B. R. Denos, W. B. Avery, and R. B. Pipes, "Structure-property relationship for a prepreg platelet molded composite with engineered meso-morphology," *Composite Structures,* vol. 210, pp. 430-445, 2019.
[100] S. B. Visweswaraiah, M. Selezneva, L. Lessard, and P. Hubert, "Mechanical characterisation and modelling of randomly oriented strand architecture and their hybrids – A general review," *Journal of Reinforced Plastics and Composites,* vol. 37, no. 8, pp. 548-580, 2018.
[101] F.-Y. Zhu, H. J. Lim, H. Choi, and G. J. Yun, "A hierarchical micromechanics model for nonlinear behavior with damage of SMC composites with wavy fiber," *Composite Materials and Engineering,* vol. 4, no. 1, pp. 1-21, 2022.

[102] G. M. Odegard, T. S. Gates, K. E. Wise, C. Park, and E. J. Siochi, "Constitutive modeling of nanotube–reinforced polymer composites," *Composites Science and Technology,* vol. 63, no. 11, pp. 1671-1687, 2003.
[103] L. Kehrer, D. Wicht, J. T. Wood, and T. Böhlke, "Dynamic mechanical analysis of pure and fiber-reinforced thermoset- and thermoplastic-based polymers and free volume-based viscoelastic modeling," *GAMM-Mitteilungen,* vol. 41, no. 1, p. e201800007, 2018.
[104] W. Azoti and A. Elmarakbi, "Constitutive modelling of ductile damage matrix reinforced by platelets-like particles with imperfect interfaces: Application to graphene polymer nanocomposite materials," *Composites Part B: Engineering,* vol. 113, pp. 55-64, 2017.
[105] Y. Wan and J. Takahashi, "Mechanical modeling of CF/PA6 sheet molding compounds with X-ray computed tomography-based internal geometry considerations," *Composites Science and Technology,* vol. 192, p. 108104, 2020.
[106] H. Choi, H. J. Lim, and G. J. Yun, "An integrated unified elasto-viscoplastic fatigue and creep damage model with characterization method for structural analysis of nickel-based high-temperature structure," *International Journal of Damage Mechanics,* vol. 0, no. 0, p. 10567895221124324,
[107] I. Doghri, *Mechanics of deformable solids: linear, nonlinear, analytical and computational aspects*. Springer Science & Business Media, 2013.
[108] M. Springmann and M. Kuna, "Identification of material parameters of the Gurson–Tvergaard–Needleman model by combined experimental and numerical techniques," *Computational Materials Science,* vol. 33, no. 4, pp. 501-509, 2005.
[109] A. H. Gandomi, X. S. Yang, S. Talatahari, and A. H. Alavi, "Firefly algorithm with chaos," *Communications in Nonlinear Science and Numerical Simulation,* vol. 18, no. 1, pp. 89-98, 2013.

Abstract in Korean

Micro-CT Characterization and Reconstruction Modeling for Multiscale Analysis of Sheet Molding Compound (SMC) Composites

임형준(Hyoung Jun Lim)
기계항공공학부(Department of Aerospace & Engineering)
The Graduate School
Seoul National University

항공우주 및 자동차 분야 등에서 진보된 기술을 바탕으로 고성능 재료의 필요 및 적용사례가 많아지고 있다. 따라서, 기존 단일재료 본연이 가지고 있는 성능을 넘어, 두개 이상의 재료를 혼합하여 만든 복합재료의 사용이 증가하고 있다. 특히, 압축제조공정으로 생산되는 SMC 복합재료는 대량생산의 장점으로 자동차산업 분야에서 적극적으로 활용되고 있다. SMC 복합재료는 미소구조단계에서 높은 공간적 불균질성으로 SMC 판내 국부적 물성이 서로다른 문제를 가지고 있다. 이는 SMC 복합재료 성능 예측을 어렵게 만든다. 이를 해결하기 위해, 본 학위논문에서는 Micro-CT 이미지 특성화 및 확률적 재구성 알고리즘을 이용해 멀티스케일 해석을 수행하여 SMC 복합재료의 거동을 파악한다.

SMC 복합재료 연구를 시작하기 앞서, 복합재료 멀티스케일 해석을 위한 균질화기법에 대해 소개한다. 균질화는 두개 이상의 재료로 구성된 미소구조의 등가물성을 도출하여 단일재료의 거동처럼 평가하는 방법이다. 이 방법을 통해 계산된 등가물성은 일반적으로 상위 스케일 구조물에 적용되어 재료 및 구조해석을 수행하게 된다. 대표적으로 유한요소법을 사용하는 직접수치균질화법(DNS: Direct Numerical Simulation)과 복합재료의 강화재의 형태를 Eshelby 텐서로 표현하여 사용하는 평균장균질화 기법(MFH: Mean-field homogenization)이 있다. 복합재료 멀티스케일 해석을 위해 두 종류의 균질화 기법에 대해 소개하고 각각의 특징에 대해 토의해 본다.

다음으로, SMC 복합재료의 미소구조를 구성하기 위해 확률분포를 이용한 재구성 알고리즘을 소개한다. SMC 복합재료를 제작하는 공정으로부터 고유의 특징을 설계변수로 사용한다. SMC 판을 구성하고 있는 섬유 번들의 형태뿐만 아니라 방향 및 분산정도를 반영하여 미소구조 재구성 모델을 생성한다. 유한요소 정적선형해석을 수행하여 실험과의 검증을 수행하며, 변형량 측정방법에 따른 SMC 복합재료의 거동 변화에 대해 토의하고자 한다. 마지막으로 단순한 선형해석을 바탕으로 파손시점을 예측할 수 있는 방법을 이용하여 계산 비용의 절감을 제시한다. 더 나아가, SMC 복합재료의 파손기작을 분석하여 재료모델을 수행한다. 점전적 손상해석을 통해 기존 선형해석에서 관찰할 수 없는 파손기작을 시뮬레이션으로 관찰할 수 있다. 복합재료가 가지는 복잡한 파손형태 때문에 이를 해석을 통해 모사하기 위한 다양한 시도를 수행해 왔다. 본 연구에서 복합재료의 파손기준을 결정하는 다양한 기법에 대해 소개한다. 재료모델을 바탕으로 섬유의 방향 및 분산정도에 따라 변하는 인장계수 및 인장강도 계산할 뿐만 아니라 파손 패턴을 분석한다. 본 시뮬레이션 모델은 국부적으로 관찰되는 SMC

복합재료의 특성을 명시적으로 관찰하며 실험결과의 비교를 통해 제안된 방법의 검증을 수행한다.

마지막으로, 보다 효율적인 접근을 위해 해석적 균질화 기법을 이용한 SMC 복합재료 해석을 수행한다. Miro-Meso-Macroscale 의 구조를 반영하여 단계적 균질화를 수행한다. 특히 Mesostructure 에서 높은 섬유의 부피분율에 의해 발생하는 섬유 번들의 겹침을 고려하며, 제조 공정에서 발생하는 섬유의 굴곡을 모사할 수 있는 방법을 제시한다. 다양한 문헌을 통한 결과 값을 바탕으로 검증을 수행하며, 간단한 계산으로 비선형해석에 필요한 전산적 비용의 절감을 기대할 수 있다.

주요어 : 멀티스케일 해석, 복합재료, 시트몰딩컴파운드, 균질화, 미세구조, 특성화, 마이크로 컴퓨터단층촬영
학번: 2017-29220